

University of Denver

Digital Commons @ DU

Electronic Theses and Dissertations

Graduate Studies

1-1-2019

Radar Detection, Tracking and Identification for UAV Sense and Avoid Applications

Erik George Moore
University of Denver

Follow this and additional works at: <https://digitalcommons.du.edu/etd>



Part of the [Controls and Control Theory Commons](#), and the [Systems and Communications Commons](#)

Recommended Citation

Moore, Erik George, "Radar Detection, Tracking and Identification for UAV Sense and Avoid Applications" (2019). *Electronic Theses and Dissertations*. 1544.
<https://digitalcommons.du.edu/etd/1544>

This Thesis is brought to you for free and open access by the Graduate Studies at Digital Commons @ DU. It has been accepted for inclusion in Electronic Theses and Dissertations by an authorized administrator of Digital Commons @ DU. For more information, please contact jennifer.cox@du.edu, dig-commons@du.edu.

Radar Detection, Tracking and Identification for UAV Sense and Avoid Applications

Abstract

Advances in Unmanned Aerial Vehicle (UAV) technology have enabled wider access for the general public leading to more stringent flight regulations, such as the "line of sight" restriction, for hobbyists and commercial applications. Improving sensor technology for Sense And Avoid (SAA) systems is currently a major research area in the unmanned vehicle community. This thesis overviews efforts made to advance intelligent algorithms used to detect, track, and identify commercial UAV targets by enabling rapid prototyping of novel radar techniques such as micro-Doppler radar target identification or cognitive radar. To enable empirical radar signal processing evaluations, an S-Band and X-Band frequency modulated, software-defined radar testbed is designed, implemented, and evaluated with field measurements. The final evaluations provide proof of functionality, performance measurements, and limitations of this testbed and future software-defined radars. The testbed is comprised of open-source software and hardware meant to accelerate the development of a reliable, repeatable, and scalable SAA system for the wide range of new and existing UAVs.

Document Type

Thesis

Degree Name

M.S.

Department

Electrical Engineering

First Advisor

Matthew J. Rutherford, Ph.D.

Second Advisor

Kimon P. Valavanis, Ph.D.

Keywords

Micro doppler, Radar, Sense and avoid, Software defined radar, Software defined radio, Unmanned aerial systems, UAS

Subject Categories

Controls and Control Theory | Electrical and Computer Engineering | Engineering | Systems and Communications

Publication Statement

Copyright is held by the author. User is responsible for all copyright compliance.

Radar Detection, Tracking and Identification for UAV Sense and Avoid
Applications

A Thesis
Presented to
the Faculty of the Daniel Felix Ritchie School of Engineering and Computer Science
University of Denver

In Partial Fulfillment
of the Requirements for the Degree
Master of Science

by
Erik G. Moore
March 2019

Advisors: Matthew J. Rutherford Ph.D. and Kimon P. Valavanis Ph.D.

Author: Erik G. Moore

Radar Detection, Tracking and Identification for UAV Sense and Avoid Applications

Advisors: Matthew J. Rutherford, Kimon P. Valavanis

Degree Date: March 2019

Abstract

Advances in Unmanned Aerial Vehicle (UAV) technology have enabled wider access for the general public leading to more stringent flight regulations, such as the “line of sight” restriction, for hobbyists and commercial applications. Improving sensor technology for Sense And Avoid (SAA) systems is currently a major research area in the unmanned vehicle community. This thesis overviews efforts made to advance intelligent algorithms used to detect, track, and identify commercial UAV targets by enabling rapid prototyping of novel radar techniques such as micro-Doppler radar target identification or cognitive radar. To enable empirical radar signal processing evaluations, an S-Band and X-Band frequency modulated, software-defined radar testbed is designed, implemented, and evaluated with field measurements. The final evaluations provide proof of functionality, performance measurements, and limitations of this testbed and future software-defined radars. The testbed is comprised of open-source software and hardware meant to accelerate the development of a reliable, repeatable, and scalable SAA system for the wide range of new and existing UAVs.

Acknowledgments

To my family, friends, advisors, and colleagues, any and all work I have accomplished is only made possible through the continued support and encouragement of those willing to give it.

First, I'd like to thank my parents for their limitless sacrifices and commitment to my well-being and pursuit of my passions. I would not be the man I am today without your wisdom and guidance. Second, to my better half, Karen, my appreciation for your patience and support cannot be put into words. I'd like to extend my appreciation towards all my family and friends whose encouragement kept my vector pointed in the right direction.

To my advisors, Dr. Matt Rutherford and Dr. Kimon Valavanis, for providing the opportunity and guidance to accomplish this work. I am forever indebted for this invaluable experience. Finally, to all the faculty and colleagues who helped or accompanied me through endless laboratory hours, Thanks for making the time more enjoyable and the countless coffee breaks.

This work was supported by a 2018 PROF Award for a project entitled “RADAR BASED SENSE and A VOID (SAA) SYSTEM FOR UNMANNED AERIAL VEHICLES (UAVs)”

Table of Contents

List of Figures	vii
List of Tables	x
List of Acronyms	xi
List of Symbols	xiv
1 Introduction	1
1.1 Motivation	6
1.2 Problem Statement	6
1.3 Methodology	7
1.4 Contributions	8
1.5 Organization of Thesis	9
2 Background and Related Work	11
2.1 Background	11
2.1.1 Collision Avoidance	12
2.1.2 Radar	23
2.1.3 The Micro-Doppler Effect	31
2.2 Radar SAA	37
2.2.1 Performance Evaluation	38
2.2.2 Simulations	39
2.2.3 Research Systems	40
2.2.4 Commercial Systems	44
2.3 Software Defined Radar	44
2.3.1 Software Defined Radios	45
2.3.2 Software Defined Radars	46
2.4 Radar Target Identification	49
2.4.1 UAV Micro-Doppler Phenomenology	51
2.4.2 Micro-Doppler Identification Challenge	62

2.4.3	Time-Frequency Micro-Doppler Representation	63
2.4.4	Feature Extraction	64
2.4.5	Neural Networks	73
2.5	Adaptive Radar	74
2.5.1	Cognitive Radar	74
2.5.2	Fully Adaptive Radar Framework	75
3	Radar Testbed	78
3.1	Design Considerations	78
3.1.1	Problem Space	79
3.1.2	Transmit Frequency	81
3.1.3	System Architecture	91
3.1.4	Radar Type	92
3.1.5	Radar Performance	94
3.2	Testbed Design	101
3.2.1	Systems Overview	103
3.2.2	Software Defined Radio	104
3.2.3	S-Band	110
3.2.4	X-Band	114
3.2.5	RF Link Budgets	120
3.3	Prototypes	121
3.3.1	S-Band	122
3.3.2	X-Band	125
4	Experiments and Results	129
4.1	Range	129
4.1.1	S-Band	130
4.1.2	X-Band	131
4.2	Doppler	135
4.2.1	X-Band	135
4.3	Testbed Results	140
4.3.1	S-Band	141
4.3.2	X-Band	143
5	Results and Discussion	145
5.1	Conclusion	145
5.2	Future Work	147

A Radar Basics	168
A.1 Radar Types	168
A.1.1 Pulsed	168
A.1.2 Doppler	171
A.1.3 Pulse-Doppler	175
A.2 Radar Signal Processing	178
A.2.1 Matched Filter	178
A.2.2 Ambiguity Function	180
A.2.3 Pulse Compression	183
A.2.4 Frequency Modulated Continuous Wave	187
B Software Defined Radios	188
B.1 Mixed Signal Limitations	188
B.2 Frequency Conversion	188
B.3 Frontend Architecture	189
C Electromagnetic Theory	191
C.1 Electromagnetic Material Properties	191
D Bill of Materials	196

List of Figures

1.1	ICAO Airspace Classification [1]	2
1.2	Sense and Avoid Taxonomy [9]	5
2.1	Collision Avoidance Cylindrical Volumes [9]	13
2.2	Collision Avoidance Horizontal Only Geometry [9]	14
2.3	Collision avoidance minimum sensing range vs. approach angle [9]	15
2.4	SAA encounter timeline [9]	16
2.5	Bistatic Radar	19
2.6	Monostatic Radar	20
2.7	ADS-B: On-Board Functions [17]	21
2.8	ADS-B: Non-cooperative System [31]	22
2.9	SAA Non-Cooperative and Cooperative Sensor integration [22]	23
2.10	Spherical Coordinate Systems for Radar [30]	26
2.11	Typical Radar Block Diagram	27
2.12	Collision Avoidance Probability vs. extra way-point margin given sensor error [43]	40
2.13	Generation 2 DU^2SRI Radar Sensor [45]	41
2.14	CFAR Tracking of Corner Reflector with 24 GHz FMCW radar Sensor [46]	42
2.15	SDR Performances and Specifications Comparisons [56]	46
2.16	SDRad dual conversion Recieve Architecture	47
2.17	KAU-SDRad Functional Block Diagram [68]	49
2.18	KAU-SDRad Implementation [71]	49
2.19	Micro-Doppler Spectrum of Sikorsky S-55 helicopter at X-Band [87]	53
2.20	Micro-Doppler time response of Sikorsky S-55 helicopter at X-Band [87]	54
2.21	Time and Frequency response of two 1 <i>m</i> rotor blades at 1 <i>m/s</i>	56
2.22	Time/Frequency representation of two 1 <i>m</i> rotor blades at 1 <i>m/s</i>	56
2.23	Doppler Spectrum of DJI Phantom 2 at X-Band [90]	59
2.24	Octocopter hovering X-Band FMCW range velocity plot [92]	61
2.25	Octocopter hovering X-Band FMCW range localized TFR plot [92]	61

2.26	TFRs, Cadence and Cepstrum Features for Octo/Quad/Nano UAV [94]	69
2.27	First Eight simulated IMFs for single blade target (300 rpm / 2.5 m) [105]	71
2.28	Simon Haykins original concept of Cognitive Radar [11]	75
2.29	Fully Adaptive Radar (FAR) Framework [115]	77
3.1	SAA Radar Testbed Problem and Design Space	80
3.2	Atmosphere Absorption and Scatter Losses [123]	82
3.3	IEEE Radar Bands [124]	83
3.4	RCS of common geometric shapes [123]	85
3.5	Scattering of sphere [123]	87
3.6	Creeping Waves for Mie region scattering [123]	87
3.7	Atmospheric Absorption [123]	88
3.8	Atmospheric Attenuation [123]	89
3.9	Software Defined Radar Functional Architecture	92
3.10	Stretched Radar SNR vs. Pulse Repetition Frequency (PRF)	101
3.11	LMS7002 Functional Block Diagram [141]	106
3.12	LimeSDR Board Layout [142]	107
3.13	LimeSDR Block Diagram [142]	108
3.14	LimeSDR Housing from left to right: open, frontside, backside	109
3.15	LimeSDR Applications Ecosystem [144]	110
3.16	S-Band Radar Testbed Block Diagram	111
3.17	S-Band Power Amplifier Simulation Scatter Parameters	112
3.18	S-Band Power Amplifier Implemented	112
3.19	S-Band Micro-Strip Patch Antenna Geometry	113
3.20	S-Band Micro-Strip Patch Antenna Simulation	114
3.21	X-Band Radar Testbed Block Diagram	115
3.22	X-Band Up-converter Spurious Mixing Signals	116
3.23	X-Band Down-converter Spurious Mixing Signals	117
3.24	X-Band Radar Testbed Block Diagram	118
3.25	N9040B Measurement of Unfiltered Frequency Conversion Spectrum	118
3.26	S-Band Radar Testbed RF Link Budget	121
3.27	X-Band Radar Testbed RF Link Budget	121
3.28	S-Band Radar Testbed Prototype	122
3.29	S-Band RSP	123
3.30	S-Band Self-Interference Tune Testing	125
3.31	X-Band Radar Testbed Prototype	126
3.32	X-Band Stretch Processing Frequency Conversion	127
3.33	Chirp Sync New Data Packet Structure	128

4.1	S-Band Range Test: Dish target at 22 feet	130
4.2	X-Band Range Test: Dish target at 20 meters	132
4.3	X-Band Range Test: Radar Chirp Samples vs. time	132
4.4	X-Band Range Test: Radar Chirp Fast Fourier Transform (FFT)	133
4.5	X-Band Range Test: Range Measurements	134
4.6	X-Band - Real (blue) and Imaginary (red) Radar Echo of Person Walking	136
4.7	X-Band - Operator Walking - Fast/Slow Time Spectrograms	138
4.8	X-Band Micro-Doppler Contributions from a Metallic Fan	139
4.9	X-Band Micro-Doppler Contributions from a metallic fan - ZOOM	140
A.1	Radar pulse signal with return signal [41]	169
A.2	Radar range swath	170
A.3	Pulse radar block diagram [41]	171
A.4	Radar doppler effect: $f_{Dr} = \frac{2\Delta v}{\lambda}$	174
A.5	Doppler shift in radar	175
A.6	Doppler radar block diagram [41]	175
A.7	Fast time, slow time 2D radar processing data matrix	177
A.8	Maximum unambiguous range vs. velocity at operating frequency in GHz.	178
A.9	Matched filter signal processing chain	180
A.10	Pulse ambiguity function	181
A.11	Pulse ambiguity function delay cut	181
A.12	Pulse ambiguity function doppler cut	182
A.13	Linear Frequency Modulated Waveform of length $1\mu s$ and $TBP = 50$	185
A.14	Ambiguity Function of LFM Waveform of length $1\mu s$ and $TBP = 10$	186
A.15	Doppler cut of the Ambiguity Function of LFM Waveform of length $1\mu s$ and $TBP = 10$	186
B.1	Homodyne or Direct Down Conversion Receiver Architecture [153]	190
B.2	Heterodyne Conversion Receiver Architecture [153]	190
C.1	Dielectric permittivity and dielectric loss of water between $0^{\circ}C$ and $100^{\circ}C$ [154]	194

List of Tables

2.1	SAA Potential Sensor Technology Characteristics [25, 26, 27, 28, 29] .	18
2.2	Radar prototype comparison	41
2.3	Micro-Doppler Bandwidth in terms of velocity [m/s]	60
3.1	Survey of RCS of common commercial drones	90
3.2	Range and Velocity Ambiguity Settings	99
3.3	Range and Velocity Swath Requirements	99
3.4	Radar Detection, Tracking and Identification Performance Design Goals	102
3.5	Radar System Parameters to meet Performance Goals	103
3.6	Lime Microsystem’s LMS7002 Specifications	106
4.1	Radar Testbed Design Results	141
C.1	Electric and Magnetic Characteristics of Common Materials	195
D.1	Bill of Materials	196

List of Acronyms

ACF Auto-Correlation Function
ADC Analog-to-Digital Converter
ADS-B Automatic Dependent Surveillance and Broadcast
AF Ambiguity Function
AM Amplitude Modulation
AM-PM Amplitude Modulation and Phase Modulation
ANN Artificial Neural Network
ATC Air Traffic Control
CAF Cyclic Auto-correlation Function
CAS Collision Avoidance Systems
CAT Collision Avoidance Threshold
CFAR Constant False Alarm Rate
CM Center of the total body Mass
CPA Cyclostationary Phase Analysis
CPI Coherent Processing Integration
CR Cognitive Radar
CRLB Cramer-Rao Lower Bound
CSD Cyclic Spectrum Density
CVD Cadence vs. Velocity Diagram
CW Continuous Wave
DAC Digital-to-Analog Converter
DTI Detection, Tracking and Identification
DU²SRI Denver University Unmanned Systems Research Institute
EDA Electronic Design Automation
EM Electromagnetic
EMD Empirical Mode Decomposition
FAA Federal Aviation Administration
FAR Fully Adaptive Radar
FCC Federal Communications Commission
FFT Fast Fourier Transform

FLARM FLight AlaRM
FM Frequency Modulation
FMCW Frequency Modulation Continuous Wave
FPRF Field Programmable RF
FSK Frequency Shift Key
GNSS Global Navigation Satellite System
GPS Global Positioning Systems
ICAO International Civil Aviation Organization
IF Intermediate Frequency
IFFT Inverse Fast Fourier Transform
IMF Intrinsic Mode Function
ISM Industrial, Scientific, and Medical
LFM Linear Frequency Modulation
LiDAR Light or Laser Detection and Ranging
LNA Low Noise Amplifier
LO Local Oscillator
LOS Line of Sight
MCD Minimum Covariance Determinant
MFP Mean Frequency Profile
 μ D Micro-Doppler
MIMO Multiple In, Multiple Out
MMIC Microwave Monolithic Integrated Circuit
MTI Moving Target Indicator
NAS National Airspace System
NF Noise Figure
NMAC Near Mid-Air Collision
NRL Naval Research Laboratory
PA Power Amplifier
PBR Passive Bistatic Radar
PCA Principle Component Analysis
PCAS Portable Collision Avoidance System
PCR Pulse-Compression Ratio
PDF Probability Density Function
PM Phase Modulation
PM/FM Phase Modulation or Frequency Modulation
PRF Pulse Repetition Frequency
PRI Pulse Repetition Interval
RADAR Radio Detection and Ranging
RBF Radial Basis Function
RCS Radar Cross Section

RF Radio Frequency
RSP Radar Signal Processing
RTI Radar Target Identification
SAA Sense And Avoid
SAR Synthetic Aperture Radar
SDA Sense, Detect and Avoid
SDR Software Defined Radio
SDRad Software Defined Radar
SNR Signal-to-Noise Ratio
sonar sound navigation and ranging
SoP System on a Chip
SST Self-Separation Threshold
STFT Short Time Fourier Transform
SVD Singular Value Decomposition
SVM Support Vector Machine
SWaP Size, Weight and Power
TBP Time-Bandwidth Product
TCAS Traffic Collision Avoidance System
TFD Time-Frequency Distribution
TFR Time-Frequency Representation
TFT Time-Frequency Transform
UAS Unmanned Aerial System
UAV Unmanned Aerial Vehicle
USRP Universal Software Radio Peripheral
UWB Ultra-Wide Band
VCO Voltage Controlled Oscillator
VTOL Vertical Take Off and Landing
WVD Wigner-Ville Distribution

List of Symbols

λ	Wavelength
t_0	Time to Target
c	Speed of Light
R	Range to Radar Target Center of Mass
θ	Azimuth Angle
ϕ	Elevation Angle
f_{IF}	Intermediate Frequency
f_{LO}	Local Oscillator Frequency
f_{Dr}	Frequency shift induced by a target in a Monostatic Doppler Radar
S_t	Power Density Transmitted
P_t	Power Transmitted
G_a	Gain of Antenna
σ	Radar Cross Section
P_b	Power Backscattered
P_r	Power Received
A_e	Antenna Effective Aperture
β_n	Noise Bandwidth
G_r	Receiver Gain
P_n	Noise Power
T_e	Effective Noise Temperature
F_n	Noise Factor
T_0	Nominal Room Noise Temperature
χ	Signal-to-Noise Ratio (SNR)
G_s	System Gain
L_s	System Loss
L_a	atmospheric loss
f_d	Doppler Frequency Shift
D_v	Vibration amplitude of target
f_v	Vibration frequency of target
$I(t)$	In-Phase Signal

$Q(t)$ Quadrature, imaginary or 90 degrees out of phase Signal
 $s_r(t)$ Return Signal
 $s_t(t)$ Transmit Signal
 $s_d(t)$ Doppler Signal
 $\hat{\Theta}$ Unknown Deterministic Parameter
 \vec{R} Vector from radar phase center to target Center of the total body Mass (CM)
 \vec{r} Vector from target Center of the total body Mass (CM) to each particle on the rigid body
 \vec{v} Vector of Motion of a particle
 \vec{V} Translation Motion Vector
 $\vec{\omega}$ Rotational Motion Vector
 \vec{r}_0 Initial Micro-Motion Position
 k Wavenumber
 Ω Rotation Rate
 D_k The Dielectric Constant
 S_b Power Density Backscattered
 \vec{E}_b Backscatter Electric Wave
 \vec{E}_t Transmitted Electric Wave
 f_{tx} Transmit Frequency
 β_{rsp} RSP Bandwidth
 ΔR Range Resolution
 β_s System Bandwidth
 G_{rsp} Gain in SNR from Radar Signal Processing
 τ Pulse Width
 L_{fmcw} FMCW Loss Factor from reduced overlapping
 ΔV Velocity Resolution
 T_D Doppler Processing Window
 Δf_{Dr} Rayleigh Resolution of the Radar Doppler Shift
 R_{um} Unambiguous Range
 v_{um} Unambiguous Velocity
 β_{dig} Instantaneous or Digital Bandwidth
 β_{rf} RF or Analog Bandwidth
 G_t Transmitter Gain
 f_{RF} RF Frequency
 N_{max} Maximum Buffer Length in Samples

Chapter 1

Introduction

Research in the field of aviation and the continuous improvement of avionics systems has led to increased use of Unmanned Aerial Vehicles (UAVs) or, more generally, Unmanned Aerial Systems (UASs). UAVs integrate efficiently into the large and growing range of applications from aerial surveillance or surveying to warehouse or crop-field maintenance. Due to their ability to perform dynamic maneuvers, low manufacturing cost, and elimination of on-board pilots, many industries find benefit in integrating UAVs into their solutions. However, UAVs are typically designed for a limited mission scope which requires unique size, type, and performance to accomplish. The result is a growing market for safe and specialized UAVs to fit the wide range of needs which present the community with many unique challenges in order to maintain a safe and efficient National Airspace System (NAS).

The NAS has different classifications of airspace based on altitude and proximity to safety concerns based on the International Civil Aviation Organization (ICAO) classification system. The Federal Aviation Administration (FAA) recognizes

airspace classes A through G. The controlled airspace (A-E) provide Air Traffic Control (ATC) services. Classes A and E separate general airspace at 18,000 feet mean sea level. Classes B, C, and D define airspace classes surrounding airports. Class G airspace is uncontrolled airspace below Class E. Commercial UAV flight primarily occurs in Class G airspace however, further restricting limit unmanned flight. Figure 1.1 shows the current NAS airspace classifications [1].

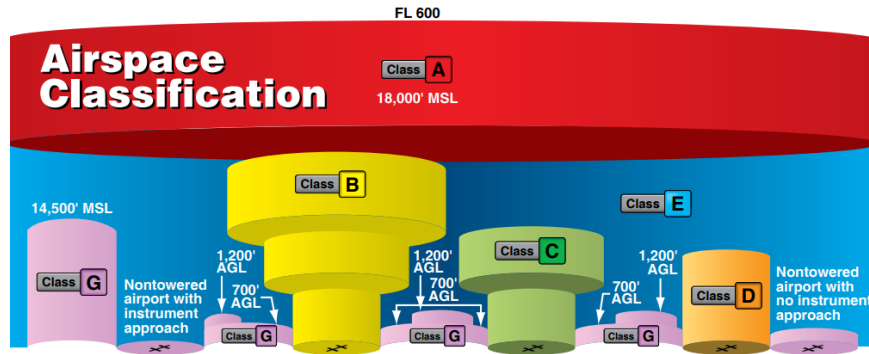


Figure 1.1: ICAO Airspace Classification [1]

Removing an on-board pilot removes a large payload component and enables missions requiring large fleets, efficiency, or long distance flight. However, unmanned flights pose a new set of problems for the aircraft systems engineers. To maintain safe and successful flights, the UAV requires more reliable communications, accurate sensors and robust control mechanisms. The FAA has recently increased restrictions on UAV flight to attempt to mitigate flight issues such as mid-air collisions [2]. Consequently, the restrictions severely limit their market potential. For example, a UAV is required to fly within the “Line-of-Sight” of the pilot and below 400 feet elevation. Some applications such as surveying or maintenance are significantly limited while others such as package delivery or large fleets are only legally allowed with special permits. To alleviate these restrictions, new technology must satisfy

the broader FAA regulation regarding “right-of-way” between aircraft [3]. This regulation requires aircraft to “see and avoid” and pass by at a “well-clear” distance from other aircraft. The definition and ability to integrate UAVs into general ATC airspace remains an ongoing problem. In fact, one of the main technology challenges as presented in the FAA’s newest civil UAS/UAV NAS integration roadmap is an airborne Sense And Avoid (SAA) system to maintain a safe distance between aircraft [4]. The main challenges for standardizing an SAA system are establishing system and performance levels, assessment of multi-sensor use, and minimum information set required for collision avoidance maneuvering.

Existing solutions to address the mid-air collision problem are already implemented in manned aircraft. The solutions contain a system or systems able to sense the navigational data of all aircraft in a given airspace, predict a potential collision, propose an avoidance maneuver and execute said maneuver. These solutions are typically divided into two categories based on their sensing techniques: cooperative and non-cooperative systems. Cooperative systems require all aircraft to proactively participate in the system and are prevalent in commercial and military aviation. They include on-board telemetry sensors, human-backed base station processors and ground based sensors cooperating through reliable communication networks. For a well-regulated, low density airspace, cooperative systems are a reliable solution and collisions are rare; however, increases in UAV flights threaten the effectiveness of cooperative-only systems.

The cooperative collision avoidance systems have a wide range of mature transponder solutions for different flight application. The transponder solutions include Traffic Collision Avoidance System (TCAS), Portable Collision Avoidance

System (PCAS), FLight AlaRM (FLARM), and Automatic Dependent Surveillance and Broadcast (ADS-B) [5, 6, 7, 8]. The different transponders solve several regimes of aircraft collision avoidance. The TCAS system is the industry standard for the collision avoidance of commercial airlines and military aircraft flying in controlled airspace. ADS-B is the communication and telemetry broadcast standard which can be incorporated into the larger TCAS system. PCAS and FLARM are low-cost, light aircraft transponder solutions for integrating into the NAS in specific short-range missions. PCAS passively listens to TCAS calls and can be used to maintain separation from larger aircraft. FLARM is a mostly European used implementation of ADS-B used for light-weight, short-range, and non-ATC missions.

Non-cooperative systems, by contrast, involve on-board sensors and processor systems to either actively or passively detect and declare a potential collision. The independent sensing of surrounding aircraft and integration of collision avoidance maneuvers into autonomous navigational systems does not require the cooperation between aircraft. They also provide one solution for a safe high-density, unmanned, uncertain integrated airspace. Due to the importance of Size, Weight and Power (SWaP) characteristics for all potential flight systems, achieving the necessary sensor performance and reliability for a non-cooperative system is still an on-going research and development problem. The research field is commonly called Sense, Detect and Avoid (SDA) or more simply, SAA, and Figure 1.2 shows the taxonomy of the problem.

There are a number of prototype systems utilizing a wide range of sensor technologies and avoidance mechanisms. This thesis will explore development of

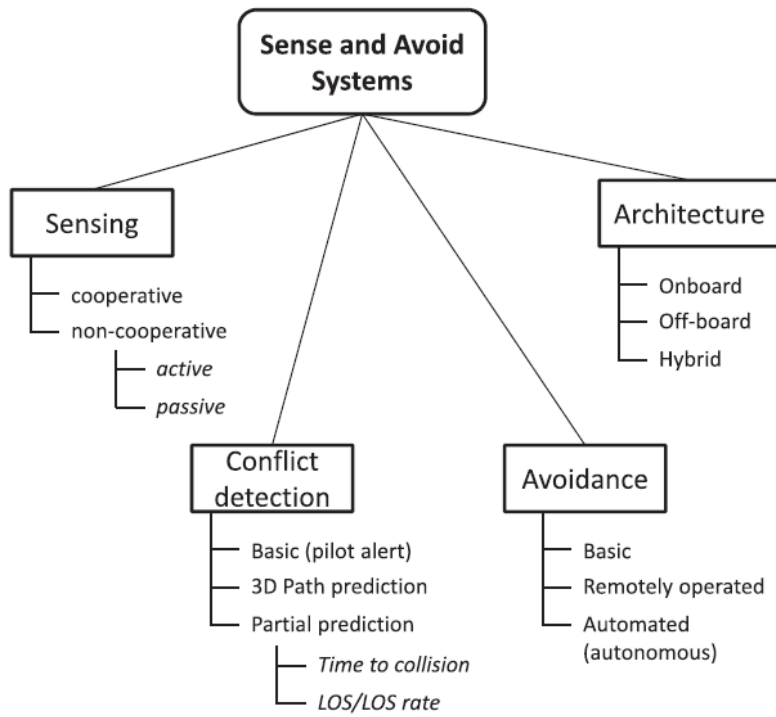


Figure 1.2: Sense and Avoid Taxonomy [9]

a prototype radar-based SAA system and fundamental research questions actively under investigation by the UAV and radar research community.

1.1 Motivation

Many sensors can be applied to SAA systems; however, radar has numerous advantages to sound, visible Light or Laser Detection and Ranging (LiDAR) alternatives due to its inherent robustness to unwanted obstruction commonly called “noise”. Unlike optical systems, radars are not largely affected by sunlight, smoke, fog, dust, or other factors that typically affect sensors utilizing optical wavelengths. Furthermore, radars typically have improved directionality and range characteristics when compared with acoustic systems. Additionally, radar systems can be used independently of aircraft with high levels of acoustic noise and can detect aircraft with little to no acoustic noise emissions (something that is increasingly important as the number of UAVs using electric propulsion increases).

Many recent attempts have been made at designing a lightweight, low power radar SAA system for collision avoidance. Each system requires accurate and robust sensors for detecting the range and velocity of a target to calculate trajectory and ultimately avoid the collision. The sensor can also provide identification of target or obstacle type. For aerial vehicles, the identifying between types of aircraft can result in better decisions made by the collision avoidance algorithm. In this thesis, the focus is on research to improve fundamental sensor performance as opposed to providing more efficient collision decisions.

1.2 Problem Statement

Radar-based SAA systems require reliable Detection, Tracking and Identification (DTI) of targets for mid-air collision avoidance. Two emerging sub-fields of radar-

based SAA systems, Micro-Doppler Identification [10] and Cognitive Radar (CR) [11], are currently active in research investigating radar systems designed for UAV-sized targets.

Micro-Doppler Identification applies machine learning techniques to extract features from unique electromagnetic echo signatures of different classes or models of UAVs and classifies them to improve avoidance decision making (i.e., knowing the flight capabilities of the opposing aircraft allows the avoidance algorithm to optimize its response). CR is a broad topic which is aimed at applying control or decision algorithms to the radar transmit signal to optimize for improved performance and/or resource management; a Software Defined Radio (SDR) enables implementation through the development of software modules rather than hardware changes.

The goal of this research is to develop a radar testbed in order to investigate fundamental research questions pertaining to Micro-Doppler radar target identification and Cognitive Radar and accelerated radar signal processing development and testing. The testbed will be capable of operating in common radar bands for UAV detection, tracking and identification and provide enough bandwidth for accurate range and velocity measurements.

1.3 Methodology

In the past, radar systems require expensive, high-performance microwave frontends and multifaceted data processing components. The recent reduction of price for flexible SDR technology has allowed for academic and industrial research laboratories to explore novel ideas and make research measurements at a reasonable

entrance expense. A radar testbed system is developed in the Denver University Unmanned Systems Research Institute (**DU²SRI**) with the aim to improve the SAA system's ability to perform all three primary radar functions specifically for UAV-sized targets. The radar testbed is designed to operate with sufficient bandwidth at common radar frequencies allocated by the Federal Communications Commission (FCC) [12]. The testbed is designed with sufficient hardware flexibility to provide software-implemented radar research algorithms pertaining to Micro-Doppler Identification and Cognitive Radar.

1.4 Contributions

A radar testbed was developed using commercially available software-defined radios, third party and in house built components, and open-source software. The radar testbed serves as a prototype for generation 3 mountable SAA radar. However, its primary use is to implement and test novel UAV SAA radar control, algorithms, and techniques.

1. S-Band and X-Band radar testbed implemented and tested with LimeSDR.
2. X-Band frequency converter design, implementation, and testing
3. SDR embedded C/C++ and HDL programming modifications for radar functionality
4. Functionality and performance testing with field measurements.
5. Analysis of Software Defined Radar (SDRad) limitations and benefits as radar testbeds.

6. Open-source software and hardware design for accelerating future SAA radar development.

1.5 Organization of Thesis

The thesis begins by providing a brief background of the required knowledge for basic understanding of UAV radar SAA. The topic requires a significant breadth of expertise including collision avoidance, radar basics, and micro-Doppler fundamentals. A motivated reader can explore a more extensive explanation in the appendices. Next, a comprehensive review of current radar SAA theory and technology is provided to justify the potential of a software-defined radar testbed to increase SAA sensor performance. Completing the background, a detailed review of current literature for two particularly popular research topics, Micro-Doppler and Cognitive Radar, is provided. These topics are particularly useful and beneficial in the push towards autonomous control. They provide examples and context for the design requirements and functionality of the radar testbed.

Chapter 3 covers the design, implementation, and evaluation of the first testbed prototypes. First, the problem space and key design decisions are discussed. A proposed solution is provided with specific parameter requirements. Section 3.2 describes the solution in great detail, covering system-level to component-level analysis of all major pieces of the testbed solution. Lastly, the prototypes and some major implementation obstacles are explored.

Chapter 4 details the field measurements made to characterize the testbed. The experiments targeted the testbed's capability of performing the three primary radar

functions: detect, track and identify. The results are analyzed and conclusions are drawn to make recommendation for future work. Future design changes are also explored based on results found throughout the design process.

Chapter 2

Background and Related Work

Substantial research and development work has been performed regarding radar SAA systems. The following background and literature review investigates the current state-of-the-art radar SAA systems technology and theory, including software-defined radar and two fundamental research areas: *Micro-Doppler Radar Target Identification* and *Cognitive Radar*.

2.1 Background

UAV radar SAA systems require a wide range of background knowledge in order to understand the fundamental principles that govern their operation. The research is based on fundamentals of collision avoidance systems, radar, Micro-Doppler (μD) effect and machine learning. The following section provides a brief introduction and current state of each.

2.1.1 Collision Avoidance

The idea of using technology for Collision Avoidance Systems (CAS) on-board aircraft has been around since the 1950s [13, 14, 15]. The early paper by Frank C. White titled *Is an Airborne System for Collision Avoidance Operationally and Technically Feasible?* urges the research community that the field is “wide open” and perhaps the “key which will unlock the door to more rapid progress either in the radar or infrared field of endeavor” [13, p. 74]. With a rise in the use of UAVs, the need for non-cooperative air-to-air SAA systems has drastically increased, and regulatory programs have created requirements and definitions for the future integration into airspace in a safe and efficient manner [4, 16, 17]. The overarching goal is to create a system that senses targets, predicts collisions and adapts flight paths with similar performance to an on-board pilot.

Integrating a unmanned CAS into NAS, the airspace surrounding an aircraft can be broken down into cylindrical volumes which serve as thresholds for the separation and collision avoidance functions. As shown in Figure 2.1, an intruding target may become a threat and eventually collide with the UAV. As the distance between the aircraft and a target increases, the uncertainty of detection, tracking and the underlining flight trajectories increases, thus the potential for collision decreases. Cooperative systems typically alert pilots of intruding targets within a large *Separation Assurance Volume*. Preliminary separation maneuvers will then prevent the intruder from crossing the Self-Separation Threshold (SST) into the *Self-Separation Volume*. The SST is typically a fixed distance determined by airspace and aircraft. More attention is needed if the intruder crosses the SST and becomes a threat. Typically, accurate and reliable systems are required to mitigate

a threat. For manned systems, the reliability and judgment of the pilot facilitates mitigation; however, UAVs require a dedicated CAS. Non-cooperative SAA systems suffer detection and tracking difficulties at long distances but become accurate and increasingly reliable at close distances, thus making them ideal for *Self-Separation Volume* use. The Near Mid-Air Collision (NMAC) volume, seen in Figure 2.1 as the *Collision Volume*, is a fixed boundary around the UAV at which safe flight can occur. The *Collision Avoidance Volume* is a volume enclosed by a variable distance called the Collision Avoidance Threshold (CAT). It is defined as the minimum distance between aircraft and threat in which the aircraft must start a successful avoidance maneuver. The CAS sensors must be able to reliably detect targets and declare potential collisions outside of the CAT.

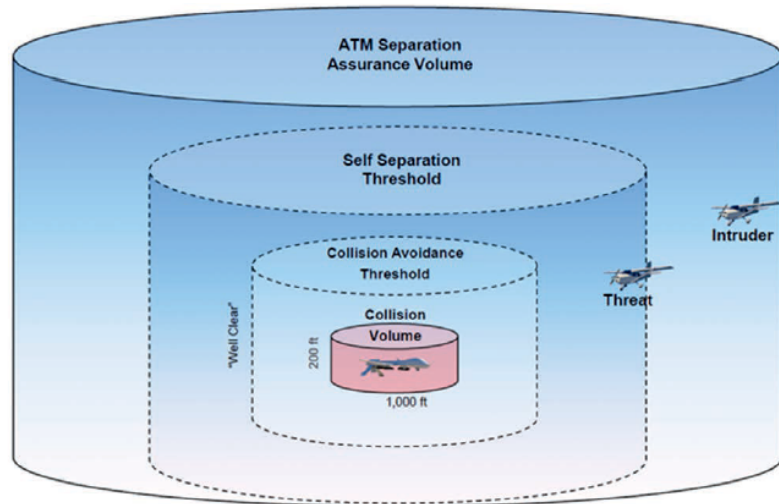


Figure 2.1: Collision Avoidance Cylindrical Volumes [9]

The CAT is a function of aircraft trajectories, avoidance maneuver and CAS performance. The threshold can be thought of as the range required for collision detection and avoidance. It is largely dependent on the flight trajectories, chosen

collision maneuver, SAA detection/tracking time, and processing time of the CAS. Typically, the CAT can be stated as the time-to-collision plus CAS time. A horizontal-only maneuver is explored in [9]. Figure 2.2 is the geometry of a target on a collision course from non-frontal angle.

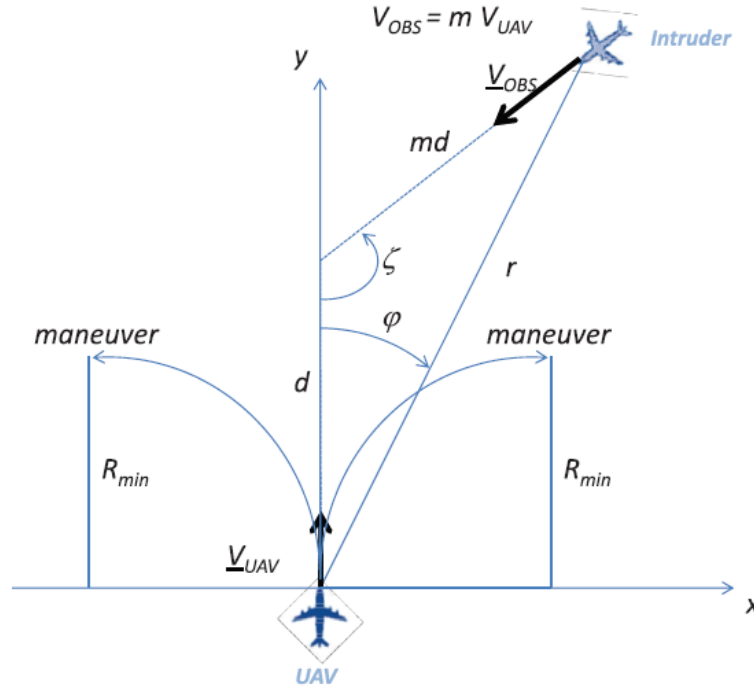


Figure 2.2: Collision Avoidance Horizontal Only Geometry [9]

Fasano solves the geometry in [9] given a UAV traveling 50 m/s , 5 second processing time, minimum distance of 500 ft, and a bank angle of 40 deg. Figure 2.3 shows the minimum sensing distance vs. approach angle for three target velocities. The plots show a minimum frontal sensing range of about 600 m for simple avoidance and conservative processing time to maintain 500 ft of separation. However, for a Part 107 UAVs, the maximum velocity is 100 mph or 45 m/s . Thus the graph can

be used as an upper bound for minimum range of detection and to gain insight into the *Collision Avoidance Volume* shape. Improving collision avoidance control theory remains a popular research field [18, 19]. However, this research will work to improve sensor performance in order to meet CAS needs.

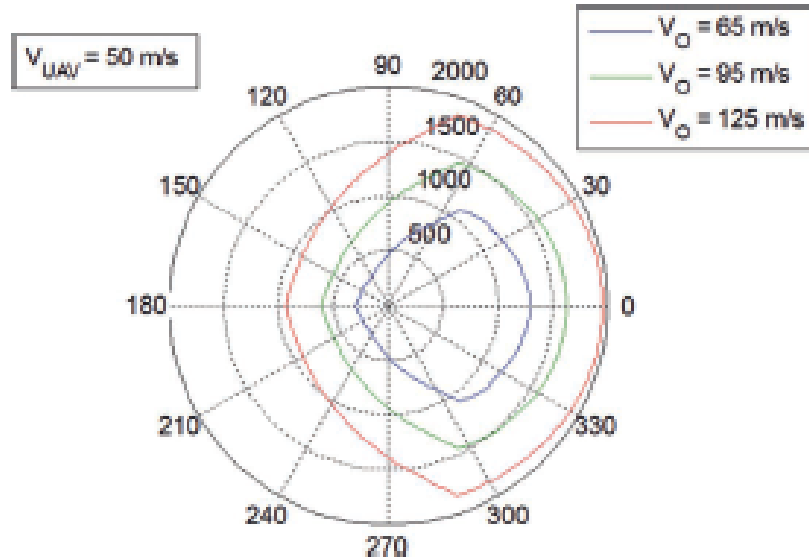


Figure 2.3: Collision avoidance minimum sensing range vs. approach angle [9]

Sense and Avoid Systems

For a SAA to be effective for UAV use, the system must satisfy the needs of the CAS within its respective airspace. Non-cooperative systems are recommended for emergency or primary use due to the potential density of future airspace, autonomous fleets, mass development of new and custom UAVs, and potential precision benefits over cooperative systems such as Global Positioning Systems (GPS). This necessitates relative location estimation via on-board sensors which

is the motivation behind “Sense and Avoid” nomenclature. Several types of sensors, architectures and levels of cooperativeness have already been theorized, implemented and evaluated for UAVs use [20, 21].



Figure 2.4: SAA encounter timeline [9]

Figure 2.4 shows a typical functional timeline and provides a format for time requirements in an SAA system. The timeline includes low-level functions such as detection, tracking and evaluation of potential collision followed by high-level functions such as declaring a required action, determining the avoidance maneuver and executing it. The low-level functions are highly dependent on the sensor type and performance of each SAA system on each UAV. The high-level functions involve complex decisions made by machine learning techniques or can often involve a

pilot or controller “in-the-loop”. The decisions can use sensor data from multiple sensors within one UAV, communicated between multiple UAVs within a UAS, or standardized across many UASs. For an SAA system to be considered completely non-cooperative, the decisions are made solely on the sensors on-board which, if properly implemented, leads to the most independent and simplified airspace integration. Currently, many proposed systems involve some level of sensor and UAS integration due to current sensor limitations [22, 23, 24].

SAA Sensors

The type and performance of SAA sensors is an important decision for systems engineers. Sensors can be thought of as a transducer that converts real physical quantities into electrical signals to be interpreted as some telemetric data. For SAA systems, the sensor is required to capture data needed for DTI of a given target. Typically, SAA sensor data includes the bearing angle (azimuth and elevation), range and relative velocity. A single sensor type commonly performs well at measuring one data type. The full relative trajectory is then calculated based on multiple or other sensor or data measurements. Popular SAA technology used for sensing is visual, thermal, LiDAR, radar and acoustic sensors. Sensor technology can be categorized as cooperative (C) or non-cooperative (NC) as well as active or passive. Active (A) means the sensor generates or transmits its own energy into the scene. Passive (P) sensors use signals already generated by the target, other systems or the environment in order to determine telemetry. Table 2.1 shows the sensor type and which telemetry it directly measures (M), calculates (C) from measurements or extracts (E) from multiple measurements.

Sensor	Type	Range	Bearing	Velocity	Trajectory
Visual Camera	NC, P	-	M	C	E
Thermal Camera	NC, P	-	M	C	E
Acoustic	NC, P	-	M	C	E
Passive Bistatic Radar	NC, P	C	M	M	E
Lidar	NC, A	M	C	M	E
Radar	NC, A	M	C	M	E
Sonar	NC, A	M	C	M	E
Transponder (mode C)	C	-	-	-	M: Altitude only
ADS-B	C	E	E	E	M: GNSS
TCAS/ACAS	C	E	E	E	M

Table 2.1: SAA Potential Sensor Technology Characteristics [25, 26, 27, 28, 29]

Non-cooperative Sensors

Non-cooperative sensors use imaging, reflectometry or a combination of both. The sensors fundamentally rely on the propagation of physical signals determined by real interactions governed by the laws of physics that carry direct information about the target’s trajectory. Most often and most used are Electromagnetic (EM) waves propagating via laws governed by Maxwell’s equations. Passive sensors generally use imaging techniques and *a priori* knowledge of the scene in order to measure bearing of the target. Active sensors generally use echolocation or reflectometry principles to measure range of the target. Velocity can be measured via a Doppler effect.

Imaging relies on scattering environmental pressure or EM waves with known or assumed sources. For passive acoustic sensing, the pressure wave or sound source is assumed or pre-processed to isolate the target itself. Multiple acoustic sensors are used to measure direction of arrival via time delays. For high frequency EM waves in the infrared or visual range, the source is assumed to be the sun or another large natural heat or light source. The main source floods the total area and the target

is assumed to scatter waves in all directions to become a secondary source. Due to the small wavelengths of visual¹ and infrared² light, the angle of arrival is easily measured with camera pixels. For the lower frequency microwaves³, passive radar relies on assumed or known man-made radio transmitters as the sources to reflect off the target. The location and frequency of the sources are known and thus, the location and velocity of a target can be triangulated or calculated via the Doppler effect. This type of radar is known as a bistatic radar where the source and receiver are not located at the same location. Figure 2.5 shows the geometry of a bistatic radar system. If the transmitter on the left is known to be part of a separate radio system, it is considered a Passive Bistatic Radar (PBR) system.

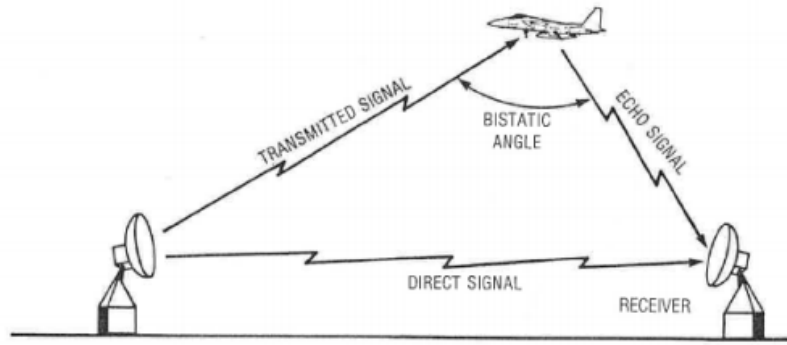


Figure 2.5: Bistatic Radar

Reflectometry is the process by which a known transmitted wave is reflected off of a target and compared with the originally generated wave in order to determine target telemetry. Visual, infrared, microwave or acoustic waves can all be used in this manner. sound navigation and ranging (sonar) uses sound pressure waves

¹Visual: $\lambda = (400nm, 700nm)$

²Infrared: $\lambda = (700nm, 1mm)$

³Microwaves: $\lambda = (1mm, 1m)$

within Earth’s atmosphere or water similar to echolocation used by bats or dolphins. LiDAR uses ultraviolet, visual or infrared light in the form of a laser in order to direct light onto a target and measure the reflections. The small wavelengths increase the bearing precision but are less robust to obstacles or weather. RADio Detection and Ranging (RADAR) which has become the standard English noun, “radar” [30], is reflectometry at microwave frequencies. The larger wavelength allows easier propagation however, tends to limit bearing angle measurement and multiple target separation. Figure 2.6 shows an example of monostatic radar which indicates the transmitter is located at the same location as the receiver. Often, they use the same antenna.

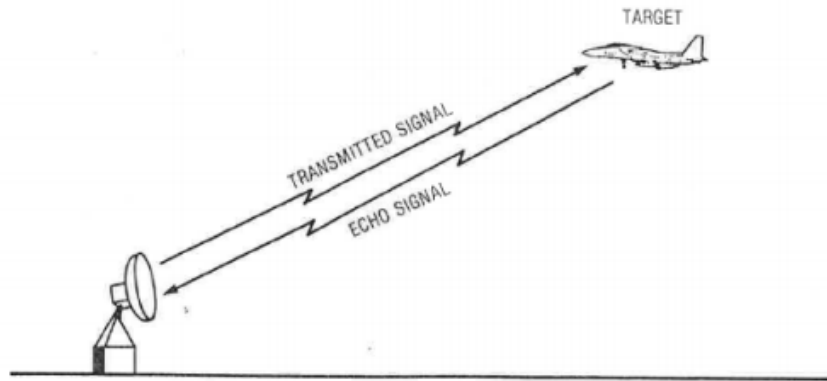


Figure 2.6: Monostatic Radar

Cooperative Sensors

Cooperative sensors such as ADS-B or TCAS use sensors such as Global Navigation Satellite System (GNSS), accelerometers, air pressure gauges or any other sensors used to determine its own location, heading and altitude [8]. Figure 2.7 shows a general functional diagram of a ADS-B system.

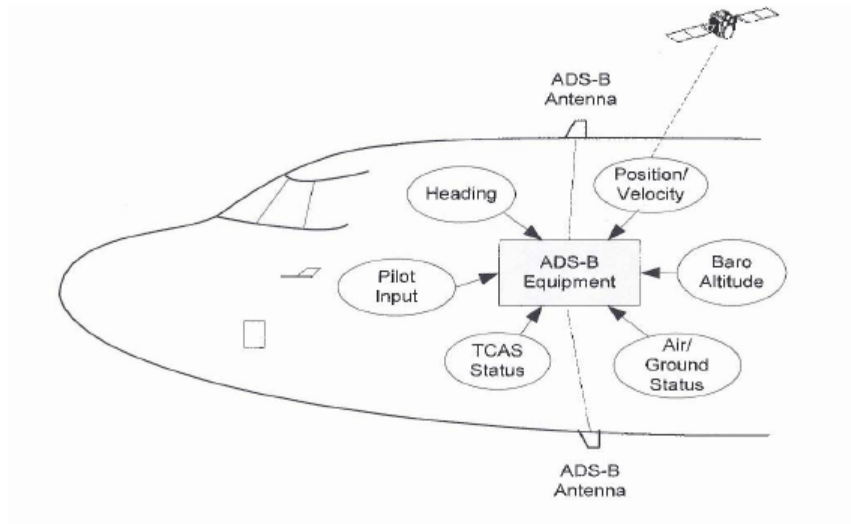


Figure 2.7: ADS-B: On-Board Functions [17]

Each aircraft sends the information on cooperative communication links between targets and base stations. Figure 2.8 shows the general ADS-B concept and one can see it requires the cooperation of aircraft, satellites, ground radar and control systems.

Sensor Uncertainty

Choosing a sensor or sensors for a particular application remains a difficult problem for system engineers. For example, an experimental study in 2016 [21] compared radar, visual and a fusion of both. It concluded that system performance is still highly dependent on sensor selection and should not be overlooked or assumed when designing a solution. The conclusion was based on their defined and measured performance error, trade-offs between target types and cost requirements. Sensor noise or error plays a fundamental role in the full SAA system performance and

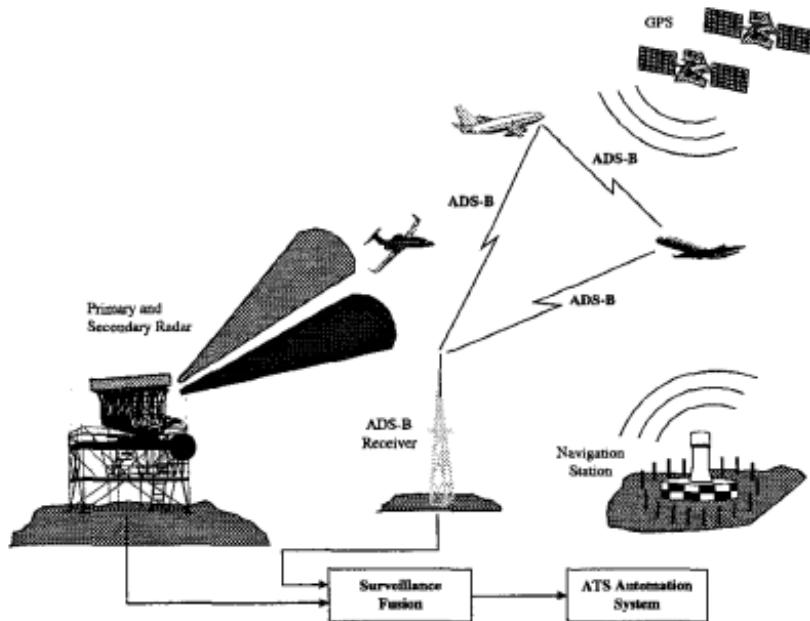


Figure 2.8: ADS-B: Non-cooperative System [31]

attempts have been made to provide frameworks in order to model and account for sensor uncertainty [32, 33, 34]. Incorporating all types of sensors, their uncertainties, sensor fusion, UAV integration, and flight dynamics into the necessary control laws or higher level UASs, traffic management frameworks continue to develop at the theoretical level [35, 36]. Figure 2.9 shows one logical structure for combining cooperative and non-cooperative collision state information. For this research, the primary goal will be to increase the performance of radar based SAA systems to fit within the non-cooperative SAA systems or larger UAS traffic management frameworks currently being implemented.

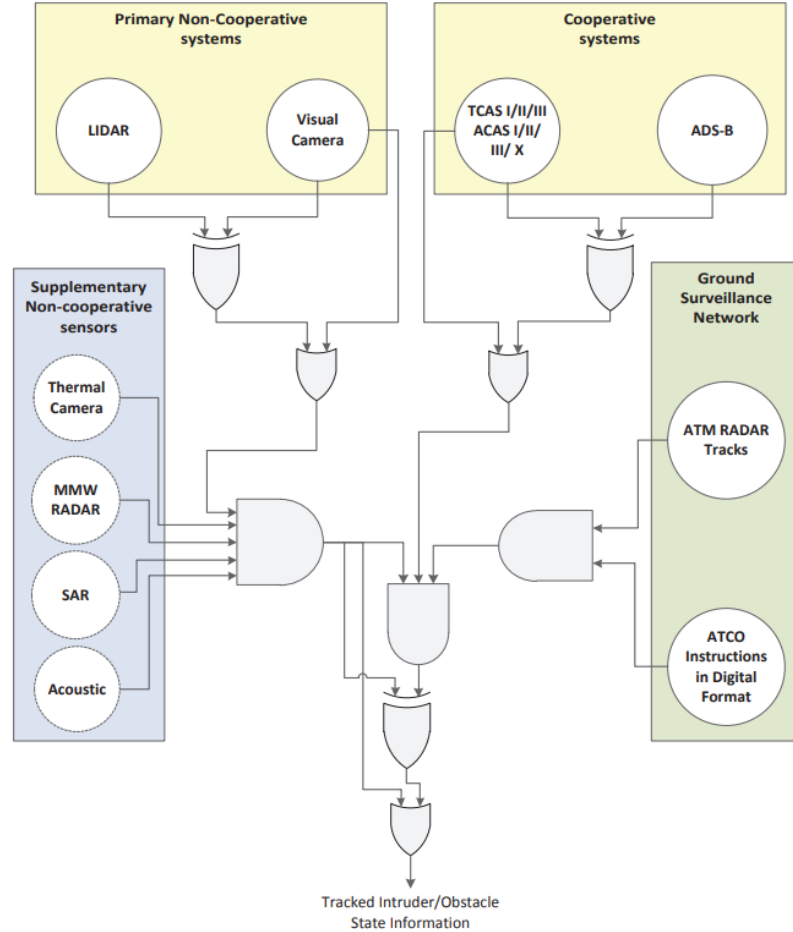


Figure 2.9: SAA Non-Cooperative and Cooperative Sensor integration [22]

2.1.2 Radar

Radar has a well-established history dating back to Heinrich Hertz's initial experiments in 1886 exploring reflection of EM waves. The publication of Hertz's book documenting his experiments forms the foundation of modern radio concepts [37]. In 1900, Tesla suggested in an interview that waves could be used for detection of moving objects. The use of radar for active detection of objects was first demonstrated by Christian Hülsmeyer who created a device he called the *Telemobiloscope*. This device,

patented in 1904, transmitted broadband Radio Frequency (RF) energy in a wide pattern while observing reflections with a narrow beam antenna which could be directed in order to make observations of a specific area. Originally intended for use in an anti-collision role in a maritime environment, the device never saw widespread acceptance [38]. In 1922, Guglielmo Marconi presented his experimental results using short wave radio to notice the effects of reflections of metallic objects miles away. Also in 1922, U.S. Naval Research Laboratory (NRL) scientists, Albert H. Taylor and Leo C. Young, demonstrate ship detection by radar and in 1930, NRL accidentally demonstrated the first aircraft radar detection.

Radar technology saw significant advances during the 1930s and 1940s in the United Kingdom, Germany, and the United States. The demands of World War II facilitated many innovations and radar technology advanced rapidly during this period. In 1935, British scientist Sir Robert Watson-Watt, motivated by the war, first demonstrated pulsed radar to detect and track Nazi air and sea craft attempting to cross the English Channel. He was instrumental in developing the *Chain Home Surveillance Radar Network* which stayed active till the end of the war and was pivotal in the ultimate outcome. In 1940, American scientists from MIT's famous Radiation Laboratory collaborated with British radar scientists to deliver the *cavity magnetron microwave power tube* to enable radar development at previously unexplored microwave frequencies. The magnetron also enabled radar to shrink small enough to be installed in aircraft. After WWII, radar applications in the civilian domain continued to increase, particularly with regard to civilian aviation. This trend continues to this day [39].

Radar Principles

In principle, a radar functions by reflecting EM waves (with wavelengths much larger than visible light) off a target and capturing the return signal through an antenna connected to electronics specially designed to estimate the time difference between the transmitted and the reflected signal. Thus the time t_0 required for an EM wave traveling at the speed of light c to traverse a distance R twice is $\frac{2R}{c}$. Equation 2.1 provides the basic relationship used for relative range measurements.

$$R = \frac{ct_0}{2} \quad (2.1)$$

Since the measured time t_0 relates to relative range from a single phase center of a monostatic radar, spherical coordinates are commonly used. In this way, the absolute distance between the radar antenna and target is known as *Range*. The *Boresight Direction* is considered the angle pointing in the direction of maximum antenna gain. Angles θ and ϕ are known as the *Azimuth* and *Elevation* angles relative to the boresight [30]. Figure 2.10 shows the spherical coordinates used to describe a target at point $P(R, \theta, \phi)$. Monostatic radar and spherical coordinates will be used for the remainder of this thesis.

Radar Architecture

A typical radar system consists of a high power microwave transmitter, low noise receiver, directional antennas, data conversion unit and a processor as shown in Figure 2.11. A transmitter typically mixes or modulates a radar waveform signal with a frequency centered around an intermediate frequency f_{IF} and local oscillator

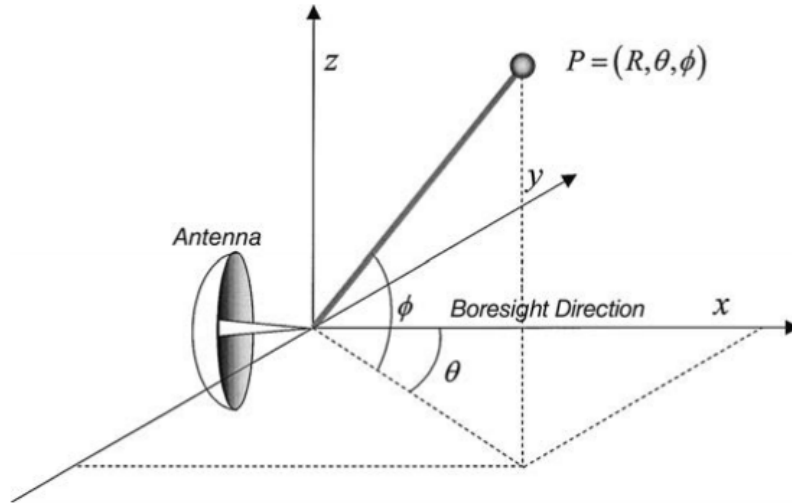


Figure 2.10: Spherical Coordinate Systems for Radar [30]

frequency f_{LO} . According to trigonometric properties, the resulting signal contains frequencies at the sum and difference frequencies. It finally passes through an amplifier able to output high powers, commonly known as a Power Amplifier (PA), and directional antennas, such as Horn antennas, radiate the signal towards a target. The target reflects a portion of the transmitted power back to the receive antenna. If the target has a relative velocity, a Doppler shift f_{Dr} is imparted on the return signal. A receiver then demodulates the transmit frequency from the received signal leaving a combination of f_{IF} and f_{Dr} . The remaining signal is then sampled and sent to a processing unit. Using radar processing techniques, the time difference between send and receive signals can be measured and used to determine the range of targets [40].

It is common to approximate the microwave power transfer through the entire radar system. Starting from the transmitter, the power density S_t radiated in all directions from the transmitting antenna is the transmit power P_t scaled by the ratio

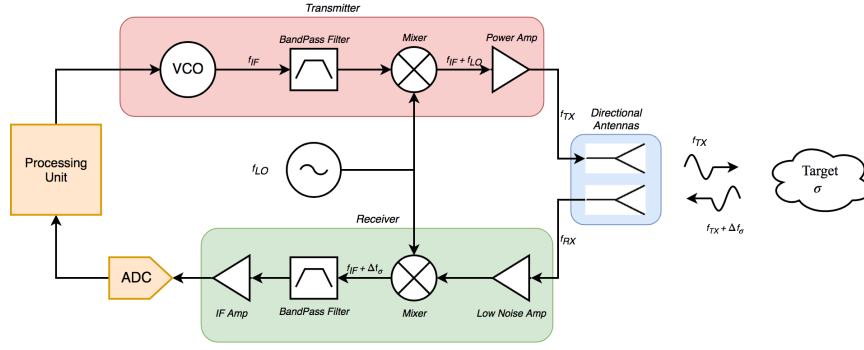


Figure 2.11: Typical Radar Block Diagram

between the antenna gain each direction $G_a(\phi, \theta)$ and the surface area of a sphere $4\pi R^2$. Taking the maximum gain or boresight leaves equation 2.2 [41].

$$S_t = P_t \frac{G_a}{4\pi R^2} \frac{W}{m^2} \quad (2.2)$$

The Radar Cross Section (RCS) σ is the power scattered off of the target in a given direction. It is defined as the ratio of backscattered power P_b to the incident power density (equation 2.3) at the particular point in the far field. Section 3.1.2 further explores the RCS.

$$\sigma(\theta, \phi) = \frac{P_b}{S_t} \text{ m}^2 \quad (2.3)$$

The re-radiated power is scattered back to the receiver and the power received P_r at the radar is again scaled by the ratio of the effective aperture of the receive antenna A_e and the spherical area.

$$P_r = \frac{P_t G_a A_e \sigma}{(4\pi R^2)^2} \text{ W} \quad (2.4)$$

Writing the effective aperture in terms of antenna gain $A_e = \frac{G_a \lambda^2}{4\pi}$ and assuming the same antenna is used for transmitting and receiving, the simple *radar range equation* is commonly written as equation 2.5. The R^4 term represents application of the inverse square law of propagation sourced from a single point and is an important relationship for calculating the maximum range. The inverse square law is applied twice, once from transmitting from the single transmit antenna and once from the target acting as a point reflector. The free space path loss $\left(\frac{4\pi R}{\lambda}\right)^2$ combines all known system parameters involved in the transmission of a signal. Equation 2.6 shows the maximum range of detection given a required minimum received power [41].

$$P_r = \frac{P_t G_a^2 \lambda^2 \sigma}{(4\pi)^3 R^4} \quad W \quad (2.5)$$

$$R_{max} = \left[\frac{P_t G_a^2 \lambda^2 \sigma}{(4\pi)^3 P_{min}} \right]^{\frac{1}{4}} \quad m \quad (2.6)$$

Receiver Noise

The minimum power received must have enough Signal-to-Noise Ratio (SNR)⁴ in order for the signal processing to detect the target. The noise power is a mix of external and internal noise. External noise is any unwanted source within the radar scene. Common sources are the sun or the *cosmic background noise* of the universe. Internal noise is usually dominated by *thermal noise* or *Johnson noise* which is a zero-mean Gaussian random process generated by temperature energy, causing electron jitter within ohmic losses of the system or heat. The power spectrum of thermal noise can be written as equation 2.7 which is constant across all frequencies.

⁴ $SNR = \frac{P_{min}}{P_{noise}}$

This type of noise is commonly called white noise. T is the temperature of the noise source in Kelvin and k_B is the Boltzmann's constant⁵ [41].

$$S_n(f) = k_B T \frac{W}{Hz} \quad (2.7)$$

Typically microwave systems have limited bandwidth β_n and thus the minimum, band-limited, thermal noise power is given by equation 2.8.

$$P_{ThermalNoise} = k_B T \beta_n \quad W \quad (2.8)$$

As the noise propagates through the receiver, it experiences a gain G_r and additional thermal noise due to losses from non-ideal sub-components. The system noise power P_n or noise at the output of the receiver can be written as the sum of thermal noise and the *effective temperature* T_e of the system. The total receiver gain G_r is assumed to be ideal linear gain and also effects the system noise.

$$P_n = k_b T \beta_n G_r + k_b T_e \beta_n G_r \quad W \quad (2.9)$$

The ratio of the total system noise output to the external thermal noise input is called the *Noise Factor* F_n (equation 2.10). To standardize this metric, T is set to $T_0 = 290 \text{ }^\circ F$ which is a nominal room temperature. Canceling like terms leaves the F_n only in terms of effective temperatures.

$$F_n = \frac{P_n}{k_b T_0 \beta_n G_r} = \frac{(T_0 + T_e) k_b \beta_n G_r}{k_b T_0 \beta_n G_r} = \frac{T_0 + T_e}{T_0} \quad (2.10)$$

⁵Boltzmann's constant: $k_b = 1.38 \times 10^{-23} \text{ Watt} \cdot \text{Second}/\text{Kevlin}$

Expressing F_n in decibels results in the Noise Figure (NF) (equation 2.11). NF can be used to simplify input/output noise characteristics of any system or components. It can be alternately defined as the ratio of input SNR to output SNR. Typically radar systems' NF span from 2dB to 3dB (170K to 2600K) [41].

$$NF = 10 \log(F_N) \quad (2.11)$$

Radar Range Equation

Equations 2.5 and 2.6 only account for ideal behavior. Most non-ideal behavior can be approximated as a linear effect on the overall SNR of the system and thus receiver noise is incorporated into the simple radar range equation. A simple multiplication factor is included within the radar range equation as required. First, the return signal power P_r of the system can be expressed as the desired SNR ($\hat{\chi}$) multiplied by the noise power as seen at the estimator $k_b T_0 \beta_n F_n$ or input noise times the noise factor F_n as seen in equation 2.12.

$$P_r = k_b T_0 \beta_n F_n \cdot \hat{\chi} \quad (2.12)$$

Applying equation 2.12 to equation 2.6 yields the radar range equation 2.13 in terms of the desired SNR needed for a given Radar Signal Processing (RSP) technique. The additional terms G_s , L_s and L_a are the system gain, system loss and atmospheric loss, respectively. System gain or losses can be from signal processing

or frontend components. Atmospheric losses are strictly more than unity and will be discussed further in section 3.1.2.

$$R = \left[\frac{P_t G^2 \lambda^2 \sigma}{k_b T_0 \beta_n F_n \hat{\chi} (4\pi)^3} \cdot \frac{G_s}{L_s L_a} \right]^{\frac{1}{4}} \quad (2.13)$$

For a more in-depth discussion of fundamental radar principles, the reader is invited to read Appendix A. The basic types, architectures, and systems are discussed in Section A.1. Some common threads of RSP are discussed in Section A.2.

2.1.3 The Micro-Doppler Effect

The Micro-Doppler (μ D) Effect was first investigated by Victor Chen in a coherent laser or light radar system or LiDAR [10]. Due to the small wavelength of a LiDAR, even small vibrations within the scale of a few μm can produce easily noticeable Doppler shifts. The vibrations of a bulk object were perceived as time-varying Doppler shifts centered around the bulk Doppler shift. Sinusoidal vibrations are seen as small oscillations in the spectrum. The maximum Doppler shift $\max \{f_d\}$ from a vibrating object is determined by the transmit wavelength λ , vibration amplitude D_v and vibration frequency f_v in equation 2.14. The concept of “micro” motions inducing “micro” Doppler shift is a broad term used for any non-bulk motion within a target such as rotating aircraft rotors or human gaits.

$$\max \{f_d\} = \frac{2}{\lambda} D_v f_v \quad (2.14)$$

For radar frequencies, the Doppler shift from vibrations becomes less detectable. For X-Band with $\lambda = 3 \text{ cm}$, a 15 Hz vibration with a displacement of 0.3 cm

produces a maximum μD shift of 18.8 Hz . At lower radar bands, the μD effects from vibrations become impractical to detect; however, larger target internal motions can be detected and used for multiple applications. The superposition of all detectable μD shifts from an entire object is often complex enough to become unique from other objects resulting in a signal commonly called *Target Signature*.

Doppler Analysis

The Doppler shifts from a single object moving in a unique direction causes a single Doppler frequency shift. Accurately measuring the instantaneous frequency of a single sinusoidal wave is a baseline for Doppler analysis. Most microwave frontends contain a coherent quadrature detector sampling both the in-phase $I(t)$ and quadrature (90 degrees out of phase) or imaginary $Q(t)$ portions of the signal. Given a return signal $s_r(t)$ (equation 2.15), the phase shift from a target's motion is $\phi(t) = 2\pi f_d t$. The transmit frequency $s_t(t) = \cos 2\pi f_0 t$ will be modulated out via hardware or software, leaving just the Doppler shift (equation 2.16) by mathematically multiplying the signals together then low-pass filtering the first term, leaving only $s_d(t)$ in equation 2.16.

$$s_r(t) = A \cos(2\pi(f_0 + f_d)t) = A \cos(2\pi f_0 t + \phi(t)) \quad (2.15)$$

$$s_d(t) = s_r(t)s_t(t) = \frac{A}{2} \cos(4\pi f_0 t + \phi(t)) + \frac{A}{2} \cos \phi(t) \quad (2.16)$$

The result will be split into I and Q parts and sampled by two Analog-to-Digital Converters (ADCs) resulting in the decomposition of $s_d(t)$ into equations 2.18 and 2.19 via Eulers Identity.

$$s_d(t) = \frac{A}{2} \cos \phi(t) = I(t) + jQ(t) = \frac{A}{2} e^{-j\phi(t)} \quad (2.17)$$

$$I(t) = \frac{A}{2} \cos \phi(t) \quad (2.18)$$

$$Q(t) = -\frac{A}{2} \sin \phi(t) \quad (2.19)$$

The goal now is to estimate f_d from $s_d(t)$ via any frequency estimation tool such as a Fast Fourier Transform (FFT) or a periodogram. For a mono-component or single tone Doppler shift, the instantaneous frequency can be calculated as the time derivative of the phase.

$$f_d(t) = \frac{1}{2\pi} \frac{d\phi(t)}{dt} \quad (2.20)$$

The velocity is then calculated by equation 2.21,

$$v(t) = \frac{\lambda}{2} f_d(t) \quad (2.21)$$

From estimation theory, the benchmark for evaluating the variance $var\{\hat{\Theta}\}$ or the performance of an unbiased estimator of some unknown deterministic parameter

$\hat{\Theta}$ is called the Cramer-Rao Lower Bound (CRLB). CRLB is defined as the inverse of the Fisher information $I(\hat{\Theta})$.

$$\text{var}\{\hat{\Theta}\} \geq \frac{1}{I(\hat{\Theta})} \quad (2.22)$$

The Fisher information is defined in equation 2.23 where $E\{\cdot\}$ is the expectation value and $p(x_k; \hat{\Theta})$ is the probability density function of ($k = 1, \dots, N$) measurements x_k of $\hat{\Theta}$.

$$I(\hat{\Theta}) = -E \left\{ \frac{\partial^2}{\partial \hat{\Theta}^2} p(x_k; \hat{\Theta}) \right\} \quad (2.23)$$

The CRLB of the Doppler frequency estimation is equation 2.24 [10].

$$\text{var}\{\hat{f}_d\} \geq \frac{6}{N(N^2 - 1) \cdot SNR} \quad (2.24)$$

Micro-Doppler Analysis

The instantaneous frequency of a real object such as an aircraft or human is often composed of a superposition of all micro motions found within. Simple time derivatives of the Doppler phase shift are no longer feasible for determining multi-component signals. Two methods have been theorized in order to analyze μ D signals with multiple deterministic frequency components. Both will be discussed in more detail in section 2.4 [10].

The first is an attempt to analytically decompose the signal into mono-component parts. The process of Empirical Mode Decomposition (EMD) is to progressively sift through the signal to find basis functions with a singular frequency component.

The basis functions are recursively subtracted from the combined signal. The basis functions are called Intrinsic Mode Functions (IMFs). EMD was eventually generalized into wavelet theory to form wavelet decomposition.

The second is an attempt to resolve the signal into a 2-dimensional joint time-frequency plane. The simplest example of a time-frequency plane is the Short Time Fourier Transform (STFT); however, limitations on time and frequency resolutions have led to advances in more rigorous definitions of what is called joint time-frequency distributions.

Micro-Doppler Effect in Radar

For a radar target, the μ D effect can be approximated as the contributions from a potentially non-rigid body broken down into rigid segments all with mass, orientation and velocity. A rigid segment is assumed to not deform with movement or pressure. The mass in a rigid body is the sum of all particle or point masses making up the total object. The orientation has six degrees of freedom around the Center of the total body Mass (CM). The CM is located at vector \vec{R} from the radar coordinate system. Each particle $P(x, y, z)$ of the rigid body is located vector \vec{r} from the CM \vec{R} . Because the body is rigid, each particle's velocity \vec{v} is defined as the time differential of its position. In equation 2.25, the velocity can be decomposed into translation \vec{V} and angular velocities $\vec{\omega}$. The latter rotational or angular velocity is called the micro motion of the object.

$$\vec{v} = \frac{d}{dt}(\vec{R} + \vec{r}) = \vec{V} + \vec{\omega} \times \vec{r} \quad (2.25)$$

The EM scattering from a complex object in motion can be predicted by making assumptions on the nature of the object or EM wave. If the rigid body segments are simple geometries, the calculated or simulated RCS of each object can be vector summed to predict total object RCS backscatter. If the body is complicated, surface geometries such as triangles can be simulated and summed. The simplifications of objects are often used to save calculation or simulation times at the expense of accuracy. The scattering process is often too complicated to be calculated analytically and largely depends on object material and electrical size. This results in many scattering behaviors such as reflection, transmission, diffraction, surface waves, ducting and interactions between them. Assumptions on the EM wave scattering type can simplify calculations to only geometric optics and ray tracing.

The EM scattering for an RCS is often simplified to a non-moving object by removing bulk translation motion \vec{V} . The internal motion of a point scatterer in the far field reflects the incident electric field $\vec{E}_i(\vec{r}_0)$ from the object at position \vec{r}_0 . The reflected field $\vec{E}_r(\vec{r})$ is the incident field modulated by some phase function shown in equation 2.26. The phase function is dependent on the wavenumber k , the motion vector \vec{r}' , and the unit vectors in the direction of the incident wave \vec{u}_k and observation \vec{u}_r .

$$\vec{E}_r(\vec{r}) = \exp \{ jkr\vec{r}'(t) \cdot (\vec{u}_k - \vec{u}_r) \} \vec{E}_i(\vec{r}_0) \quad (2.26)$$

For monostatic radar the incident and observation wave unit vectors are opposite ($\vec{u}_k = -\vec{u}_r$). The time varying motion vector is the generalized motion induced by any internal motion. For a vibrating object projected in the \vec{u}_T direction, $\vec{r}'(t) = r'(t)\vec{u}_T$. The translation motion along \vec{u}_T is the sinusoid $r'(t) = A\cos\Omega t$. The modulating

phase function is therefore defined as equation 2.27. The contribution or projection of the vibrational motion in the \vec{u}_k direction induces a sinusoidal phase modulation onto the reflected wave. When \vec{u}_T is perpendicular to \vec{u}_k , the modulating phase function has no effect on reflections, or $\exp\{j\Phi(t)\} = 1$.

$$\exp\{j\Phi(t)\} = \exp\{jkr(t)\vec{u}_T \cdot 2\vec{u}_k\} \quad (2.27)$$

For a rotating point scatter inside a rigid body, the micro-motion of each particle is limited to rotational degrees of freedom as described in $\vec{\omega}$. The motion vector becomes $\vec{r}(t) = \Delta t (\vec{\omega} \times \vec{r}_0)$, where the Δt is small enough to assume a small angle $\angle \vec{r}\vec{r}_0$. The phase function for a rotational point scatterer is shown in equation 2.28.

$$\Phi(t) = k\Delta t(\vec{\omega} \times \vec{r}_0) \cdot 2\vec{u}_k \quad (2.28)$$

2.2 Radar SAA

Using radar sensors for SAA applications of Part 107 UAV in low altitude Class G airspace has become a popular research field. Many radar techniques and transmit frequencies have been explored for potential solutions to satisfy CAS performance needs. Typical CAS performance requires a 500 *ft* (150 *m*) radius safety cylindrical area with at least 20 second warning time to perform necessary avoidance [42]. The ultimate minimum range needed for detection is determined by the UAV and intruder. A Part 107 UAV is required to fly slower than 100 *mph* or 45 *m/s*. In a frontal collision, each warning second requires a maximum of 90 *m*. If the sensor is required to cover an equivalent field of view of a pilot, the sensor must scan $\pm 110^\circ$ in

azimuth and $\pm 15^\circ$ in elevation (2 sr). To ensure adequate tracking, the scan must occur at least every 2 seconds and detect targets with 1 m^2 RCS [42]. For a survey of state-of-the-art SAA systems, a few recent performance evaluations, simulations and systems are presented.

2.2.1 Performance Evaluation

In [42], three radar bands are evaluated for SAA UAV potential. Three bands, S-Band, X-Band, and Ka-Band (3, 10, 35 GHz respectively), are investigated and compared based on CAS performance. It is pointed out that during scanning, the SNR of the receive signal must be greater than some threshold in order for detection. The SNR threshold is dependent on the overall antenna aperture, power, target RCS, radar coverage and revisit time. The antenna aperture is loosely related to the physical size of the antenna. Across operating bands and at a given antenna size, the angular accuracy increases because the main beam width decreases. For a required coverage and revisit time, the scan requires more beams with less dwell time. Therefore, with the above constants there exists a fundamental trade-off between the dwell time required for range-Doppler processing and angular accuracy controlled by operating frequency.

Stephane Kemkemian et al. further investigate this trade-off while setting the installation and performance constants to nominal values for UAVs. The authors consider multiple scanning technologies such as mechanical/electrical scanning and simultaneous digital beam forming and the cost associated with each. For S-Band, the wide beam width is cost effective for a detection function using scanning or beam forming techniques. The lack of angular accuracy hinders tracking greatly. For

Ka-Band, the higher gain antenna requires costly, high-element beam forming with complex supporting circuitry. In fact, given the necessary coverage and advanced warning, a fully sequential mechanical or electrical scan is not possible. The cost per coverage can be mitigated by separating azimuth and elevation direction to different scan techniques. The angular accuracy at Ka-Band provides an advantage for a tracking function if general location of target is already known. According to the paper and the performance metrics required by CAS function, X-band provides a sufficient balance between angular accuracy, system complexity, and scanning potential [42].

2.2.2 Simulations

In [43], Ka-Band range and velocity measurement error is simulated to predict CAS performance. The simulation uses typical high-power Ka-Band pulse radar performance characteristics. Using a simulated probability of detection with a Swerling-2 clutter model, a closing speed of 1000 *km/h* or 277 *m/s*, and 2 *m*² target RCS shows the detection range is sufficient for an 11 second collision warning time. The collision avoidance maneuver starts at 11 seconds to collision and gives a way-point outside of the safety 500 *ft* zone. Simulations show proper avoidance given for a few common collision types. More importantly, the radar trajectory estimation error is applied and probability of safety zone violations are simulated. To mitigate, an additional margin from target location is applied to the way-point.

Figure 2.12 shows the effect of azimuth and velocity safety zone violation probability versus extra margin given to way-points. Given an extra 50 *m* way-point margin the probability of collision avoidance given azimuth or velocity error increases

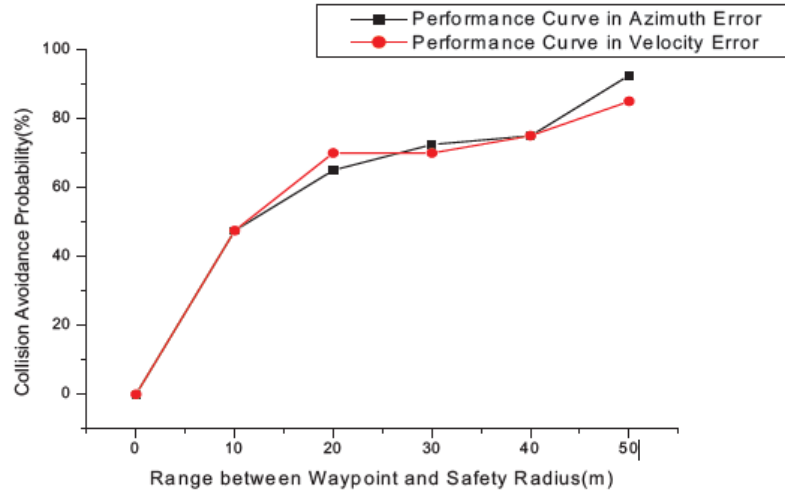


Figure 2.12: Collision Avoidance Probability vs. extra way-point margin given sensor error [43]

to 85%. This shows that significant care must be taken to compensate for sensor uncertainty and thus investigating higher performance radar sensors can yield a significant effect on preventing collisions.

2.2.3 Research Systems

The research and development performed within this thesis for **DU²SRI** is based on prior research performed resulting in publications and patents [44, 45]. Two generations of radar based SAA systems were developed. The first was a Continuous Wave (CW) gunplexer-based X-Band sensor. The second was a light-weight, low-power Frequency Shift Key (FSK) X-Band radar system using an XMOS processor. Table 2.2 shows the system characteristics of each generation.

Generation	1	2	2a
Mass (g)	250	150	360
Dimensions (cm)	15.5x10x9	10x10x10	13x10x17.5
Power Consumption (W)	4.5	4.5	5.8
Input Voltage (VDC)	10-15	5-6	5-6
Transmit Frequency (GHz)	10.5	10.5	10.5
Transmit Bandwidth (MHz)	-	5	5
Transmit Power (mW)	10	0.4	0.4
Modulation	-	FSK CW	FSK CW

Table 2.2: Radar prototype comparison

Shown in Figure 2.13 is the radar sensor mounted on a mechanical scanning platform. The X-Band frontend is a commercially available unit with a 5 MHz bandwidth. This bandwidth severely limited the range resolution and lead to tracking errors.

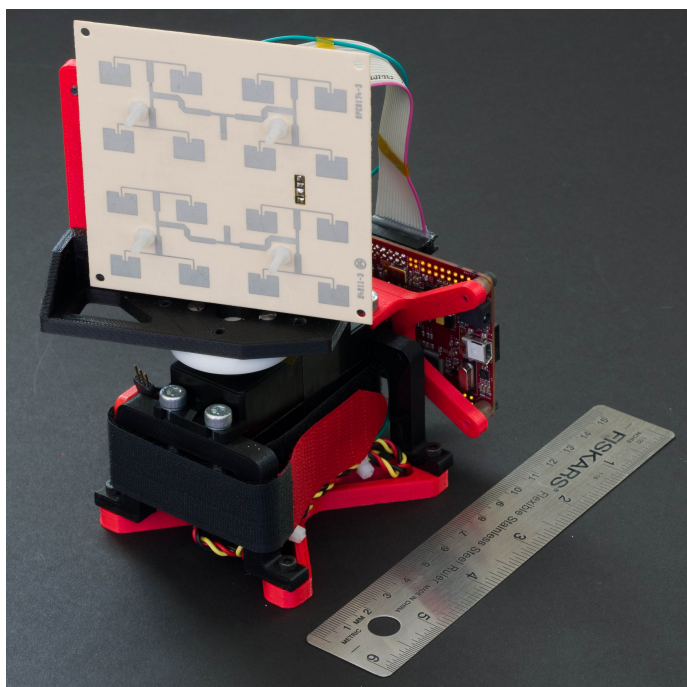


Figure 2.13: Generation 2 DU^2SRI Radar Sensor [45]

In [46], experiments using a commercial 24 GHz Frequency Modulation Continuous Wave (FMCW) SENTIRE radar by IMST investigate potential for CAS sensor [47]. The sensor uses phase interferometry between two return channels in order to measure azimuth angle. A corner reflector and a DJI F450 quadrotor are used as targets. A transmit bandwidth of 1 GHz is used to achieve a range resolution of 13.5 cm with experimental error of ± 0.3 cm. A 40 cm separation between two targets was easily detectable. The radar was mounted on a movable platform and motion tracking was evaluated. An offline Constant False Alarm Rate (CFAR)-based tracking algorithms output is shown in Figure 2.14. The tests yield strong close-range target to clutter ratio and accurate range/bearing measurements. The tests did not include Doppler processing for velocity and concluded offline processing of identification and tracking was recommended.

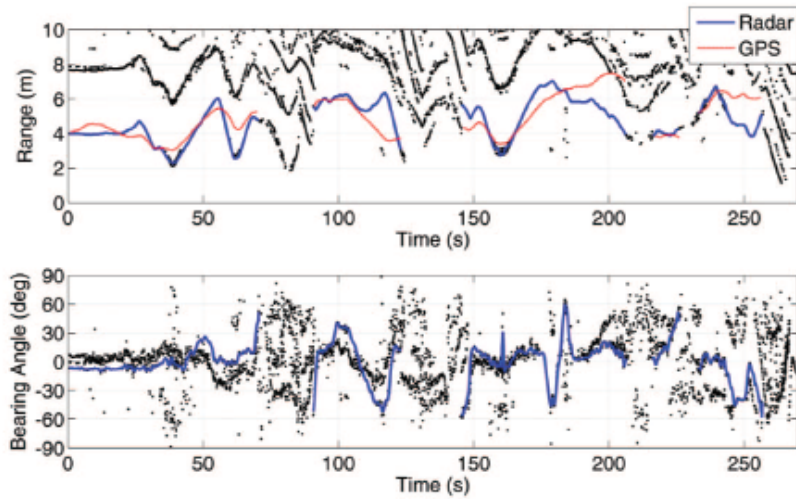


Figure 2.14: CFAR Tracking of Corner Reflector with 24 GHz FMCW radar Sensor [46]

In [48], an X-Band FMCW radar sensor using a flood transmitter and digital beam forming receivers was designed, implemented and evaluated for SAA applications. The advantage of beam forming is high (or sometimes simultaneous) scan rates and multi-beam tracking. The sensor was developed within Rockwell Collins France and tested using a Cessna 172 as a target. Detection ranges were found to be 10 *km* for head-on collisions and 5 *km* at a 45° angle.

In [49], a low SWaP, K-Band FMCW radar sensor with one transmit channel and two receive channels was designed, developed and evaluated. A 24 GHz homodyne Microwave Monolithic Integrated Circuit (MMIC) transceiver chip converts K-Band energy down to DC baseband Intermediate Frequency (IF). A baseband board conditions the IF signal, and a Texas Instruments micro-processor board captures and processes the data. The radar waveform is 140 *MHz* wide with a 730 *Hz* PRF. Experimental testing shows easily separated corner targets (with undeclared RCS) 2 *m* apart at less than 16 *m* away.

In [50], an ultra low SWaP, W-Band FMCW radar was developed and tested. W-Band radar has recently become popular due to large available bandwidth and high Doppler shifts yielding smaller range resolution and faster Doppler processing. The paper presented two versions of W-Band radar sensors. The first design transmitted at 76 GHz with 6 GHz potential bandwidth. The theoretical 2.5 *cm* range resolution was almost experimentally proven by successfully separating targets 4 and 10 *cm* apart. The second design miniaturizes the sensor to less than 1 *cm*³ and 7 *g* at the expense of a reduced bandwidth to 500 *MHz*. The power and microwave performance was verified similar to the first design, thus maintaining sensor performance only with bandwidth reduction.

2.2.4 Commercial Systems

A few commercial radar SAA systems are available for public use. Due to the push for driverless cars, prominent integrated circuits companies have begun developing automotive radar sensor solutions. Texas Instruments and NXP have developed a W-Band, 4 GHz BW, multi-channel automotive radar MMIC (AWR1642/MR3003) and evaluation boards [51, 52]. Analog Devices has a suite of K-Band automotive radar enabling MMICs and processing units [53]. Opportunities for recycling automotive sensor development for UAV applications should be monitored as significant overlap between the two applications exist.

A few companies specialize in commercial drone radar SAA for airspace mitigation. Fortem Technologies develops an electronically steerable Ku-Band drone sensor [54]. Echodyne Echoflight is a low SWaP, airborne detection and tracking radar system. It utilized a preparatory *Metamaterial Electronically Scanning Antenna* technology for fast electronic scanning. According to FCC records, the airborne SAA operates within the Ka-Band at about 24 GHz [55]. Both commercial SAA radars are in early release and have not proven market potential or functionality at the time of this thesis.

2.3 Software Defined Radar

The concept of SDRad has emerged recently in the research communities. The need for rapid RSP prototyping and development is driven by the need for high-performance sensors and saturation of microwave bands. The move to designing flexible and dynamic hardware frontends supported by programmable software

reduces development time and costs by providing a single “*one-size-fits-all*” hardware approach. However, the complexity required is not to be taken lightly. A similar move to software-defined has taken place in the radio world.

2.3.1 Software Defined Radios

Recent advances in fundamental RF and microwave integrated circuit technology have enabled the creation of an SDR. Thus, opportunities for fundamental research at a low entry cost have emerged. The primary application of flexible radio systems is to compensate for over-saturation of EM wave propagation at FCC allocated bands. The resulting wide-spread interference and management issues can be tackled by adapting the complex EM environment on a case-by-case basis. Relieving allocation pressures are currently the focus of active research inside of governmental, private and university research institutes. An SDR is essentially a transceiver with a wide range of hardware settings controlled by software applications. Some common hardware settings are tune frequency, bandwidth, sample rate, gain and filter cutoffs. Transceivers function as a signal converter from RF and microwave frequencies to digital signals for later computational processing. SDRs require a vast knowledge of mixed signal performance limitations, physical limitation, and frontend architecture solutions. For more information, see Appendix B.

There are a variety of commercially available SDRs for hobbyists, enthusiasts, and professionals. Most common communication protocols use the license-free Industrial, Scientific, and Medical (ISM) bands at 2.4 *GHz* and 5 *GHz*. Figure 2.15 is a table of common SDRs in the market and their performance. SDR development has recently accelerated due to reduced manufacturing cost of transceiver MMIC chips.

	HackRF One	Ettus B200	Ettus B210	BladeRF x40	RTL-SDR	LimeSDR
Frequency Range	1MHz-6GHz	70MHz-6GHz	70MHz-6GHz	300MHz-3.8GHz	22MHz-2.2GHz	100kHz-3.8GHz
RF Bandwidth	20MHz	61.44MHz	61.44MHz	40MHz	3.2MHz	61.44MHz
Sample Depth	8 bits	12 bits	12 bits	12 bits	8 bits	12 bits
Sample Rate	20MSPS	61.44MSPS	61.44MSPS	40MSPS	3.2MSPS	61.44MSPS (Limited by USB 3.0 data rate)
Transmitter Channels	1	1	2	1	0	2
Receivers	1	1	2	1	1	2
Duplex	Half	Full	Full	Full	N/A	Full
Interface	USB 2.0	USB 3.0	USB 3.0	USB 3.0	USB 2.0	USB 3.0
Programmable Logic Gates	64 macrocell CPLD	75k	100k	40k (115k avail)	N/A	40k
Chipset	MAX5864, MAX2837, RFFC5072	AD9364	AD9361	LMS6002M	RTL2832U	LMS7002M
Open Source	Full	Schematic, Firmware	Schematic, Firmware	Schematic, Firmware	No	Full
Oscillator Precision	+/-20ppm	+/-2ppm	+/-2ppm	+/-1ppm	?	+/-1ppm initial, +/-4ppm stable
Transmit Power	-10dBm+ (15dBm @ 2.4GHz)	10dBm+	10dBm+	6dBm	N/A	0 to 10dBm (depending on frequency)
Price	\$299	\$686	\$1,119	\$420 (\$650)	~\$10	\$299 (\$289 pre-order)

Figure 2.15: SDR Performances and Specifications Comparisons [56]

2.3.2 Software Defined Radars

For SDRad, the same basic transceiver technology is used for radar sensing applications. The main difference between radio and radar systems' performance requirements is found in the interaction between transmit and receive channels. Signal processing and higher-level network management are typically responsible for coherence between radios, and precise hardware synchronization is not required for most protocols. At the core of a radar system is an active time estimate, and therefore sufficient isolation and precise synchronicity between channels take priority. A few research labs have designed and developed SDRads. Research into the potential of SDR technology for radar use has also been investigated.

Researchers at Ohio State University have developed a few iterations of SDRads starting in 2010 [57]. A Multiple In, Multiple Out (MIMO) SDRad for testing new adaptive waveform techniques was designed, implemented and tested. The design operated from 2 – 18 GHz with 500 MHz of bandwidth transmitting and receiving across 4x4 (4 transmit and 4 receive) channels of dual polarized antennas. The design used commercially available DSPs and ADC/DAC modules. A custom RF frontend, and an antenna array driven by a switch matrix was developed for flexible radar performance. The DSP processor interacts with a CPU/GUI and can generate any arbitrary waveform. It also processes higher level RSP across 2x2 channels. The RF frontend converts the 2x2 channels to a selectable microwave frequency using double conversion architecture. A homodyne, I/Q mixer first converts signals to 2 GHz IF. It is followed by a tunable heterodyne mixer allowing for user control up to 18 GHz . The block diagram is shown in Figure 2.16. The switch matrix antenna multiplexes the 2x2 channels into vertically and horizontally polarized 4x4 channels. Evaluations were run showing successful range vs. speed plots of a truck.

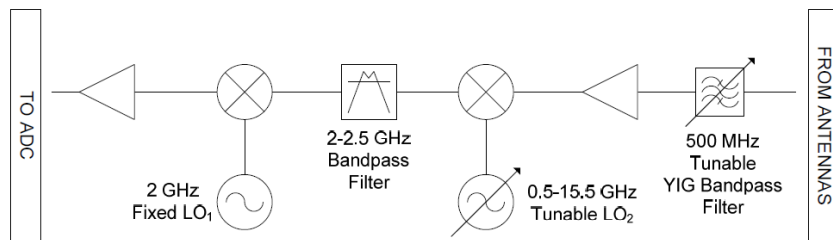


Figure 2.16: SDRad dual conversion Recieve Architecture

Another 2x1 MIMO SDRad RF frontend was developed at a fixed X-Band frequency with potential for antenna multiplexing to 4 receive channels and 250 MHz bandwidth. The frontend was implemented on a microwave capable circuit board

and tested for performance [58]. Investigations into the usefulness of pre-existing SDRs were also conducted using Texas Instruments small form factor SDRs [59] and (more recently) a Universal Software Radio Peripheral (USRP) [60, 61]. USRPs are developed by Ettus Research and are widely regarded as the leader in SDRs for research environments. Numerous USRP SDRad evaluations have been conducted with the minimum necessary antennas and amplifiers [62, 63, 64, 65, 66, 67]. The tests' transmit frequencies range from 0.9 – 6 *GHz* as provided by the USRP. Varying degrees of success are reported showing promise for SDRad research and even enabling more sophisticated radar techniques. Of note, a synthetic Ultra-Wide Band (UWB) waveform utilizes the USRPs total frequency range for higher range resolution in [65].

A multi-channel, multi-mode SDRad platform operating at S, X and K band was theorized, designed and developed within the Korea Aerospace University [68]. The system is designed to have multiple RF frontends supported by a signal processing module for data conversion, arbitrary waveform design, and RSP. The system is implemented into PCI modular slot card housing and tested for use with drone detection, μ D signatures and traffic securities [69, 70, 71]. The K-Band frontend is used for drone detection with a variety of quad drones placed 50 to 100 *m* from the SDRad. The μ D analysis is performed with a sphere and cylindrical pendulum at S-Band. The oscillations appear as 5 to 10 *Hz* within the Time-Frequency Representation (TFR). Figure 2.17 shows the functional block diagram of the KAU SDRad. The system is divided into four main sub-systems; the antenna, the RF module, the signal processor module, and the software module. Both the antenna and

RF module run multiple bands in parallel. The modules can be seen in Figure 2.18 as slots within a PCI Express chassis.

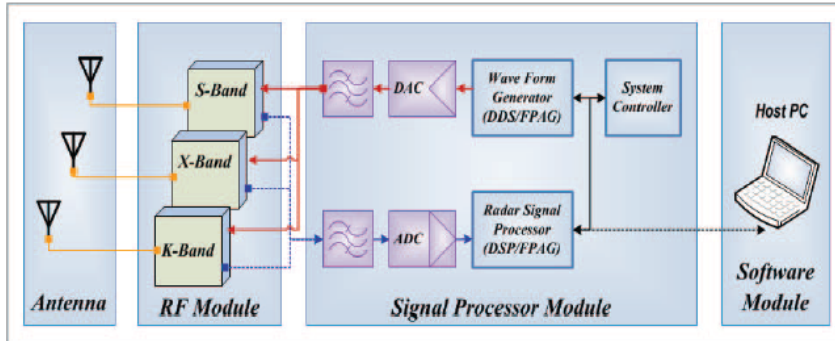


Figure 2.17: KAU-SDRad Functional Block Diagram [68]

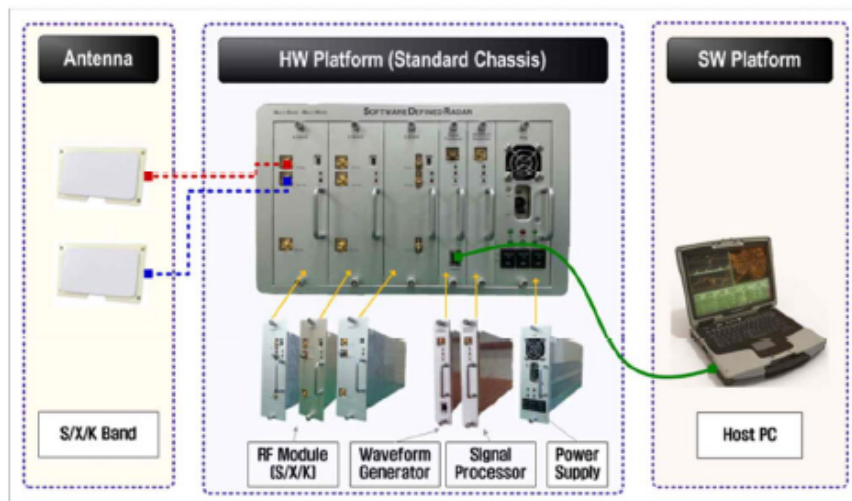


Figure 2.18: KAU-SDRad Implementation [71]

2.4 Radar Target Identification

The concept of Radar Target Identification (RTI) has been theorized as early as the 1950s when Dr. E. M. Kennaugh first theorized the “Impulse Response” a target

exhibits during the EM scattering process [72, 73]. The scattering impulse response, which utilizes Rayleigh or Mie scattering as described in Section 3.1.2, exhibits unique observable natural resonances. It was eventually theorized that the unique natural resonances of specific target geometries could be used for discriminating the targets themselves [74, 75, 76, 77]. Natural resonances occur when geometries of the target are similar to the wavelength of an incident wave and thus ring when stimulated. The concept can be easily seen with sound waves in a tuning fork and in fact are present within any higher differential order system. At the time, the targets were primarily larger military aircraft with EM resonances within HF or VHF bands, and the radars lacked the capability or bandwidth to implement a proper identification system. However, efforts to increase resonance or use synthetic aperture techniques were explored[78]. One important concept resulting from Kennaugh's investigations is the idea of a pole killing pulse or K-Pulse [79, 80]. It is defined as the pulse of minimum length whose Laplace transform cancels all poles or natural resonances of a system using singularity expansion method. The concept was an EM scattering adaptation of previously explored waveforming filters to minimize intersymbol interference in communication systems. K-Pulses were eventually generalized into an Extinction Pulse or E-Pulse which can selectively annihilate poles not just exhibited by some target [81, 82]. Both pulses were explored for target identification but were essentially the same concept [80, 81, 83]. E-Pulses are still active today within many signal processing fields, such as ground-penetrating radar, as the theoretical foundation of scattering identification [84, 85]. Recently, it's been broadly generalized into wavelet theory.

A competing RTI technique involves increasing spacial radar performance in order to capture an image of a scene and thus providing enough detail to discriminate targets. The main performance limitation is angle resolution determined by antenna main lobe width or gain. Given a certain antenna size, a maximum gain is achievable. Thus, to increase resolution a technique of capturing many samples of a scene from a linear moving radar increases effective aperture width. The process is called Synthetic Aperture Radar (SAR). SAR also requires higher bandwidth and transmit frequency for range resolution and detail.

For RTI applications, both E-Pulse and SAR suffer performance limitations. For E-Pulse, the time resolution required to implement ns pulses is limited by ADC/DAC performance and require large bandwidths at lower microwave bands. SAR is still a maturing technology and requires image machine learning techniques to overcome the fact that the image depends on the angle-of-view. Also, they do not consider target dynamics. It was not until Victor Chen in 2000 explored and formalized how micro motions effect the radar signal that researchers began exploring target μ D signatures as a discrimination tool [86].

2.4.1 UAV Micro-Doppler Phenomenology

The wavelength change observed from a target moving relative to the observer is known as the Doppler effect [10]. As described in Section 2.1.3, this phenomenon is the basis for techniques used to measure target velocity. When a target has internal components moving relative to the bulk average velocity, such as a human walking or rotor blade, the radar signal experiences μ D effects which ultimately appear as unique frequency band characteristics. In the following section, the radar phenomenology

for UAVs and their μ D signature will be explored to provide the intuitive knowledge required to understand μ D based RTI.

Rotor Micro-Doppler Effect

The phenomenon of μ D on common rotor aircraft has been theorized, simulated and experimented [10]. Prior to Chen’s formalization, a few experiments were performed taking frequency and time domain pictures of the μ D effect of a Sikorsky S-55 replica helicopter [87]. From the spectrum in Figure 2.19, the skin line is the bulk velocity of the helicopter and is negative due to separating flight velocity from radar. The rotating rotor hub is seen as the lobe around the skin line. The rotor blades are observed as flat shoulders on either side of the main hub region.

In Figure 2.20, the time response shows impulses at regular intervals. The impulses are caused when rotor blades are perpendicular to the radar and a large RCS is present, commonly called the rotor “flash”.

Rotor Micro-Doppler Theory

From [10], Chen formalized the μ D effect of rotor blades. First, given the distance $R_p(t)$ from the radar to a single blade scatter center, the phase function $\Phi_p(t)$ is shown to be equation 2.29.

$$\Phi_p(t) = \frac{4\pi}{\lambda} R_p(t) \tag{2.29}$$

After integrating over the length of rotor L and generalizing for K rotors, equation 2.30 shows the phase function $\Phi_k(t)$ for the k th rotor. The rotor rotation

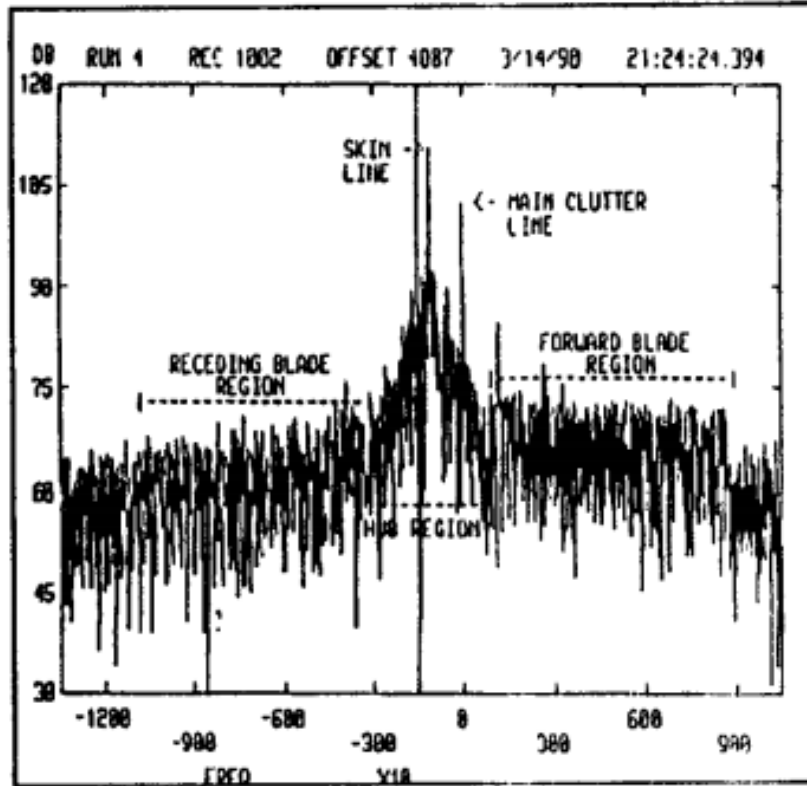


Figure 2.19: Micro-Doppler Spectrum of Sikorsky S-55 helicopter at X-Band [87]

rate Ω has a rotation angle of ϕ_0 . The center of rotation has a radar elevation angle of β .

$$\Phi_k(t) = \frac{4\pi L}{\lambda} \frac{1}{2} \cos \beta \cos (\Omega t + \phi_0 + k2\pi/N) \quad (k = 0, 1, 2, \dots, K - 1) \quad (2.30)$$

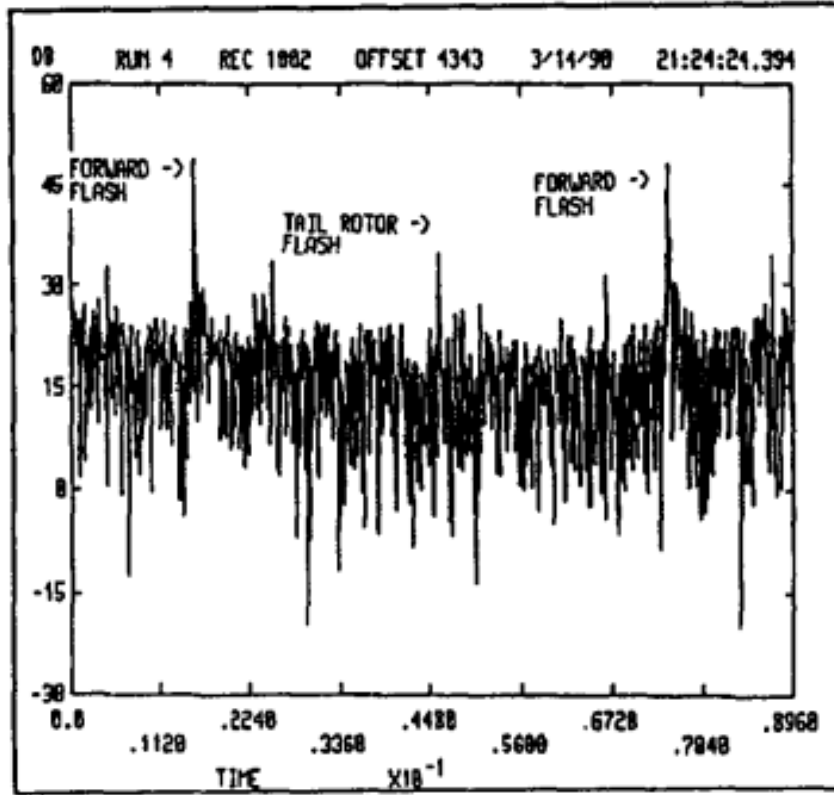


Figure 2.20: Micro-Doppler time response of Sikorsky S-55 helicopter at X-Band [87]

Finally, the returning μ D signature signal is shown in equation 2.31. The range and height to the center of rotation are R_0 and z_0 , respectively.

$$s_{\mu D}(t) = L \exp \left\{ -j \frac{4\pi}{\lambda} [R_0 + z_0 \sin \beta] \right\} \sum_{k=0}^{K-1} \text{sinc} \{ \Phi_k(t) \} \exp \{ -j \Phi_k(t) \} \quad (2.31)$$

Taking a closer look at rotor μ D signature signal, the first exponent is constant phase shift from the propagation distance between radar and rotation center. Each rotor blade contributes the phase modulation function $e^{-j\Phi_k(t)}$ modulated by the sinc function of the phase function. The phase function is a cosine whose amplitude

depends on the maximum Doppler shift generated by the rotor blade and frequency depends on blade rotation velocity. The phase modulation function is thus governed by a Bessel function of the first kind. The time-varying Doppler frequency shift is enveloped by a sinc impulse train at Ω radians per second. The maximum of the impulse train is located at the maximum Doppler shift frequency resulting in a high-energy broadband Doppler Shift. This equation represents the rotor “flash”.

Rotor Micro-Doppler Simulation

Figure 2.21 shows the simulation of two 1 *m* rotor blades rotating at 10 revolutions per second and traveling at 10 *m/s* based on equation 2.31. The radar sensor is operating in X-Band 707 *m* away at an elevation of 45°. The rotor “flash” is seen in the time response when rotors are perpendicular to the radar Line of Sight (LOS). The rectangle frequency bandwidth is caused by the maximum and minimum velocities at the tips of rotors from forward and backward drifting rotors. The near ideal rectangle envelope can be seen in equation 2.31 as the Fourier Transform of the sinc function convolved with the phase modulation function. The entire bandwidth has a shift due to bulk rotor velocity.

In Figure 2.22, a simulated time-frequency representation of the rotor is shown. Both rotors are seen as sine waves with a 180° phase shift. The “flash” is seen at peaks as a vertical line. The RCS increase is seen as an increase in magnitude in the time-frequency plot. Again, the bulk velocity is seen as a frequency offset of the μ D signature.

Comparing the simulation results with the measured spectrum from Figure 2.19, the rectangle bandwidth is seen as the shoulders of the main hub and skin line.

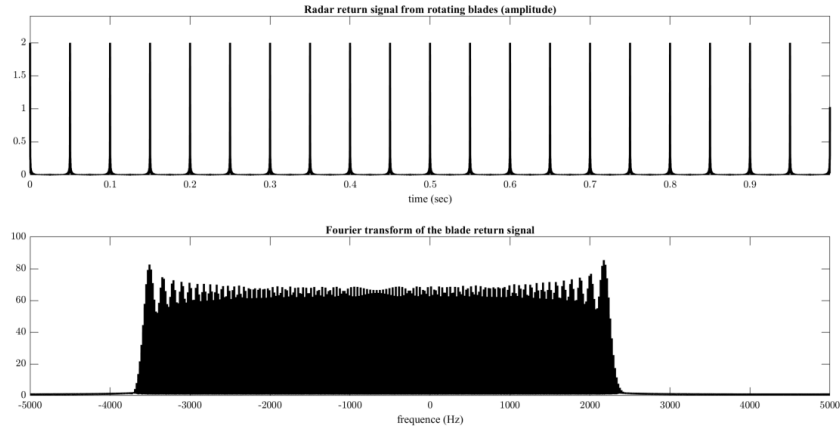


Figure 2.21: Time and Frequency response of two 1 m rotor blades at 1 m/s

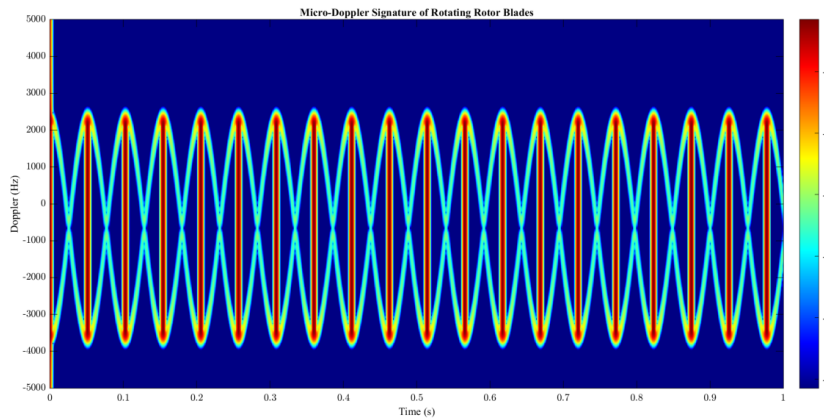


Figure 2.22: Time/Frequency representation of two 1 m rotor blades at 1 m/s

The sinc impulse train and “Flash” is seen from the main and tail rotors. The above theory and simulation yields a fundamental framework into understanding the dynamic effects of rotors on the induced μD signal. However, it approximates a constant reflectivity across the entire blade length and in all directions. This, in fact, is not true for real life signals. The following section will investigate real μD effects from drones with primarily four rotors.

UAV Micro-Doppler Model

As seen in [88], the theoretical model of the μ D return signal of a quadrotor drone is the summation of every reflecting blade from all rotors. In this paper, only a quadrotor is investigated; however, the theory is scalable. For a drone with M rotor hubs and K blades, the return μ D signature $s_r(t)$ can be stated in equation 2.32.

$$s_r(t) = \sum_{m=0}^{M-1} \sum_{k=0}^{K-1} \frac{\sqrt{\sigma_{m,k}(t)}}{L} \exp \left\{ -j \frac{4\pi}{\lambda} \int_0^L R_{m,k}(t) dL' \right\} \quad (2.32)$$

The time-varying distance or range from the radar to each point along each rotor $R_{m,k}(t)$ is integrated along the blade and scaled by $4\pi/\lambda$. The result is the time-varying phase function which modulates the propagating signal. The RCS is the ratio of the incident electric wave to return electric wave which can be thought of as a gain factor depending on blade, rotor and angle of incidence. Since the angle of incidence is a time-varying function, the RCS $\sigma_{m,k}(t)$ is also a function of time. The total reflected signal is the superposition of each blades' reflection on each rotor. Following a similar derivation found in [10] which includes the distance from radar to rotor blades, the return signal can be reduced to equation 2.33.

$$s_{\mu D}(t) = \sum_{m=0}^{M-1} \exp \left\{ -j \frac{4\pi}{\lambda} [R_m + z_m \sin \beta] \right\} \cdot \sum_{k=0}^{K-1} \sqrt{\sigma_{m,k}(t)} \text{sinc} \{ \Phi_{m,k}(t) \} \exp \{ -j \Phi_{m,k}(t) \} \quad (2.33)$$

The phase shift for each rotor hub is based on the range R_m and height z_m to each M hubs. Much like equation 2.30, the phase function (equation 2.34) is a sinusoidal signal depending on rotor rotation rate and rotation angle for each rotor hub.

$$\Phi_{m,k}(t) = \frac{4\pi L}{\lambda} \frac{1}{2} \cos \beta \cos (\Omega_m t + \phi_m + k2\pi/K) \quad (k = 0, 1, 2, \dots, K - 1) \quad (2.34)$$

The Doppler shift can be calculated as the instantaneous frequency of the phase function or the time derivative of equation 2.34 while setting the rotation angle of each blade k on rotor m to a general phase angle $\phi_{m,k} = \phi_m + k2\pi/K$. The result is a combination of sinusoidal functions for each blade on each rotor determined by geometry and distances. The return μ D spectrum will result in contributions from $m \times k$ Doppler shifts.

$$\frac{d\Phi_{m,k}(t)}{dt} = 2\pi f_{D,m,k}(t) = -\Omega_m \frac{2\pi L}{\lambda} \cos \beta [\cos \phi_{m,k} \sin \Omega_m t + \sin \phi_{m,k} \cos \Omega_m t] \quad (2.35)$$

The maximum Doppler shift will occur at the tips of each blade as the blade rotation is perpendicular to the radar. This occurs at the maximum of equation 2.35 or $|f_{D,m,k}(t)| = f_{max(\mu Doppler)} = \frac{\Omega_m L \cos \beta}{\lambda}$. Therefore the effective Doppler processing sample rate must be larger than twice $f_{max(\mu Doppler)}$ in order to avoid μ D ambiguities.

The spectrum of a quadrotor's μ D signature exhibits similar bands as the helicopter recordings in Figure 2.19. In [89] and [90], real experiments are performed to view commercial drones' spectra. In [89], a 5.8 GHz EM wave is reflected off of a S1000 Octocopter. In [90], X-Band FMCW radar recordings of a common

quadrotor DJI Phantom 2 are evaluated for μ D signature as shown in Figure 2.23. The total bandwidth lies within 5 kHz of the main body return and can be divided into sub-bands to approximate different micro motions such as the rotating blades or main body.

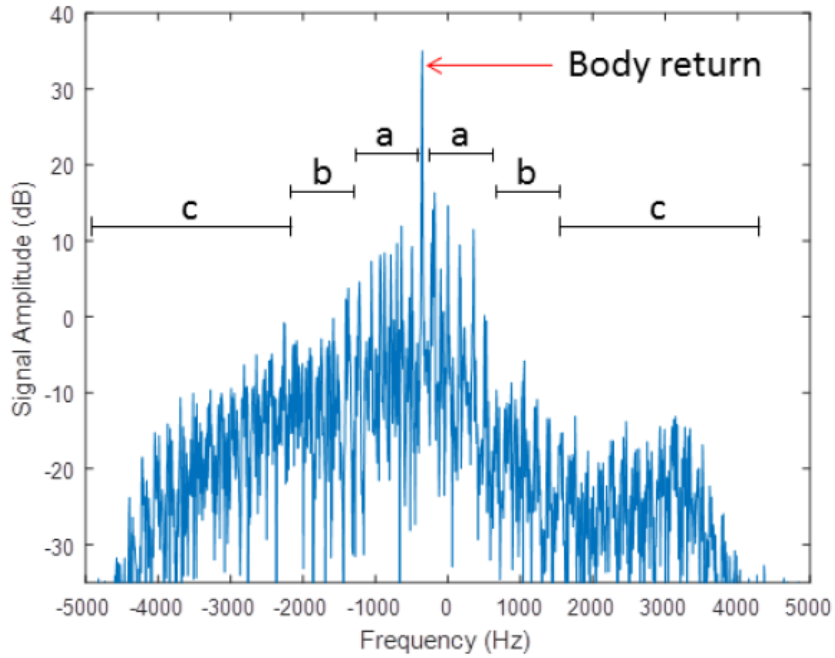


Figure 2.23: Doppler Spectrum of DJI Phantom 2 at X-Band [90]

The interference between multiple time-varying Doppler processes results in the overall spectrum exhibiting regular resonances tones. These resonances are governed by the constructive and destructive interference of the fundamental Bessel function for each Doppler contribution. Essentially, each Doppler contribution is Phase Modulation or Frequency Modulation (PM/FM) by velocity and Amplitude Modulation (AM) by RCS strength. Both the amplitude and frequency of velocity changes will effect the resulting Bessel frequency. Complex signals such as these are

often characterized by bandwidths of similar behavior. In [91], the μ D bandwidth in terms of velocity [m/s] is given for common targets.

Target	Bandwidth without μ D	Bandwidth of μ D
Walking Person	1.509	3.970
Running Person	0.873	6.273
Hovering UAV	0.158	18.818
Flying UAV	0.000	5.081

Table 2.3: Micro-Doppler Bandwidth in terms of velocity [m/s]

The μ D spectrum of a target provides low precision detail into the characteristics of a target. Ultimately, information about the time-varying nature of the target is lost across the time dimension by effectively averaging or smearing across the spectrum window. For this reason, a TFR can provide far more detail at the cost of computations and memory resources. The TFR of a simple 2-blade rotor case is shown in Figure 2.22. In [92], the TFR of helicopter and quadrotor UAVs are experimentally investigated with an X-Band CW radar. The TFRs are accurate enough to resolve the length of blades of the helicopter type. The μ D of the quadrotor is seen but less discernible due to low RCS of plastic rotors. An X-Band FMCW radar is used to evaluate an octo and hex copter. Within the range-velocity plot, distinct μ D velocities are shown at the drone range as seen in Figure 2.24.

The time variations effectively become a third dimension, and slicing the radar cube across range will effectively result in a range localized μ D TFR. Figure 2.25 shows the TFR of an octocopter hovering at approximately 85 m . The Doppler frequencies are seen to drift perhaps due to the hovering control mechanism adapting rotor speeds as needed.

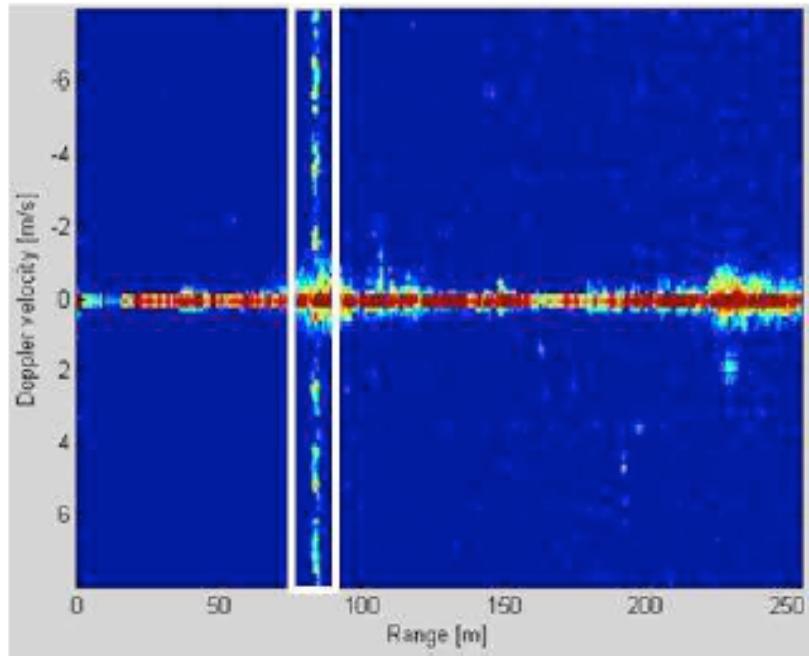


Figure 2.24: Octocopter hovering X-Band FMCW range velocity plot [92]

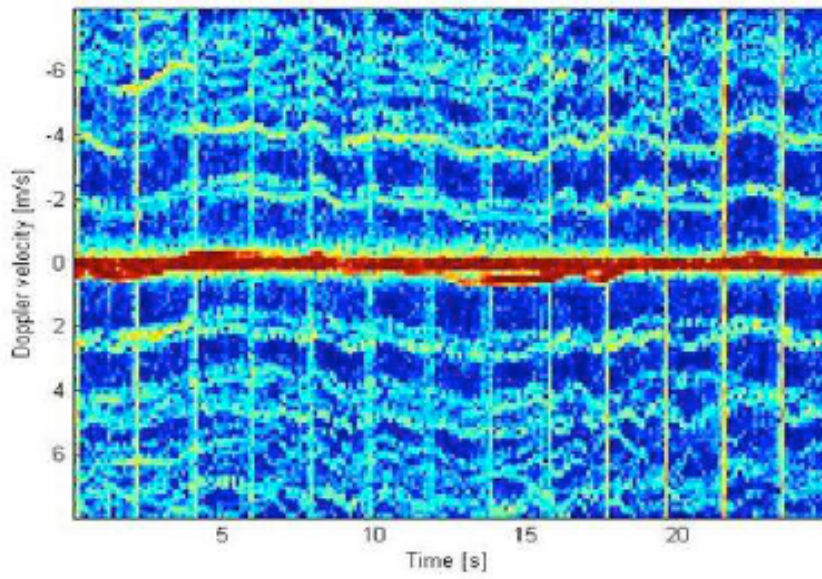


Figure 2.25: Octocopter hovering X-Band FMCW range localized TFR plot [92]

Additional experiments were performed to evaluate the μ D TFR of a DJI Inspire at L-Band [93]. Also in [94], octocopter, quadcopter and nano-quadcopter are compared at 35 GHz. One issue with μ D analysis is the detecting of only radial velocity creating a dependence on radar LOS. Recently, the use of interferometric sensors to detect angular velocity has been investigated. The interferometer operates by mixing return signals from antennas spaced at a specific distance apart. The azimuth angle of a target will cause a distance or phase difference between receivers. An angular velocity causes a detectable phase change or frequency. Experimental investigations of UAV angular and radial velocities show discerning characteristics. Angular velocities show potential for secondary features accounting for the LOS dependency [95, 96].

2.4.2 Micro-Doppler Identification Challenge

The challenge is creating a real-time, reliable technique to differentiate between UAVs μ D signatures. From the first formulation of the μ D effect to recent attempts at machine learning, significant advances in understanding and interpreting how EM signals reflect off complex targets fuel identification techniques. Identification can be interpreted as a machine learning classification problem. Within every classifier, two distinct functions exist: feature extraction and the classifier itself. Classifiers are application independent, and comprehensive research has already been conducted to determine the potential of each [97, 98]. Feature extraction is highly application specific and requires intuitive understanding of the dataset. The resulting performance is a product of physical understanding, intuition and real dataset evaluations. However, the existence of a comprehensive UAV μ D

database ultimately determines how practical the results can be. Few databases are currently published [99], and few research labs have the capability to generate and evaluate comprehensive UAV radar μ D identification databases. Given the project history of **DU²SRI** and our UAV fleet size, a unique potential to explore novel μ D research including feature extraction and frequency band comparisons can be explored. Currently, **DU²SRI** has an extensive fleet of fixed wing, helicopter, and quadrotor commercially and custom built UAVs to evaluate RTI algorithms.

2.4.3 Time-Frequency Micro-Doppler Representation

Many attempts at classifying targets based on TFRs or Time-Frequency Distributions (TFDs) have been explored and published. The first analysis of the phenomenon and its time-frequency transform was published in 2000 by Victor C. Chen [10]. He is commonly known as the father of μ D and is cited numerous times for his ground-breaking work in demystifying and laying the fundamental theory this research field builds from. His initial work contains mathematical models of the time-frequency domain representation of μ D signatures induced from vibrations, rotations, human gait and rotating antennas. A Gabor transform was used to experimentally confirm his TFR using empirical data. The Gabor Transform is a STFT using a Gaussian window function.

TFRs are generally classified by the mathematical transform applied to the single dimension radar echo resulting in a 2-dimension representation. Due to the *Uncertainty Principle of Signal Processing*, the product of the time-duration σ_t and bandwidth σ_w of a signal are bounded by $\frac{1}{2}$ [equation 2.36]. In this case, the

time-duration and bandwidth are defined as the standard deviation of the energy distribution in the time and frequency domain.

$$\sigma_t \cdot \sigma_w \geq \frac{1}{2} \quad (2.36)$$

Due to this fundamental law, efforts have been made to find the best Time-Frequency Transform (TFT) or optimize a parameterized TFT to best suit an application. TFT are generally categorized as linear, such as the STFT, or bilinear, such as the Wigner-Ville Distribution (WVD). Bilinear transforms may have better time-bandwidth characteristics but suffer from cross term interference due to their dependence on overlapping local time and frequency characteristics. A final class of linear TFRs known as *Wavelets* are essentially generalized STFT in which a time window function is incorporated into the kernel of the Fourier transform to ultimately optimize for exploiting time or frequency characteristics. As a result, Wavelets tend to be interpreted and defined from a “scale” point of view, rather than a frequency point of view.

2.4.4 Feature Extraction

Feature Extraction is the method of mathematically formulating characteristics or features of a certain signal to model real-life dependencies and separate different physical phenomena. In the case of μ D RTI, features should be formulated to differentiate different targets due to their μ D signature. A feature can be low resolution and use approximate statistical calculations or high resolution using known

physical models. The trade-off is fundamentally between computational efficiency and performance.

TFR Features

The TFR itself is an attempt at exploring differences in μ D signatures and can be used as a high dimensional feature space. Each pixel in the two-dimension spectrogram picture is a single feature in the feature space. The downsides with high-dimensional feature spaces are the required computational needs for classifiers and the potential for over-fitting. Attempts have been made to apply Principle Component Analysis (PCA) to the TFR in order to reduce the dimensionality to the most influential features. PCA is a common research method of finding the eigenvectors and eigenvalues of a co-variance matrix of some dataset using eigen decomposition. The eigenvectors become the orthogonal basis functions ranked from most to least variance based on the corresponding eigenvalues. Singular Value Decomposition (SVD) is a numerical solution to approximate PCA. The following papers all attempt some variant of PCA in order to dimensionally reduce the feature space defined by some μ D TFR [100, 101, 102].

In [100], the authors use an X-Band Doppler radar system to classify planes, quadrotors, helicopters, stationary rotors and birds by extracting an STFT using a Hamming window. The STFT is first pre-filtered with an adaptive noise filter. After the STFT, the bulk target velocity is tracked and centered. Radar measurements were performed within the Dutch Radar Centre of Expertise and included 11 different targets. The principle components of the linear TFR are calculated and used to train a linear/non-linear Support Vector Machine (SVM) and a naive Bayesian classifier.

After 10-fold cross validation, the best performance was the non-linear SVM at 95% accuracy.

In [101], the authors claim to use robust PCA based on a Minimum Covariance Determinant (MCD) applied to the STFT Mean Frequency Profile (MFP) analysis of the *RadEch Database* [99]. Essentially, the time-average across frequency is calculated followed by an outlier-robust PCA extraction. An SVM classifier learns from up to the 50 features and is ultimately implemented on a TI DSP chip (TMS320C6713). Random validation evaluates acquisition time, from 0.5 to 4 seconds, vs. feature space. Results ranged from 82% to 94%.

In [102], authors investigate computationally simple features for discerning between birds, fixed-wing UAVs and rotor-based UAV targets. The authors report that target velocity, spectrum periodicity and spectrum width are sufficient features for classifying birds vs. UAVs based on μ D and scattering theory. For discerning between fixed and rotor-based targets, an X-Band CW radar samples μ D signatures of a Vertical Take Off and Landing (VTOL) and flying-wing mini-UAV at 96 kHz and SVD dimensional reducing algorithm is investigated. First, an STFT is computed with the appropriate sample rate, integration time and window overlapping. Then the TFR matrix $\mathbf{X}(v, t)$ is decomposed into left (\mathbf{U}) and right (\mathbf{V}) singular vectors according to equation 2.37.

$$\mathbf{X} = \mathbf{U}\mathbf{\Sigma}\mathbf{V}^T \quad (2.37)$$

The diagonal matrix $\mathbf{\Sigma}$ contains the singular values which represent a metric for how much information is contained within the respective left and right singular vectors. The singular vectors are projections of \mathbf{X} onto two principal bases decoupling

velocity and time information from each other. The results of the first few left and right (velocity and time) vectors contain easily seen rotor rotation rate and μ D bandwidth. Using these values, an estimate of rotor length L is calculated via equation 2.38.

$$L = \frac{BW}{2\pi\Omega} \quad (2.38)$$

The previous attempts at target identification use similar methods to reduce feature space dimensionality of TFR to only the principle components in order to robustly classify UAVs characteristics. The results are promising but inherently STFT and other linear TFRs have limited time-variant resolutions. The following section explores more complex TFRs and μ D specific features.

TFR-Based Feature

Measuring the time-varying characteristics of the μ D signature has a direct correlation to the real micro motion of the target. One obvious representation can be achieved by taking the FFT along each velocity bin across a longer time window. The second FFT across time has an effective sample rate of $\frac{f_s}{Window\ Length \times Overlap}$. As a result it can be called the “slow-time” FFT or the “cadence” to not confuse with the previous Doppler processing “slow-time” terminology. The cadence can be plotted on a Cadence vs. Velocity Diagram (CVD) and be used to estimate human gait or rotor rotation speed. A second TFR-based feature is called the cepstrum. The cepstrum was first theorized in 1963 by Bogert et al in his seminal paper [103] as an analysis tool for periodic motion within a spectrum. It is defined as the Inverse

Fast Fourier Transform (IFFT) of the logarithm of spectrum or windowed FFT of a signal represented in equation 2.39. Today it is commonly used in speech analysis.

$$C(f_{que}) = \mathcal{F}^{-1}\{\log(|\mathcal{F}\{f(t)\}|^2)\} \quad (2.39)$$

In [94], cadences and cepstrum of octocopters, quadcopters, and nano-quadcopters are calculated with recordings from a 35 GHz CW radar and plotted in Figure 2.26. In the CVD plots, the distinct vertical lines suggest oscillatory behavior of the TFR at distinct cadences. This could be due to rotor rotation and the flash of the blade. The nano-Quad lacks cadence possibly due to high blade rotation rate relative to sample frequency. The cepstrum plots the que-frequency and reveals distinct periodicity. The periodicity is most likely caused by the rotation of the blades and thus is a measure of blade rotation rate. Multiple que-frequency peaks can result from multiple blades rotating at difference speeds or harmonic distortion.

The TFRs are decoupled and decomposed using SVD and averaged across velocity and cadence. The resulting features are run through a Radial Basis Function (RBF)-SVM classifier and five-fold cross validated. The result was above 96% accuracy when comparing birds to UAVs or small-size UAVs to medium-sized UAVs. The rotor length was also estimated accurately from CVD or cepstrum. The results suggest high performance when differentiating types of targets however do not investigate a large fleet or sub-types of UAVs such as rotor number or fixed-wing aircraft. In [104], helicopter and octocopter UAVs cepstrum are calculated and plotted with an X-Band CW radar. The authors suggest cepstrum for low sample rate acquisition or differentiating between bio-life and UAVs.

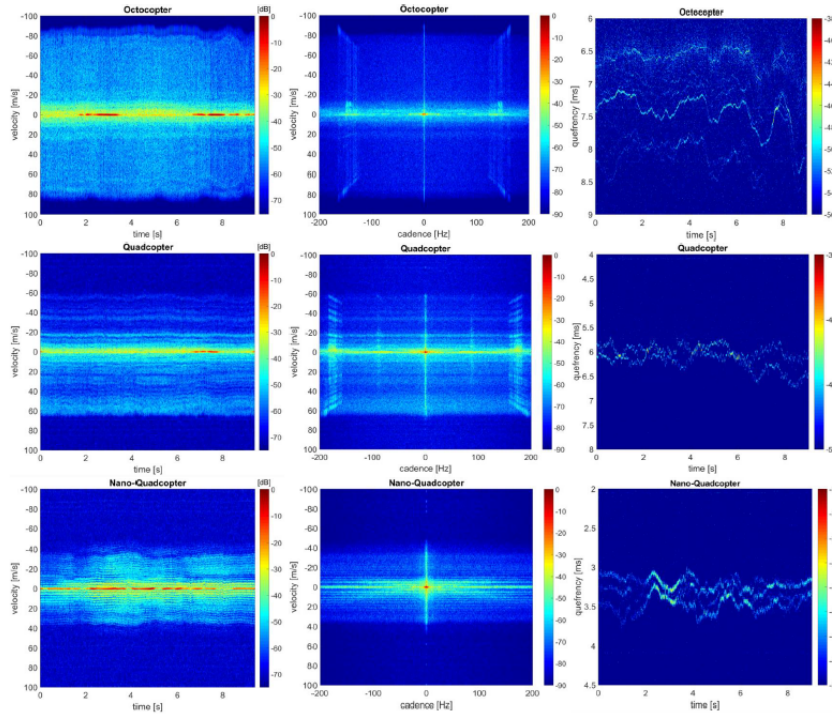


Figure 2.26: TFRs, Cadence and Cepstrum Features for Octo/Quad/Nano UAV [94]

EMD Features

A downside of CVD and cepstrum-based spectrum periodicity calculations is that STFT and WVD TFRs suffer from lack of resolution or computational complexities. Another approach to decompose μD into fundamental periodic components called IMFs is EMD. EMD can be effective for μD analysis with the addition of Hilbert Huang Transforms. An IMF has only one instantaneous frequency at a time, an equal number of maximum/minimum extrema to zero-crossings, and is locally zero-mean across all time. An IMF is found by first sifting to find extrema, then interpolating with a cubic spline. Lastly, the median is subtracted out. The first IMF is subtracted

from the original signal and the process is repeated. Essentially, EMD is a time-based calculation of fundamental frequencies and their time-varying contribution.

In [105], simulations and experiments of rotor blades' EMDs are analyzed and shown to carry information for RTI classifiers. Figure 2.27 shows the IMFs of a simulated single 2.5 *m* blade rotating at 300 RPMs. The IMFs carry both frequency and time-varying information of targets. The use of EMD will still result in a high-dimensional feature space and therefore statistically and geometrically calculated features are derived from the IMFs [106]. A few EMD-based features such as zero-crossings, IMF energy, standard deviation, entropy, frequency peak and a fusion of all are investigated for classifying distinct fixed-wing and rotor-based UAVs, birds and stationary rotors. Using SVM classifiers and similar data, the error rate is compared with other common features such as TFRs, CVDs, cepstrum and regularized complex-log FFTs. The EMD-based features yields best results [106].

Micro-Doppler Reconstruction Features

Estimating UAV characteristics from its μ D signal has also been theorized and evaluated. Characteristics such as the number of rotors, rotor length, rotation rate, target speed, and target size can lead to estimating the aerodynamics and potential trajectories of the UAV. Such characteristics can ultimately benefit SAA systems by improving the avoidance maneuver. The blade flash phenomenon is an ideal candidate for determining rotation rate. The blade flash is a wide-bandwidth, short-time event appearing as an envelope peak across multiple IMFs [107]. Ordering the IMFs according to its blade flash contribution and reconstructing the signal from a select number of contributing IMFs will enhance the flash observed in a TFR.

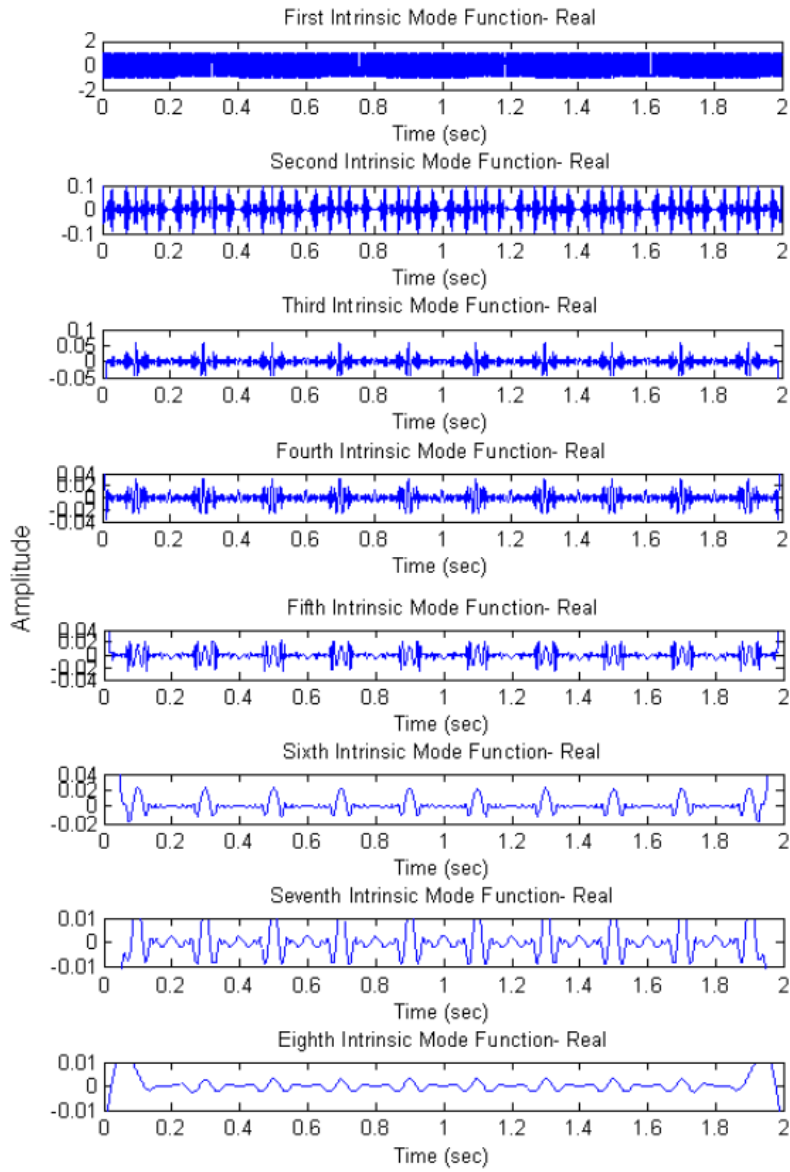


Figure 2.27: First Eight simulated IMFs for single blade target (300 rpm / 2.5 m) [105]

The algorithm in [107] is experimentally evaluated and shows distinct flashes for helicopter and quadcopter UAVs.

In [108], Yichao Zhao et al. analyze the estimation of parameters of the μ D model from [10, 88] in equation 2.33. Simplifying the model with focus on periodic velocities and including phase noise $\psi(t)$ results in equation 2.40. The μ D signal is a superposition of potentially infinite micro-motion frequencies f_k with a complex coefficient D_k . The target bulk velocity is incorporated into $V(t) = -\frac{4\pi}{\lambda}vt$. The range and reflectivity are incorporated into a complex factor $K = \sigma \exp \left\{ -j\left(\frac{4\pi}{\lambda}R_0\right) \right\}$. The μ D signal is a combination of Amplitude Modulation and Phase Modulation (AM-PM) where K represents the AM and the summation of infinite sinusoidal functions is the Phase Modulation (PM).

$$s_{\mu D}(t) = K \exp \left\{ j \left[\sum_{k=0}^{\infty} D_k \exp \{ j2\pi f_k t \} + V(t) + \psi(t) \right] \right\} \quad (2.40)$$

Using a process called Cyclostationary Phase Analysis (CPA), an estimate of the μ D parameters (D_k, f_k) can be made. When analyzing random processes, a stationary process does not exhibit dynamic statistical behavior such as mean or standard deviation. A cyclostationary process experiences periodic statistical behavior. It is defined as a zero-mean signal whose Auto-Correlation Function (ACF) is periodic. The ACF has a peak at the expected value or mean. If the expected value is cyclical, a periodic peak occurs. Using the fundamental period T_0 of the expected value, the Fourier series coefficients $R_x^\alpha(\tau)$ of the ACF $R_x(t, \tau)$ are often referred to as the Cyclic Auto-correlation Function (CAF) defined in equation 2.41.

$$R_x^\alpha(\tau) = \frac{1}{T_0} \int_{T_0/2}^{T_0/2} R_x(t, \tau) \exp(-j2\pi\alpha t) dt \quad (2.41)$$

The spectral density of each coefficient is called the Cyclic Spectrum Density (CSD) $S_x^\alpha(f)$ defined in equation 2.42.

$$S_x^\alpha(f) = \int_{-\infty}^{\infty} R_x^\alpha(\tau) \exp(-j2\pi f\tau) d\tau \quad (2.42)$$

The amplitude of the CSD can be put into the form of a Bessel function of the first kind. Thus, a CSD of a μ D signal is a measure of the expected fitted Bessel function and can be used to estimate the fundamental μ D parameters. The performance of the CPA parameter estimation of the PM μ D signal (CSDP) given phase noise is evaluated with field experiments and Monte Carlo simulations. The results show robust parameter estimation to distinguish UAVs from other non-cyclostationary interference signals such as platform movement. The estimates of D_k and f_k are asymptotically optimal above -4 dB.

2.4.5 Neural Networks

Artificial Neural Networks (ANNs) have reemerged in recent years due to computational hardware advances. An ANN essentially mathematically models the human brain and its layers of neurons and can be trained to perform most known mathematical functions. They essentially combine the mathematics of feature extraction and classification into one network of layered summations with activation functions. However, the downside with ANNs are their inherent complexity in implementation and training. ANNs require large computational units and datasets for effective training. Research using ANNs for a wide variety of applications is a large and growing field with too many facets to cover in a single thesis. A cursory search

of ANN μ D RTIs yield many attempts at using fully-connected [109], convolutional neural networks [110] and deep belief networks [111]. Due to large training sizes and complexity, this method of RTI is still in its infancy and maturing. The development of a comprehensive training set for ANN μ D RTI remains a fundamental limitation of such machine learning techniques.

2.5 Adaptive Radar

Until recently, applying information and/or control theory into the design of the radar waveform in order to maximize performance has been strictly theory [112, 113]. A few waveform techniques were technically feasible with a meaningful performance increase. Examples such as Linear Frequency Modulation (LFM), stepped frequency modulation, waveform spectrum shaping, and binary phase codes [30] are common in modern military and commercial systems given a particular application and performance need. Recently, the concept of CR has emerged and advances in the mathematical frameworks and SDRad have enabled implementation.

2.5.1 Cognitive Radar

The idea of CR and resulting Fully Adaptive Radar (FAR) frameworks were theorized and generalized [11] as early as 2006. The concepts behind cognitive sensing systems are simple but with many interpretations. Fundamentally, it is using information about the sensing environment and target from prior measurements to adaptively sense the target with higher performance. Conceptually, Figure 2.28 shows Simon Haykins' original concept of Cognitive Radars in 2006. The fully-

feedback, statistical based tracker uses past and present environmental models from active sensors and *a priori* knowledge to intelligently track the target by adapting the transmitter to optimal parameters. The concept is borrowed from the echolocation system of a bat, which uses complex calls for high resolution range for velocity ??.

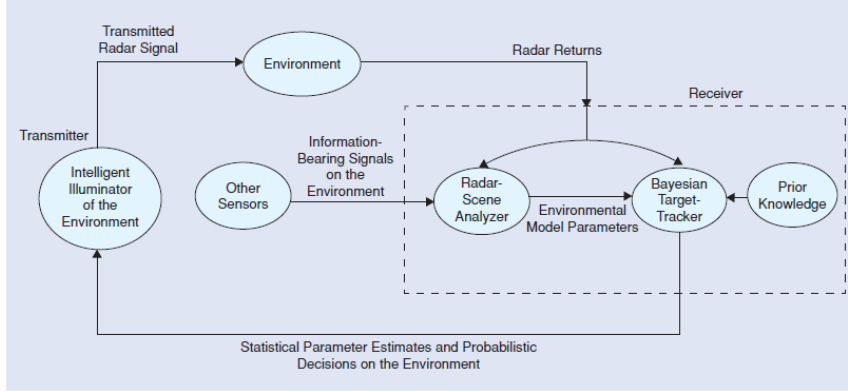


Figure 2.28: Simon Haykins original concept of Cognitive Radar [11]

2.5.2 Fully Adaptive Radar Framework

Statistically-based models driving complex optimal control algorithms to determine the best radar parameters for detecting or tracking targets are currently being investigated. Kristen Bell et al provided the mathematical framework using optimal control theory [114, 115, 116, 117]. The sensor, with its internal parameters θ_k , senses the target state \mathbf{x}_k and makes a measurement z_k . All sensor measurements and parameters up until the current time t_k are denoted as matrices $\mathbf{Z}_k = \{z_1, z_2, \dots, z_k\}$ and $\Theta_k = \{\theta_1, \theta_2, \dots, \theta_k\}$ respectively. Figure 2.29 is the proposed control theory framework which estimates the target state $\hat{\mathbf{x}}_k(\mathbf{Z}_k)$ by minimizing the processor cost function $C(\hat{\mathbf{x}}_k(\mathbf{Z}_k), \mathbf{x}_k)$. The controller loss function $L_{C,\Theta}(\cdot)$ balances the processor cost function with the sensor cost function $R_\Theta(\cdot)$ to determine the sensor parameters.

A Markov motion model with a Probability Density Function (PDF) $q(\cdot)$ statistically models the next target states given the previous target states and the current sensor parameters. The sensor measurement function $f(\cdot)$ is another PDF modeled function to observe the target states given target and sensor parameters. A posterior density function $f^+(\mathbf{x}_k) = f(\mathbf{x}_k|\mathbf{Z}_k; \Theta_k)$ is effectively a measurement of the sensor measurement function accuracy given prior observations and sensor parameters. It helps the controller perceive the environmental effect on the target state estimator. The FAR framework has been solved for tracking and detection of radar targets by initializing, adapting and optimizing radar sensor parameters [116, 117, 118]. Theory has also been scaled to MIMO networks or distributed cognitive radars [119], and performance metrics for complex CR systems are proposed [120]. The theory has also been implemented in an SDRad, and initial experiments for performance yield promising results [121, 61, 122]. One strong conclusion resulting from the CR experiments are the bridging of radar performance to processor and sensor costs. This results in optimal radar performance cost on its hardware resources. The concept can be extended into the radar development process to provide optimal hardware design requirements for a given set of performance goals.

For most radar systems, implementing a FAR system is not yet feasible and thus multi-mode or multi-function systems which integrate different radars for separate functions have been implemented for performance sensitive applications like fighter aircraft [40]. The complexity of the control method can range from simple multi-mode operation to a fully analytic feedback control model with real-time data acquisition. The latter requires significant computational resources and is severely limited by system latency. The flexibility of an SDRad provides the ability to switch radar

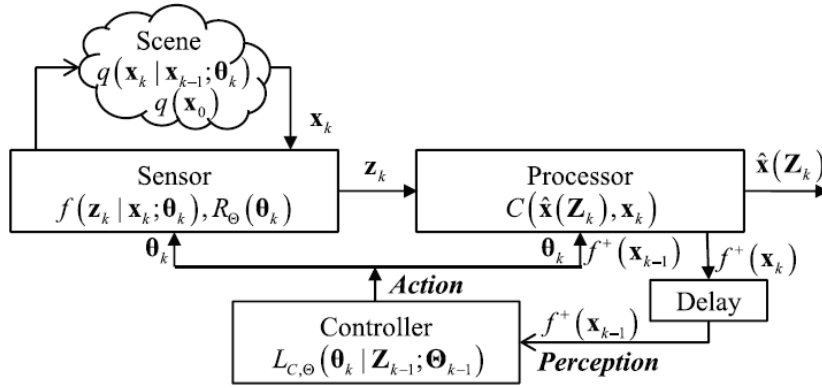


Figure 2.29: Fully Adaptive Radar (FAR) Framework [115]

parameters in real time to implement multi-mode or FAR frameworks as needed. For UAV SAA applications the payload or sensor cost in SWaP is directly related to computational needs and sensor transmit power. A CR has the potential to meet the high performance needs by optimizing computation and sensor costs.

Chapter 3

Radar Testbed

In signal processing and machine learning design, the engineer needs to evaluate the effectiveness of an algorithm. Evaluations can be performed on software simulations (models) or by taking real world measurements depending on the application. For machine learning, or more generally, statistics-based classifying of real world data, it is important to test the algorithm on data captured in the same manner as in the field. For the purpose of testing CR and μ D RTI, a SDR based radar system was developed to capture real radar data for the evaluation of such algorithms or techniques.

3.1 Design Considerations

For the purposes of current and future research, a flexible, software-defined Frequency Modulation (FM) radar is needed to perform and compute the adaptive processes of CR and μ D RTI. The testbed will be used primarily within the context of research and development within applied science laboratories and thus it must

account for large, dynamic problem spaces as efficiently as possible. Fortunately, advances in MMIC and System on a Chip (SoP) for sensor or radio applications provide software control of hardware parameters with a degree previously not possible. This allows potential for rapid prototyping of novel research concepts by simply programming solutions into a capable system. In fact, the overarching novelty of this research is the potential this repeatable design has to provide rapid radar development at a low entry cost point through the use of commercially (or open source) available systems, components and development environments.

3.1.1 Problem Space

The design considerations are limited or constrained by the CAS problem space. Radars prove to be a reliable and robust SAA solution for performing the necessary *Functions* (DTI) on the given *Targets* (FAA Part 107 UAV) given the *Environmental* limitation such as atmospheric effects and airspace definitions. The design considerations themselves start by defining radar performance requirements to satisfy the problem. The radar type/technique and overall system architecture is then carefully selected to meet the performance needs while minimizing engineering and component costs. Finally, the performance is controlled by a set of programmable hardware design parameters. Thus providing rapid prototyping and the ability to meaningfully change between different solution sub-spaces or functions. Some major parameter decisions consist of the transmit frequency, receiver sensitivity, bandwidth, RSP parameters, and data processing limitations. Defining the problem constraints provides context as seen in Figure 3.1.

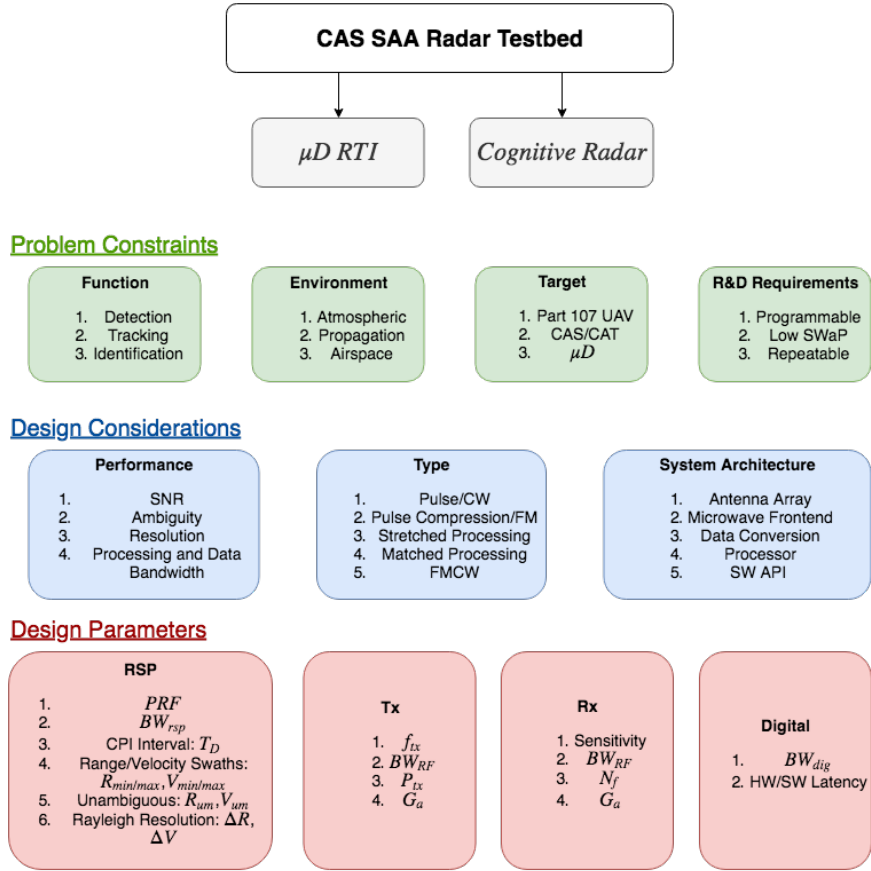


Figure 3.1: SAA Radar Testbed Problem and Design Space

The targets in this case are “small commercial UAVs” as defined by FAA flight rules Part 107 [2]. The flight of UAVs under Part 107 are limited by weight (**50 lbs**), height (**400 feet**), speed (**100 mph**), area (not over people or by airports) and within LOS of pilot or operator. The SAA requires DTI of targets. The maximum range performance is defined as the CAT or the distance required for the SAA system to have enough time for collision detection and successful avoidance. From Section 2.1.1, a maximum frontal CAT distance for Part 107 UAVs are found to be 600 *m*. This formulation assumed a beyond worst-case scenario and a more reasonable range

of performance is 100 – 300 *m* with focus on close-range tracking in order to supply avoidance algorithms with sufficient sensory data. The maximum velocity performance is defined as the twice the maximum allowable Part 107 UAV speed or 200 *mph* (≈ 90 *m/s*). The appropriate resolution of range and velocity is determined by which function the radar is performing. Typically, tracking requires much higher resolution than detection. Identification typically requires higher velocity resolution than detection or tracking. This research investigates opportunities for advancing DTI of FAA Part 107 UAV targets.

3.1.2 Transmit Frequency

The selection of the transmit frequency directly affects the system performance in a variety of ways. First, for electromagnetic reflectometry, radio frequency or microwaves are used due to their inherent robustness to obstacles such as atmospheric or landscape effects which overwhelm LiDAR, infrared or visible light sensing systems. Figure 3.2 shows the relative transmission losses of EM waves with frequencies from microwaves to ultra-violet over 1 nautical mile at sea level. The microwave region has significant bandwidths available without atmospheric effects. Visible light and IR have windows of low absorption losses, but scattering effects begin to dominate due to small wavelengths relative to particles in the atmosphere. Thus, atmospheric absorption from scattering or other effects need careful consideration in any CAS.

Fundamentally, the usable frequencies within the millimeter and microwave bands are further limited by target scattering, free space loss, atmospheric absorption and Doppler effects, all of which have large dependencies on the choice of transmit

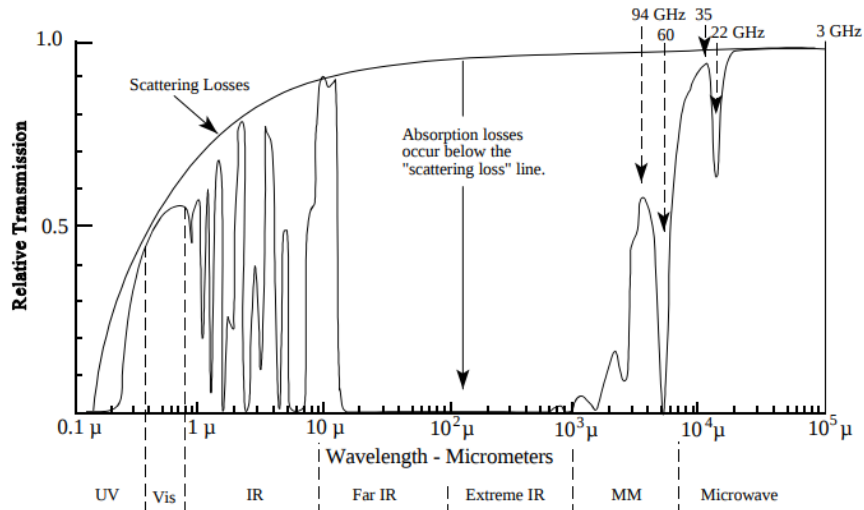


Figure 3.2: Atmosphere Absorption and Scatter Losses [123]

frequency. Figure 3.3 shows the IEEE standardized radar bands found in IEEE Std 521-2002 [124]. Typical aircraft detection is found within the S-Band or below. Typical aircraft tracking is found at X-Band or above. Identification is highly dependent on targets scattering effects. The following sections briefly overview EM scattering, atmospheric, and Doppler effects and their relationship to transmit frequency and a UAV target.

Scattering Theory

In scattering theory, if the internal state or kinetic energy of the scattering particle or medium is unchanged after the collision, the process is called elastic scattering [125]. Microwaves typically do not have enough energy to interact in-elastically with common materials. Hence, the scattering effect of radar systems is simply a matter of which direction the energy has scattered towards. The scattering effects of an object depend on its material, size and geometry. There are two basic categories

International table				
Band designation	Nominal frequency range	Specific frequency ranges for radar based on ITU assignments (see Notes 1, 2)		
		Region 1	Region 2	Region 3
HF	3–30 MHz	(Note 3)		
VHF	30–300MHz	None	138 –144 MHz 216– 225 MHz (See Note 4)	223-230 MHz
UHF	300–1000 MHz (Note 5)	420–450 MHz (Note 4) 890–942 MHz (Note 6)		
L	1–2 GHz	1215–1400 MHz		
S	2–4 GHz	2300–2500 MHz		
		2700–3600 MHz	2700–3700 MHz	
C	4–8 GHz	4200– 4400 MHz (Note 7)		
		5250–5850 MHz	5250–5925 MHz	
X	8–12 GHz	8.5–10.68 GHz		
Ku	12–18 GHz	13.4–14 GHz		
		15.7–17.7 GHz		
K	18–27 GHz	24.05–24.25 GHz	24.05–24.25 GHz 24.65–24.75 GHz (Note 8)	24.05–24.25 GHz
Ka	27–40 GHz	33.4–36 GHz		
V	40–75 GHz	59–64 GHz		
W	75–110 GHz	76–81 GHz		
		92–100 GHz		
mm (Note 9)	110–300 GHz	126–142 GHz		
		144–149 GHz		
		231–235 GHz 238–248 GHz (Note 10)		

Figure 3.3: IEEE Radar Bands [124]

of materials based on their electrical and magnetic characteristics: conductors and non-conductors. Conductors essentially allow for easy movement of free electrons and thus electric and magnetic fields are quickly resolved through conductive currents and do not propagate easily. Non-conductors, commonly known as dielectrics, propagate energy indirectly through displacement currents [41]. The speed of propagation is a function of a fundamental EM characteristic called the *Dielectric Constant* D_k . At the interface of dielectrics, the speed of propagation changes resulting in a reflection of a portion of the incident wave. Appendix C.1 provides a more fundamental review of electromagnetic material theory.

Radar Cross Section

Radar engineers are typically concerned with how much energy is scattered back in one direction. This, appropriately called *backscatter*, can be measured as the RCS σ . The RCS is defined as the ratio of incident power density and reflected power density of a given target at significant distances from the transmitting antenna. RCS has units of square meters but is not a measure of projected cross section. The units are a product of the definition containing power densities with units of W/m^2 . In order to understand the significance of RCS, one must investigate how it affects power radiating within a radar system. The power density incident upon a point target S_t can be described as the isotropic transmitted power density scaled by the antenna gain G_a in the direction of the target. The power density is calculated from the power transmitted P_t scaled by the surface area of a sphere at a distance R from the transmitter.

$$S_t = \frac{P_t}{4\pi R^2} G_a \quad W/m^2 \quad (3.1)$$

The isotropic backscatter can be defined as equation 3.2 which includes the RCS factor to represent the power backscattered P_b from the incident power density. The backscatter power is radiated isotropically and is thus scaled by the area of a sphere.

$$S_b = S_t \frac{\sigma}{4\pi R^2} = \frac{P_b}{4\pi R^2} = \frac{P_t G_a \sigma}{(4\pi)^2 R^4} \quad W/m^2 \quad (3.2)$$

Finally, the power received P_r includes the effective aperture size of the receive antenna A_e , free space path losses $(\frac{4\pi R}{\lambda})^2$, system losses L_s and atmospheric losses L_a . Equation 3.3 is one form of a monostatic *radar range equation*. The RCS

can be seen as a factor which represents the ability of a target to reflect a given transmitted frequency at a specified range, system power, gain, and loss parameters. From equation 3.2, a formal definition of RCS is defined as 3.4 by expressing the relationship in terms of the complex electric field amplitudes and guaranteed far field conditions.

$$P_r = \frac{P_t G_a A_e \sigma}{(4\pi)^2 R^4 L_s L_a} = \frac{P_t G_a G_r \lambda^2 \sigma}{(4\pi)^3 R^4 L_s L_a} \quad W \quad (3.3)$$

$$\sigma = 4\pi R^2 \frac{S_b}{S_t} = 4\pi \lim_{R \rightarrow \infty} \left[R^2 \frac{|\vec{E}_b|^2}{|\vec{E}_t|^2} \right] \quad m^2 \quad (3.4)$$

The max RCS generated from a few common shapes is illustrated in Figure 3.4. The calculations assume the maximum dimension of the object is much greater than the wavelength of transmitted frequency and the material is conductive. Also, the maximum RCS is not always related to the projected cross section of the object.

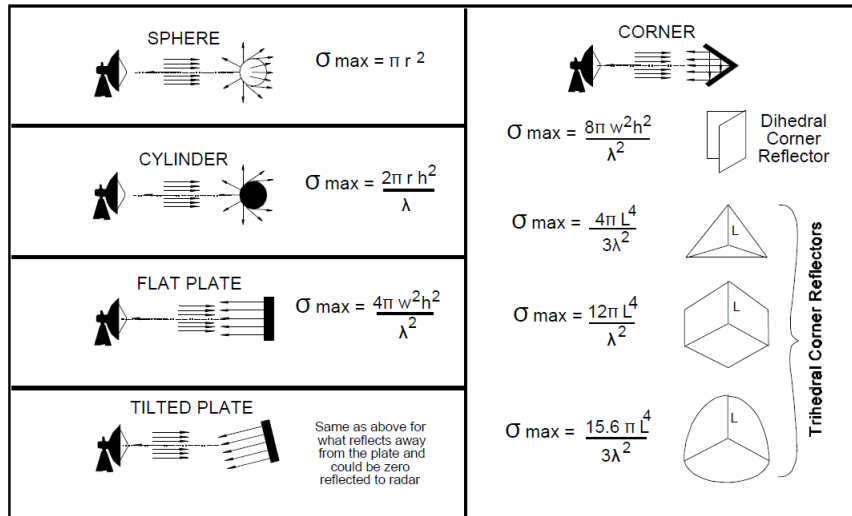


Figure 3.4: RCS of common geometric shapes [123]

Scattering

To understand the effects of electrical size on EM scattering, Figure 3.5 shows the relationship between the size of a conducting sphere expressed in wavelengths and the RCS normalized to the maximum RCS from Figure 3.4. A sphere has full three dimensional symmetry and thus makes a good object for scattering investigations. EM scattering can be separated into three regions depending on the relationship between wavelength and object size. When $\lambda \ll 2\pi r$, RCS is not dependent on wavelength and is equal to πr^2 . This is known as the *Optical* or geometric region, where waves behave by the laws of ray tracing. The region where $\lambda \gg 2\pi r$ is called the *Rayleigh* region. The RCS exhibits a dependence on the wavelength due to the whole object at any given moment experiencing a uniform electric field, pushing all free electrons to one side and inducing a dipole. From antenna theory, dipoles are understood to radiate almost isotropically with broadside gain increasing with frequency [126]. When $\lambda \sim 2\pi r$, resonances occur due to the constructive and destructive interference between immediately reflected specular waves and creeping waves created by diffuse waves following the shadow of the sphere around the backside. This region is considered the *Mie* region. A maximum occurs at point A when $\sigma = 4\pi r^2$ and minimum at point B when $\sigma = 0.26\pi r^2$.

Atmospheric Absorption

The propagation of millimeter and microwaves requires suitable transmit powers to overcome atmospheric absorption. Absorption is fundamentally caused by the inherent dielectric loss of a material. The lag response of the molecular dipole moment to propagating waves creates friction dissipated as heat within the material.

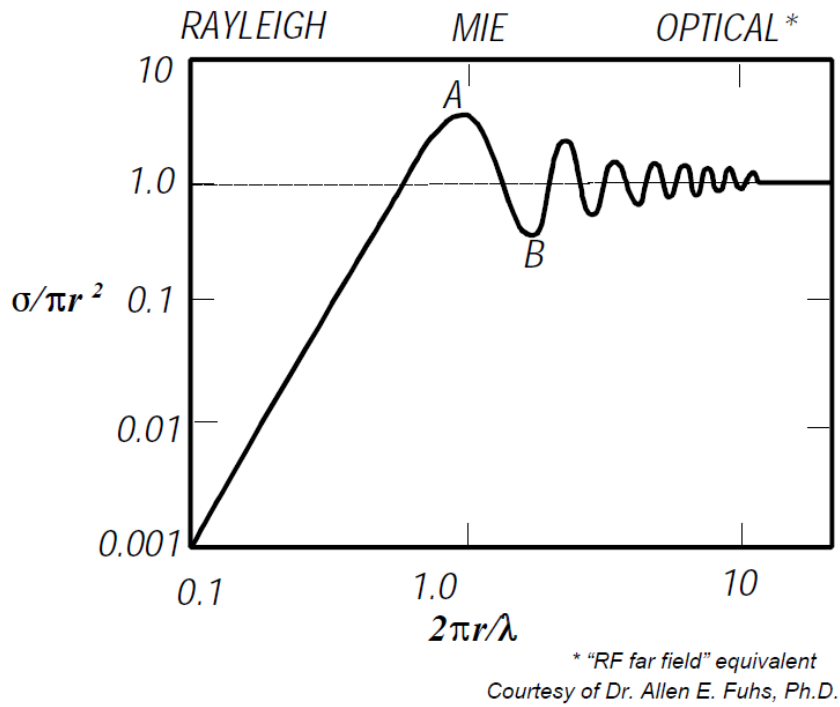


Figure 3.5: Scattering of sphere [123]

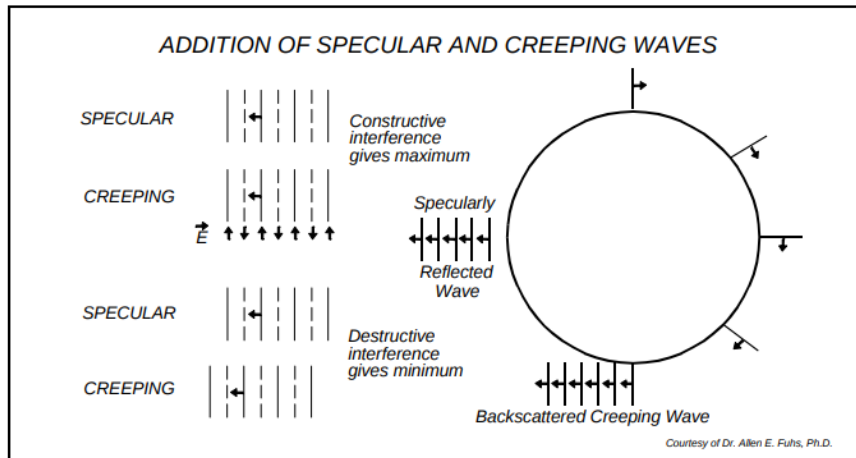


Figure 3.6: Creeping Waves for Mie region scattering [123]

It is measured as the loss tangent. Scattering effects can enhance absorption due to multi-path effects. Absorption effects are typically dominated by water moisture and

oxygen particles which contain peaks along a generally increasing trend as frequency increases across the microwave region, shown in Figure 3.7. The peaks are caused by resonances between molecular dipoles and the transmit frequency. One cause of the increasing trend is minor Rayleigh scattering. As seen on the plot above 10 GHz, IEEE radar X-band, water vapor absorption increases dramatically and peaks at 23 GHz. The oxygen absorption peaks around 65 GHz and 135 GHz, IEEE radar V, W, and mm bands, prevent effective long distance detection at these bands. However, atmospheric effects can also be used to the radar engineer's advantage as seen in weather radar, automotive radar sensors using oxygen absorption peaks to prevent system-to-system interference, and satellite-to-satellite communications using peaks in order to prevent ground reception.

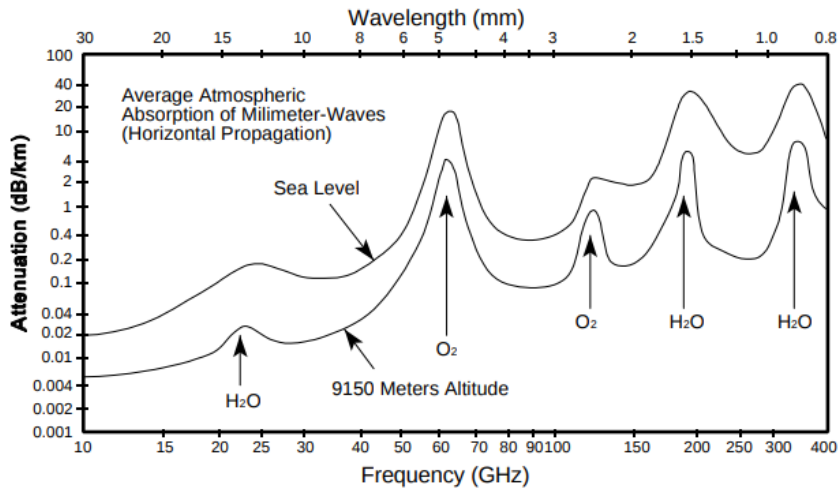


Figure 3.7: Atmospheric Absorption [123]

Weather affects propagation significantly as well. Figure 3.8 shows atmospheric attenuation as a result of rain. The effects of precipitation increase due to scattering and dielectric loss effects of dense areas of water drops. The wavelengths in this band

are typically larger than the precipitation and thus a strong frequency dependency occurs.

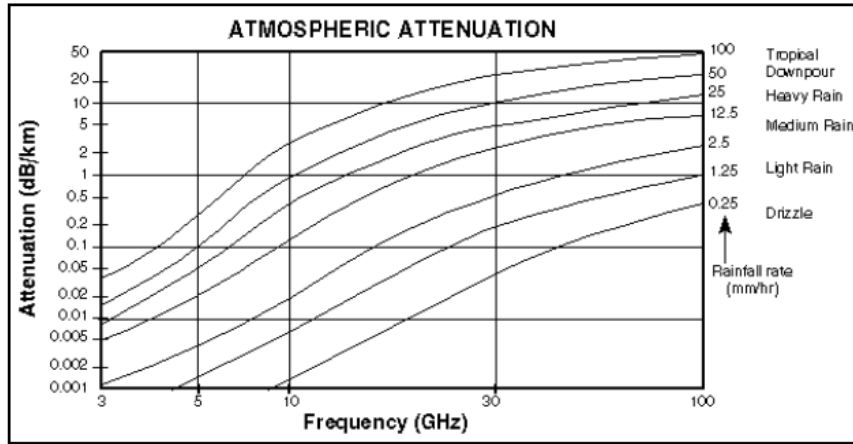


Figure 3.8: Atmospheric Attenuation [123]

Doppler Effect

The Doppler effect is an important topic to consider when choosing a transmit frequency. As described in Section A.1.2 and shown in Figure A.5, the Doppler frequency shift caused by relative velocity is directly related to transmission frequency. X-Band radar shifts about 1 kHz per 20 m/s . S-Band radar shifts about 1 kHz per 50 m/s . Given a Doppler processor's acquisition time and rate, the transmit frequency will affect the resolution and maximum velocity, respectively.

UAV Target Requirements

The first requirement of the transmit frequency is significant RCS of typically commercial drones. If we assume the maximum length of a typical drone is 1 meter, the transmit frequency needs to be significantly higher than 300 MHz in

order to reflect optically. The transmit frequency is ideally well within the optical region and should also meaningfully reflect geometries related to different internal velocities to create distinguished radar echos. The internal velocities can be created by structures like rotor blades, which depending on angle of attack, could have significantly less cross sectional area. For this reason, typically higher transmit frequencies are recommended for identification using small target features. Due to the complexity and variety of commercially available drones, analytic and simulated RCS of drones are unreliable [127]. There have been multiple experimental studies investigating the RCS of commercially available UAVs. The results can be found in Table 3.1. For reference, a person’s RCS is about 0 dBsm or decibels related to square meters. From the studies cited, the RCS of commercial UAVs ranges from -1 to -25 dBsm; however, significant variation occurs along frequency and angle of attack. The studies are provided to give reasonable expectation of RCS of commercial variety.

UAV	Type	RCS [dBsm]	Freq [MHz]	Angle
DJI F450 [89]	Quad	-17	6000-8000	Front and Back
DJI S1000 [89]	Octo	-8	6000-8000	Front and Back
DJI Phantom 3 [128]	Quad	-10:-23	1810-1870	Azimuth
Matrice 100 [128]	Quad	-8:-25	1810-1870	Azimuth
DJI Phantom 2 [127]	Quad	-20	10,000	Side Bistatic
IRIS [129]	Quad	-1:-18	1000-4000	Side
Parrot AR 2.0 [130]	Quad	-18	2400	Side

Table 3.1: Survey of RCS of common commercial drones

Additionally, due to inherent hardware limitations of microwave frontends, the operation bandwidth limitations and transmit power are proportional to the transmit frequency and thus, affects the radar performance by limiting the range resolution. As a result, the FCC currently allocates larger bandwidths at higher frequencies [12].

The bandwidth considerations provide benefits at higher frequency while transmit power becomes a more difficult task to accomplish. For these reasons, typically S-Band and below are used for detection radar at long distances when range resolution is less preferred. Tracking and identification radars typically use X-Band or higher when accurate range is preferred over absolute range. Imaging radars use much higher bands such as K, Ka, and W.

For the research and development within this thesis, S and X Band are selected as operating transmit frequencies due to their availability as licensed and unlicensed FCC radiolocation bands as well as their favorable atmospheric, Doppler, and bandwidth capabilities [12, 42].

3.1.3 System Architecture

The system architecture can be broken down into three subsystems as seen in Figure 3.9: the microwave frontend, the signal acquisition/generation, and the processor unit. The required performance of all three subsystems will be chosen in order to meet radar performance and functionality given a target and environmental use case. The design is made with focus on enabling future research opportunities in **DU²SRI** and to be programmed by the popular open-source RF signal processing prototyping environment, GNU Radio [131]. For field measurements, the systems needs to be mobile and able to capture and store large amounts of radar data. Secondary considerations for future integration into UAVs are the SWaP of the entire system.

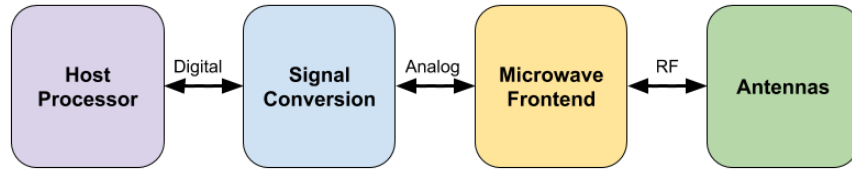


Figure 3.9: Software Defined Radar Functional Architecture

3.1.4 Radar Type

Pulsed radar was heavily developed during WWII by the Allies to help the British detect and track Nazi aircraft and sea vessels attempting to cross the English Channel [132]. The first systems used short-time, high-power, single wavelength pulses of EM waves. When and if the pulse scattered back, a detection and distance estimate could be made by the radar operator. The whole system spun on a large mechanical servo to “sweep” a field of view. This rudimentary system sufficed to win a war but lacked significant range resolution and required high peak power electronics to travel significant distances. A fundamental relationship between the range resolution and peak power limited the systems significantly. Since the war, many technical advances have been theorized and eventually implemented when technology permitted. These include Doppler or CW radar, FMCW, imaging, phased arrays, Moving Target Indicator (MTI), multiple-target tracking, Clutter Rejection and MIMO radar to name a few. One of the most notable advances was developing FM techniques which allowed radar engineers to “pulse compress” more bandwidth into longer pulse to lower peak power.

FMCW radar is arguably the most common tracking and surveillance radar technique at the time of this thesis. It involves modulating the transmit signal’s frequency f_{tx} with a radar waveform. The waveform is commonly a linear sweeping

saw signal. This signal is commonly called a “chirp” due to the sound it makes if applied to an audio synthesizer. The chirp signal can linearly increase or decrease f_{tx} for some bandwidth β_{rsp} (usually no more 500 MHz). The received signal is delayed by the time it takes for the EM signal to propagate twice the distance to the target (reflection), and that time can be estimated by the frequency difference between the Tx/Rx given the slope of the FM signal. The concept was developed because of hardware power constraints with simple pulsed radar and the lack of range estimation in CW “Doppler” radar. The general technique of modulating f_{tx} is called “Pulse Compression” and ultimately compresses the peak power across a bandwidth and decouples SNR from range resolution ΔR . The modulation bandwidth now ultimately determines the range resolution. FMCW can provide higher power per “pulse”, which yields higher SNR at greater distances or smaller RCS, independent of range resolution. A FMCW radar combines the benefits of pulse compression and CW techniques in order to accurately track small targets at a relatively close range. It is commonly used for automobile sensors and is therefore the ideal candidate for UAV SAA tracking function. The decoupling of SNR also provides flexibility to detect targets at longer distances. The maximum range now becomes limited by the radar waveform’s ambiguity which can be extended to the desired detection range and the loss of SNR from the reduced stretch processing window. Achieving the desired radar performance by altering parameters is explored in the following section.

For more information on radar basics and fundamentals of Pulsed, Doppler and Pulse-Compression techniques, see Appendix A.

3.1.5 Radar Performance

The overall radar performance is measured with a variety of metrics and interdependent variables. Typically, the radar range equation 2.13 considers energy or power transfer through the system in order to calculate maximum range given a required SNR or vice versa. The radar range equation is essential for predicting detection performance. The resolution in each measurement dimension such as range, velocity, and spatial angles are primarily functions of the RSP and waveform choice. The waveform can be either pulsed or CW. The resolution and detection performance are inversely related unless the waveform is pulse-compressed across frequency. Inherent to any sampling or measurement process, the discrete acquisition intervals produce aliasing or ambiguities between the input and measured frequency. The SNR, transmit frequency, and ambiguity all contribute to the total available swath of range or velocity capable of being measured. Ultimately, the radar engineer attempts to meet the design resolution and swath requirements between all measured dimensions.

SNR

Equation 2.13 shows the range potential given system and environmental parameters; transmitted power (P_t), antenna gain (G), wavelength (λ), target RCS (σ), bandwidth (β_n), receiver sensitivity or NF (F_n), required SNR ($\hat{\chi}$), system gain (G_s) or loss (L_s), and atmospheric loss (L_a). It assumes the system bandwidth β_s is equal to the noise bandwidth β_n and thus SNR gain from pulse-compression or other RSP techniques are excluded. Equation 3.5 includes the Pulse-Compression Ratio (PCR) and RSP Gain (G_{rsp}). The PCR is defined as the Pulse Width (τ) times

the effective bandwidth of the RSP (β_{rsp}). The system bandwidth is required to be greater than or equal to the RSP bandwidth which cancels out the noise bandwidth thus leaving only τ . As τ approaches Pulse Repetition Interval (PRI), the radar becomes CW and alternate types of RSP are required or preferred.

$$R = \left[\frac{P_t G^2 \lambda^2 \sigma \tau}{k T_0 F_n \hat{\chi} (4\pi)^3} \cdot \frac{G_s G_{rsp}}{L_{fmcw} L_s L_a} \right]^{\frac{1}{4}} \quad (3.5)$$

For FMCW using stretched processing, an additional SNR loss term from non-matched filter processing will further reduce SNR [133]. The loss term is due to the lagged return signal overlapping the transmit signal over a smaller portion of τ , thus reducing the SNR by the FMCW loss factor $L_{fmcw} = \frac{\tau}{\tau_r}$. The overlapping time of return signal $\tau_r(R)$ is a function of the target range as shown in equation 3.6, where τ_d is the time-delay due to the target range. If $\tau \gg \tau_d$, the FMCW loss factor is negligible.

$$L_{fmcw}(R) = \frac{\tau}{\tau_r} = \frac{\tau}{\tau - \tau_d} = \frac{\tau}{\tau - \frac{2R}{c}} \quad (3.6)$$

Resolution

Resolution of a measurement is fundamentally the smallest time interval a system can discriminate or differentiate. Both analog and digital components limit performance. Each analog component is limited in its ability to allow high time-differentials to pass through. The digital approximation can only approach the total analog resolution of the system. From this time-frequency relationship, most measurement systems ultimately reduce to the ability of a system to isolate and separate different spectral contributions. For an FMCW radar, the return signal

contains range information as a function of frequency. Fundamentally, a radar’s range and velocity resolutions are dependent on the system’s ability to separate peaks within the signal’s spectrum. A target at a single range will produce a single frequency tone. The finite and non-ideal measurement inherently generates a bandwidth of uncertainty around the single peak in a noisy spectrum.

The use of the term “bandwidth” usually refers to the effective frequency band containing most of the signal’s energy. Bandwidth can be defined differently based on application, author, or function. The Rayleigh Bandwidth is typically defined as the inverse of the time-duration of a signal. For an ideal pulse of finite length τ , the spectrum will be a sinc function with zeros at $\pm 1/2\tau$. The Rayleigh Bandwidth $1/\tau$ is the width of the main lobe contained between the first zeros on each side. Another definition defines the bandwidth between points 3 *dB* lower than the maximum called “3dB-bandwidth” or “main-lobe width”. The 3dB bandwidth is often used on empirical data where zeros are buried in the noise floor. The Rayleigh bandwidth is often used within theoretical analysis of systems design.

For a pulsed radar system after matched filtering, as seen in Section A.2.1, the Rayleigh bandwidth $1/\tau$ is considered the minimum effective bandwidth. Pulse Compression increases the effective bandwidth from Rayleigh by the Time-Bandwidth Product (TBP) resulting in the RSP bandwidth β_{rsp} . Finally, the range resolution ΔR factors out the speed of light from the bandwidth as seen in equation 3.7. For a range resolution of 1 *m*, the RSP bandwidth must be at least 150 *MHz*. For an FMCW radar system, ΔR acts as a maximum range resolution. Due to the loss of overlapping transmit and receive signals, the range resolution suffers a loss by a

factor of $L_{f_{mcw}}$ as seen in equation 3.6. If τ is sufficiently large compared to τ_d , the range resolution will remain largely unchanged.

$$\Delta R = \frac{c}{2\beta_{rsp}} \quad (3.7)$$

The velocity resolution ΔV is dependent on the Doppler processing window T_D and Rayleigh resolution of the radar Doppler shift $\Delta f_{Dr} = 1/T_D$ as seen in equation 3.8. For pulse-Doppler processing, Doppler measurements are discretely sampled every PRI, therefore the velocity resolution is further limited discretely in the FFT domain. Zero-padding the end of each Doppler FFT call solves this issue. The T_D can be limited by the maximum implementable FFT or filter order. It can also be limited by the required TFR characteristics. For example, if the localized change in velocity or acceleration is needed for a tracking algorithm, the FFT must reduce in size according to the *Uncertainty Principle of Signal Processing*. If velocity accuracy is not important, such as within MTIs, T_D may be as small as two samples. This provides an indication of movement without over processing the data. Given the processing limitations, TFR requirements, and velocity accuracy needs, there exists a maximum or optimal T_D allowed for each velocity estimation. For 1 m/s resolution, S-Band and X-Band radars require 46.2 ms and 14.3 ms processing windows, respectively.

$$\Delta V = \frac{\lambda}{2T_D} = \Delta f_{Dr} \cdot \frac{\lambda}{2} \quad (3.8)$$

Ambiguity

The ambiguity of range and velocity measurements are fundamentally determined by which RSP algorithm is used. The ambiguity function plots the magnitude of the matched filter over effectively range and velocity as seen in section A.2.2. Using typical pulse-Compression and Coherent Processing Integration (CPI) pulse-Doppler techniques, the processing fundamentally becomes one of sequential multi-scale FFTs. Ambiguities can occur in any discrete Fourier Transform process unless proper filtering eliminates aliasing due to the energy occurrence at frequencies above the Nyquist frequency¹. As seen in equations A.12 and A.13 in Section A.1.3, the range and velocity ambiguities are linked via the Pulse Repetition Frequency (PRF) of the radar waveform. Table 3.2 shows the range and velocity ambiguity for the target transmit frequencies. As the PRF approaches 1 MHz , the unambiguous range R_{um} decreases to a nominal Part 107 UAV tracking distance of 150 m . The unambiguous velocity v_{um} approaches maximum Part 107 allowable flight at less than 10 kHz for both S-Band and X-Band. However, S-Band allows for larger maximum velocity per PRF. In other words, the X-Band induces a larger Doppler frequency shift per unit velocity. The maximum PRF is also limited by hardware signal processing computational resources. From Table 3.2 it is concluded a PRF exceeding 1 kHz but less than 1 MHz is required.

Range and Velocity Swaths

The range and velocity swaths of radar sensors are the total available ranges and velocities capable of being measured. The swath requirement for FAA Part

¹Nyquist Frequency $f_n = f_{sample}/2$

PRF [kHz]	0.1	1	10	100	1000
R_{um} [km]	1500	150	15	1.5	.15
X-Band v_{um} [m/s]	1.42	14.2	142	1420	1,420
S-Band v_{um} [m/s]	4.6	46	461	4,610	46,100

Table 3.2: Range and Velocity Ambiguity Settings

107 UAVs for DTI are shown in Table 3.3. Each function requires different range and velocity swaths. The goal of detection radars is to detect the intruding UAV prior to the CAT. Increasing R_{max} lowers probability of error but increases available collision avoidance processing time. A detection or surveillance radar prioritizes lower probability of error at a given distance over resolutions ΔR and ΔV . Thus, the radar range equation 3.5 and SNR are more important parameters over the radar waveform and its ambiguities. Using a low ΔV MTI reduces the need for large velocity swaths by thresholding velocities above standstill. MTI has the added benefit of decreasing detection processing latency. The goal of tracking radars is to estimate range and velocity as accurately as possible. Tracking focuses on closer ranges to avoid measurement errors but requires the entire Part 107 velocity swath. The identification of targets must occur closer than initial detection and within the μD velocity bandwidth [91].

Function	R_{min}	R_{max}	$ V_{min} $	$ V_{max} $
Detection	100 m	> 600 m	> 0 m/s	< 90 m/s
Tracking	0 m	100 m	0 m/s	90 m/s
Identification	0 m	< 600 m	$V_{target} - 10$ m/s	$V_{target} + 10$ m/s

Table 3.3: Range and Velocity Swath Requirements

The maximum range and velocity swaths need to satisfy both waveform ambiguity and radar range equation 3.5. According to equations A.12 and A.13, the PRF is the fundamental parameter for ambiguity. The PRF must be less than 250 kHz to

avoid range ambiguities up to 600 m and 1.5 MHz for 100 m . For S-Band detection, the PRF must be greater than 2 kHz for the entire ± 90 m/s velocity swath. For X-Band tracking, the entire velocity swath requires 6.3 kHz . In FMCW radar with stretch-processing when pulses are no longer coherently integratable, the velocity must be calculated directly from the samples, and the PRF no longer determines the velocity swath.

Using the radar range equation, the theoretical SNR for S-Band and X-Band at 600 m and 100 m vs. PRF is plotted in Figure 3.10. The plot assumes nominal values; $\sigma = 0$ dB , $G_a = 15$ dB , $P_t = 0$ dBm , $F_n = 3$ dB , and $G_{rsp} = 3$ dB . The point labels are the minimum PRF given the required Part 107 unambiguous velocity. The maximum PRF is dependent on unambiguous range and extends off the graph to the right. For the red X-Band tracking, the target returns as close as 100 m , and the SNR is large across most PRF. However, tracking SNR reduces to well below 0 dB at 600 m . For the green S-Band Detection at 600 m , the PRF must be less than 8.2 kHz for above unity SNR. SNR can be increased to 10 dB if the minimum restriction on PRF is loosened to $v_{um} = 45$ m/s as seen on the extrapolated tail. The shaded green region shows the S-Band detection radar performance solution that satisfies the swath from an SNR and ambiguity perspective. Using FMCW where $\tau = PRI \approx 8$ kHz , the FMCW loss factor $L_{fmcw} = 0.14$ dB .

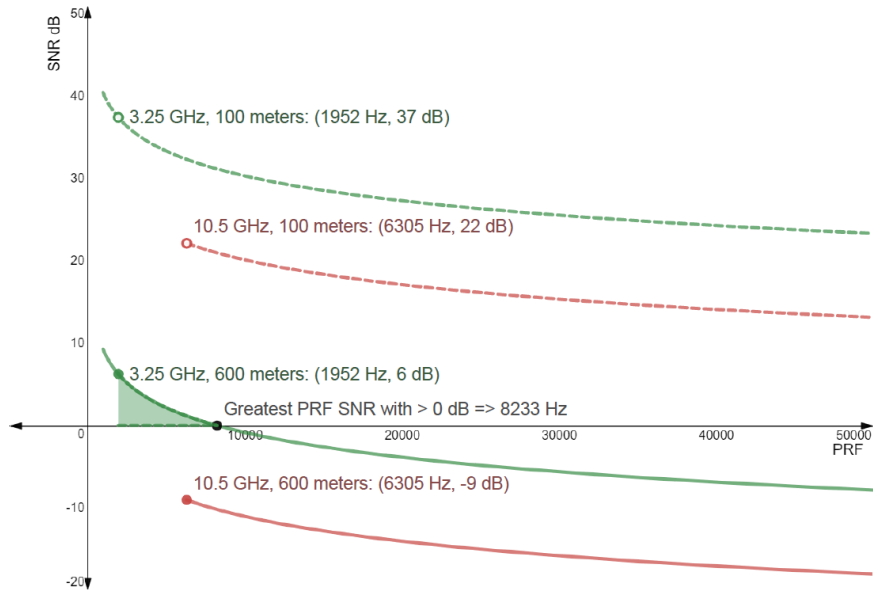


Figure 3.10: Stretched Radar SNR vs. PRF

3.2 Testbed Design

Table 3.4 consolidates radar performance requirements for the desired target, environmental limitations, and desired functionality. The right hand column gives a brief description of the rationale behind deciding the target value. The rationale originates from FAA regulations [2], CAS requirements [9], physical size constraints, empirical data [91], or nominal or conservative values if no clear value exists or is relative to the function. Of note, the beyond worst case maximum 600 *m* CAT is derived in [9] and is used as a detection maximum range target value. For tracking, a nominal 100 *m* is used. For resolution, nominal values $\Delta R = 1m$ and $\Delta V = 1 m/s$ are used. In the case of ΔR , the nominal value is roughly the largest maximum dimension of a typical UAV.

Goal	Target Value	Units	Reasoning
Detection			
Range Swath	(100, 600)	m	CAT Requirement
Range Resolution	> 10	m	Low Priority
Velocity Swath	± 90	m/s	Part 107 UAV regulation
Velocity Resolution	> 10	m/s	Low Priority
Tracking			
Range Swath	(0, 100)	m	CAS Requirement
Range Resolution	< 1	m	Target physical size
Velocity Swath	± 90	m/s	Part 107 UAV regulation
Velocity Resolution	< 1	m/s	Tracking Algorithm Error
Identification			
Range Swath	(0, 600)	m	Limited by Detection
Range Resolution	1	m	Target physical size
Velocity Swath	± 10	m/s	UAV μ D bandwidth
Velocity Resolution	< 1	m/s	Desired Doppler TFR

Table 3.4: Radar Detection, Tracking and Identification Performance Design Goals

From the performance design goals, Table 3.5 shows the range of system parameters of an S-Band detection, X-Band tracking, dual-band identification FM range-velocity radar. For FMCW radar where $\tau = PRI$, in order to keep $L_{fmcw} < 1$ dB at 600 m the PRF must remain below ≈ 50 kHz.

Parameter	Target Value	Units	Reasoning
S-Band Detection			
f_{tx}	2 – 4	GHz	Easy Propagation
Bandwidth	> 15	MHz	10 m Resolution
PRF	(2, 8)	kHz	Ambiguity + SNR + L_{fmcw}
T_D	(4.62/46.2)	ms	(10/1) m/s Velocity Resolution
X-Band Tracking			
f_{tx}	8 – 12	GHz	Large BW and Doppler
Bandwidth	> 150	MHz	1 m Resolution
PRF	(6.3, 50)	kHz	Ambiguity + L_{fmcw}
T_D	14.3	ms	1 m/s Velocity Resolution
Identification			
f_{tx}	S-Band,X-Band		Comparison
Bandwidth	30 – 1000	MHz	Low Priority
PRF	(2, 50)	kHz	Ambiguity + SNR
T_D	> 14.3	ms	< 1 m/s Velocity Resolution

Table 3.5: Radar System Parameters to meet Performance Goals

3.2.1 Systems Overview

The final system design consists of two SDR based SAA radar testbeds at S-Band and X-Band. The host processor is a Razer Blade Stealth Laptop with a GeForce GTX 1060 external graphics card. A commercially available SDR is used for signal conversion between digital and RF signals. A microwave frontend including amplifier, filters, mixers, etc... conditions the signal to propagate from a directional antenna aperture. Each microwave frontend was developed using MMIC and custom parts. The design, simulation, implementation, and evaluation run through many iterations in order to achieve required performance. The RF and microwave development was performed primarily with Keysight’s Electronic Design Automation (EDA) software including EMPro [134], Advanced Design Systems (ADS) [135], and Genesys RF/Microwave Synthesis and Simulation Software [136].

The S-Band is covered using commercially SDR devices which are available with maximum tune frequencies ranging from 3.8 to 6 GHz . To achieve operation at X-Band, centering 10.5 GHz , an additional secondary frequency converter is required. The converter also allows a chirped Local Oscillator (LO) to potentially stretch-process to wider β_{rsp} . Additional channel filtering, PAs, and Low Noise Amplifiers (LNAs) are implemented with MiniCircuit’s MMICs [137] to condition the signal and remove distortion or spurious mixing signals. The microwave frontend components and system are verified using a 26.5 GHz Keysight N9040B UXA Signal Analyzer. The bill of materials is found in Appendix D.

3.2.2 Software Defined Radio

The system uses SDR technology combined with a prototype microwave frontend to provide flexibility when interacting with signals up the X-Band. There are many SDR boards currently available on the market as seen in Figure 2.15. More fundamentally, the transceiver MMICs choice ultimately determines performance characteristics. At the time of this research, three chipsets dominated the SDR transceiver market [56]. The lower performance, RTL-SDR family of SDRs is a well established, low-cost (\$25) single channel SDR solution operating up to 2.2 GHz with 3.2 MHz bandwidth [138]. The performance is significantly lacking for this system’s performance needs. Analog Devices AD93XX suite of transceivers are incorporated into many full SDRs such as Ettus Research’s USRPs [139, 140]. This family provides the best performance among commercially available SDRs operating up to 6 GHz with 20–100 MHz bandwidths. Ettus Research designs SDRs for use primarily with research labs. The third family is based on Lime Microsystems’ SoP transceivers,

LMS7002 series [141]. The chip operates up to 3.8 *GHz* with potential 60 *MHz* digital bandwidth. It provides full 2x2 duplex MIMO operation and is supported by a suite of open-source drivers. In 2016, Lime Microsystems crowdsourced development of a fully HW/SW open-source SDR board [56, 142]. The low cost (\$300), claimed performance, established transceiver chip, open-source and large support community lead to the decision to use the LimeSDR board for the radar testbed.

LMS7002

The LMS7002 is a second-generation Field Programmable RF (FPRF) transceiver IC [141]. The FPRF includes two fully duplex, homodyne I/Q coherent channels, two PLL-tunable low phase noise synthesizers, 8051 micro-controller with SPI control registers, on-chip DSP units, and custom high-speed interface as seen in Figure 3.11. The DSP, micro-controller, and hardware are all capable of accounting for in-chip non-linearities and self-calibration.

Each filter, amplifier, synthesizer, mixer, and data converter are all programmable for as much flexibility as allowed. The chip also contains three parallel LNAs for low, wide and high operating frequency. The matching of each LNA and supporting transmission lines are optimized for maximum noise performance within each range. It operates with the specification seen in Table 3.6.

LimeSDR

The LimeSDR board contains one LMS7002 FPRF chip, an Altera Cyclone IV EP4CE40F23C8N FPGA, a Cypress FX3 USB 3.0 controller, required memory, power distribution, clock management and external connectors as seen in Figure 3.12

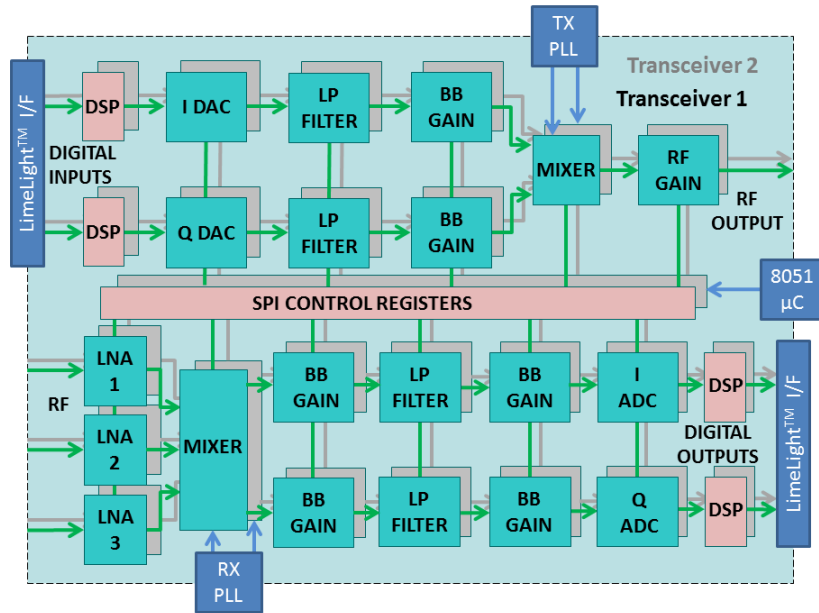


Figure 3.11: LMS7002 Functional Block Diagram [141]

Parameter	Min.	Typ.	Max.	Unit	Conditions
f_{tx}	30		3800	MHz	PLL Tunable
	0.1		3800	MHz	TSP NCOs
β_{dig}			48	MHz	MIMO
			96	MHz	SISO
β_{rf}			160	MHz	Analog
P_t			0	dBm	CW
NF		2.0		dB	at 0.95 GHz
		2.5		dB	at 2.0 GHz
		3.5		dB	at 3.8 GHz
G_r	0		70	dB	1dB steps
G_t	0		89	dB	1dB steps
Bit Depth		12		bits	
ADC f_s			160	MHz	Samples per second
DAC f_s			640	MHz	Samples per second
Total Power Usage		880		mW	2x2 MIMO
		550		mW	SISO

Table 3.6: Lime Microsystem's LMS7002 Specifications

and 3.13. The board layout, hardware selection and manufacturing processes are completely open-source which allows for easy diagnostics or custom development when necessary.

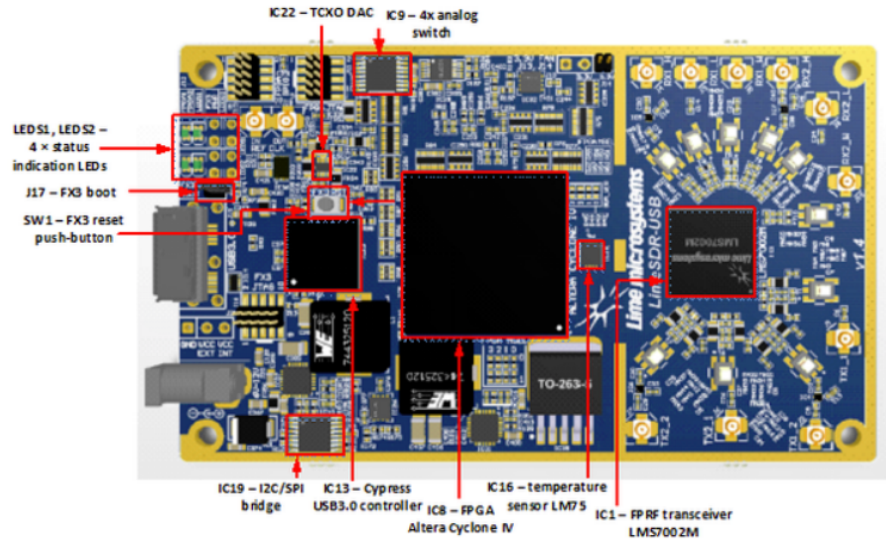


Figure 3.12: LimeSDR Board Layout [142]

A total of ten coaxial RF U.FL connectors are provided. Each transmit channel has two separately matched outputs for high and low tune frequency. Each receive channel has three inputs for low, wide, and high tune frequency. The LMS7002 coherently transmits/receives RF signals, converts to/from digital signals, and receives/sends data across a high-speed LimeLight interface to the FPGA. The FPGA contains an open-source Altera Quartus 15 project with HDL code to handle board settings, transceiver settings, data interfacing, stream settings, timing, and packetization. The FPGA is programmable through a GPIO JTAG interface or through a USB connection. The Cypress FX3 USB 3.0 controller interacts with the host processor with packets of settings or stream data.

The LimeSDR has similar RF specifications to the LMS7002 chip itself; however, the instantaneous or digital bandwidth is further limited by the theoretical maximum USB 3.0 bitrate (5 Gbits/s), theoretical maximum interface data rate between FPGA and FX3 (400 MB/s), and required overhead. At 12 bits/sample , the fundamentally β_{dig} limitation is specified as 61.44 MHz per each SISO channel. To clarify, that is two 30.72 MHz transmit and 30.72 MHz receive streams simultaneously. Thus the maximum stream data rate is 368.64 MB/s . This satisfies the detection bandwidth requirement but does not satisfy the tracking.

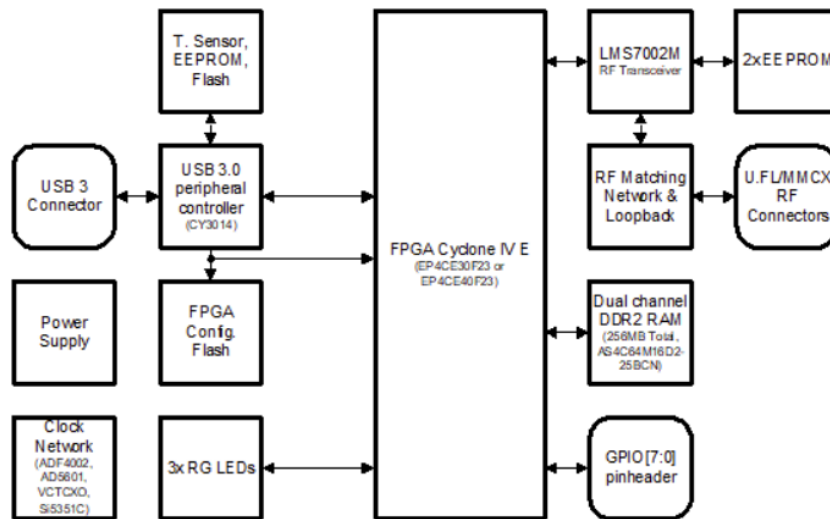


Figure 3.13: LimeSDR Block Diagram [142]

The board also includes multiple temperature sensors and optional fan control output. The LimeSDR is housed in a custom made aluminum housing with a temperature controlling fan, heat syncs, and EM isolation copper netting to keep receiver sensitivity as low as possible. The housing is shown in Figure 3.14.



Figure 3.14: LimeSDR Housing from left to right: open, frontside, backside

LimeSDR Application Ecosystem

The stack of supporting software applications for LimeSDR or general SDR programming is large and lacks significant documentation. At the lowest abstraction level, hardware drivers control low-level component settings and abstract commands to a human readable format. LimeSuite provides C/C++ API for LMS7002 and LimeSDR function calls [143]. It also provides a GUI for register and above level debugging and self-calibration. Finally, it provides stream and control API to the larger SDR ecosystem via a hardware agnostic driver abstraction C++ layer called SoapySDR [144]. There exist many user-level applications with sophisticated GUI and user control; however, GNU Radio (GR) is currently the most supported and flexible signal processing prototyping application [131]. GNU Radio also provides a GUI application called GNURadio Companion for visualizing the signal flow. GR is written in C/C++ and Python and supports third party modules to extend the already extensive tree of source, sink, and signal processing blocks. SoapySDR and GNU Radio connect through a latent application called gr-osmosdr which handles SDR source and sink block effectively. Figure 3.15 shows how the LimeSDR specific applications integrate into the larger SDR application ecosystem. A gr-radar toolbox with RSP block was created in 2014 by the Communications Engineering Laboratory

at Karlsruhe Institute of Technology in Germany [145]. It provides most of the RSP block required for this project.

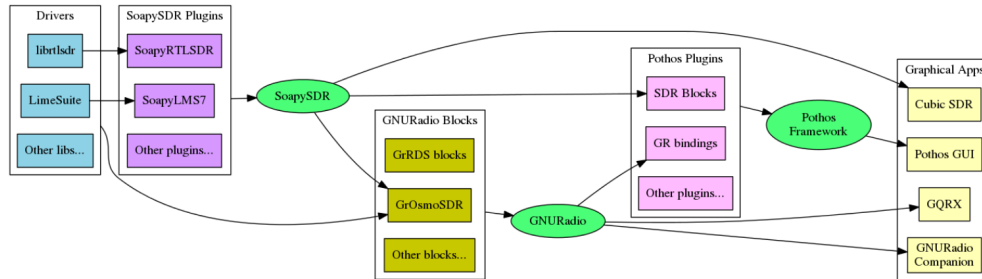


Figure 3.15: LimeSDR Applications Ecosystem [144]

3.2.3 S-Band

Figure 3.16 shows the functional block diagram for a 2x2 digitally steered MIMO, surveillance S-Band radar. The 2x2 MIMO, homodyne, fully coherent SDR operates up to 3.8 GHz with 30 MHz instantaneous or digital bandwidth. The microwave frontend includes a single PA, optional LNA, and four micro-strip or “patch” antennas. The block diagram excludes any channel filtering required when spurs are found. The PA and patch antennas were designed and implemented using a suite of Keysight’s EDA software including a 3D EM solver, non-linear microwave simulation, and board layout tools.

Microwave Frontend

The S-Band microwave frontend transmitter simply filters, amplifies and propagates the SDR outputs. The receiver gathers, filters and amplifies incoming signals for the SDR inputs. The transmit amplifier is a PA specifically designed

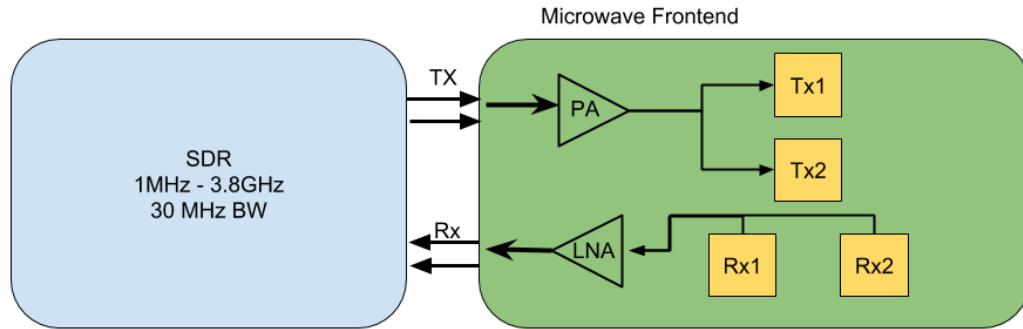


Figure 3.16: S-Band Radar Testbed Block Diagram

to handle high output powers. The receive amplifier is an LNA designed for efficient matching to reduce the NF. The LNA is optional for enhanced SNR performance. Mini-Circuit’s ZX60-V62+ or ZX60-153LN-S+ amplifiers could be used. A custom PA board is designed from sample MMIC chips. Custom patch antennas were designed and implemented completely in house.

S-Band Power Amplifier

A custom SMA connector-matching RF board is designed around a quarter watt 2.3 – 4 GHz Analog Devices Driver Amplifier (ADL5321). The reference matching and biasing circuit from the datasheet is simulated in ADS. Discrete genetic algorithm-based optimization is performed to select ideal circuit components and spacing. Figure 3.17 shows the scatter parameters of the input and output ports of the simulated PA matching board. The circuit components are layed out on a PCB. The PCB is fabricated and implemented and the components are soldered onto the board. Figure 3.18 shows the final implemented PA board. The gain is measured to be about 10 dB from 2.5 – 3.5 GHz which is similar to the simulation. The total cost of the PA is \$9.98.

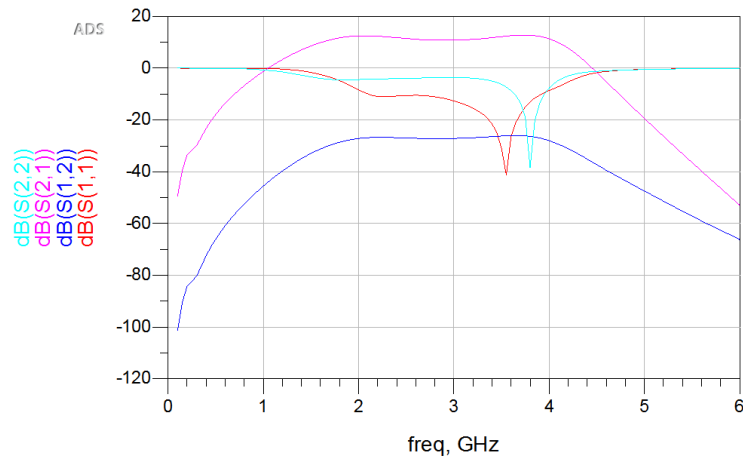


Figure 3.17: S-Band Power Amplifier Simulation Scatter Parameters

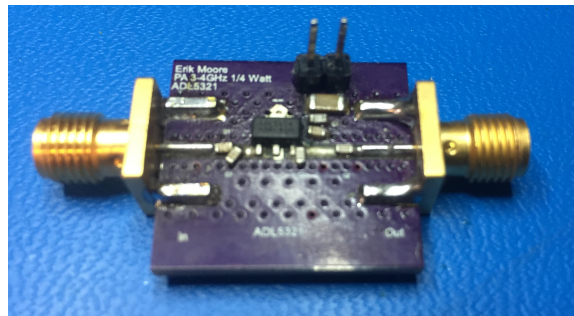


Figure 3.18: S-Band Power Amplifier Implemented

S-Band Patch Antennas

Patch antennas are designed, simulated and manufactured using Keysight's EDA software and standard etching processes. The single rectangular patch's length is calculated to be the half wavelength of the resonance frequency (3.25 GHz). The width loosely determines bandwidth. The radiating element is inset fed matched to a 50Ω micro-strip transmission line and SMA connector. Figure 3.19 shows the geometry of the patch antenna.

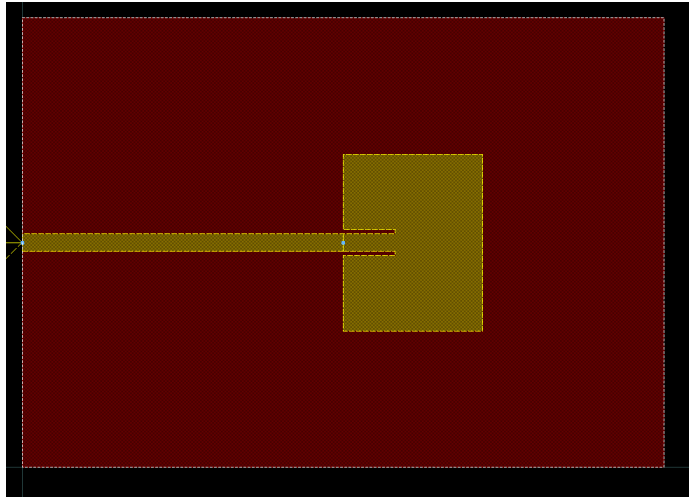


Figure 3.19: S-Band Micro-Strip Patch Antenna Geometry

An FEM method 3D EM solver simulates the near field, far field, radiation pattern and antenna parameters as seen in Figure 3.20. The gain shows peaks at frequencies higher than 3.25 GHz due to alternate resonance modes from E_{01} . The design is implemented using a low-cost, two layer copper clad board. Black spray paint is laser cut and removed from the board where copper is desired to be removed by chemical etching.

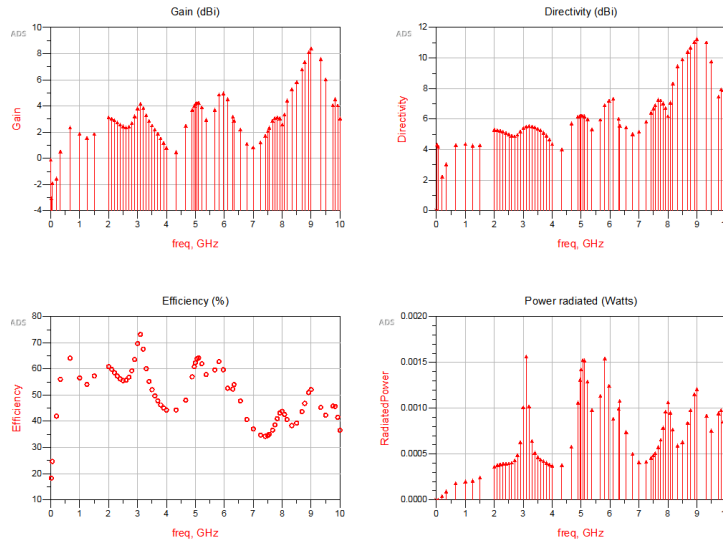


Figure 3.20: S-Band Micro-Strip Patch Antenna Simulation

3.2.4 X-Band

The X-Band tracking and identification radar requires an additional frequency conversion stage seen in Figure 3.21. This design uses a secondary heterodyne conversion stage to convert the SDR output frequency of 3.25 GHz up to 10.5 GHz by way of the upper mixing product with an LO centered around 7.25 GHz . The LO can be tuned along the entire X-Band and frequency modulated to extend the effective bandwidth β_{rsp} by a couple orders of magnitude. This stretch processing is an alternative RSP to matched filtering where the radar waveform is decoupled from the signal within the hardware prior to sampling. The stretched processing has a maximum SNR equal to the SNR of the ideal matched filtered process. It is accomplished by splitting the same chirped LO between transmit and receive paths.

The chirped LO is driven by a radar waveform generated external to SDR, conversion board, and microwave frontend. A synchronization signal is simultaneously

sent to the SDR board to synchronize radar waveform with the samples gathered and sent across USB to host processor. The external function generator is controlled by the host processor, thus fully connecting the control loop. The design is alternatively capable of CW modes and matched filtering using the SDRs instantaneous digital bandwidth.

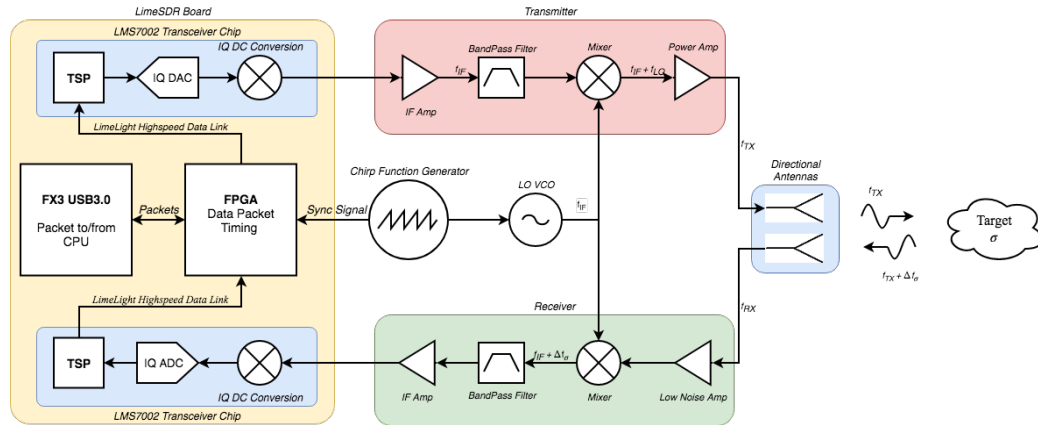


Figure 3.21: X-Band Radar Testbed Block Diagram

Frequency Conversion

In order to convert the SDR RF up to X-Band frequency (10.5 GHz), a heterodyne frequency conversion stage is required (Figure B.2). The choice of intermediate and LO frequencies determines not only the potential RF frequency but all spurious mixing products as the result of harmonics present at the mixer inputs. The spurs reduce in power as the order increases; however, mixing 2^{nd} and 3^{rd} can result in spurious signals close the fundamental output frequency. A Genesys tool call “WhatIF” calculates mixing products from non-linearities to determine spurious free choices.

Figure 3.22 shows the up-conversion spurs at the output for $f_{IF} = 3.25 \text{ GHz}$ and $f_{LO} = 7 \text{ GHz}$. The yellow RF bandwidth is interfered by the $2f_{LO} - f_{IF}$ spur at -60 dBc . Lowering the f_{IF} slightly will increase the spur frequency out of the range. Also, strong $3f_{LO} - 3f_{IF}$ spur nears the operating bandwidth. Careful filtering of the IF and LO must be used to reduce harmonic spurious interference. Also, reducing f_{IF} by about 250 MHz will move all spurs out of the desired bandwidth.

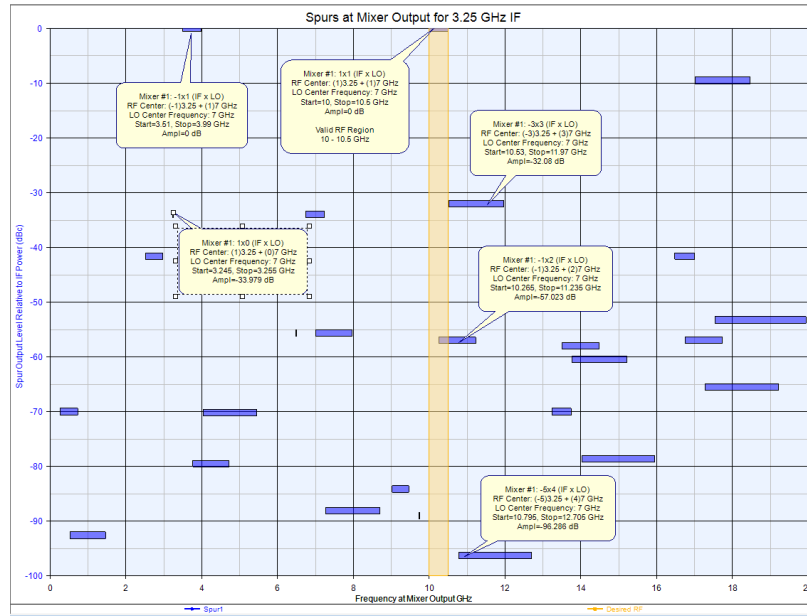


Figure 3.22: X-Band Up-converter Spurious Mixing Signals

For down-conversion, Figure 3.23 shows possible spurious free f_{IF} outputs. Again, a few spurs overlap the desired f_{IF} ; $-2f_{LO} - f_{RF}$ and $-5f_{LO} - 3f_{RF}$. Adequate channel filtering or moving the f_{IF} can reduce spurious interference.

Considering the harmonic's spurious possibilities at $f_{LO} = 7 \text{ GHz}$ and available bandwidth, two Mini-Circuits mixers (Zx05-153-S+) provide the correct frequency conversion at 9 dB of loss. A chirped LO centered around 7 GHz is achieved by tripling a $2 - 3 \text{ GHz}$ Voltage Controlled Oscillator (VCO). The frequency

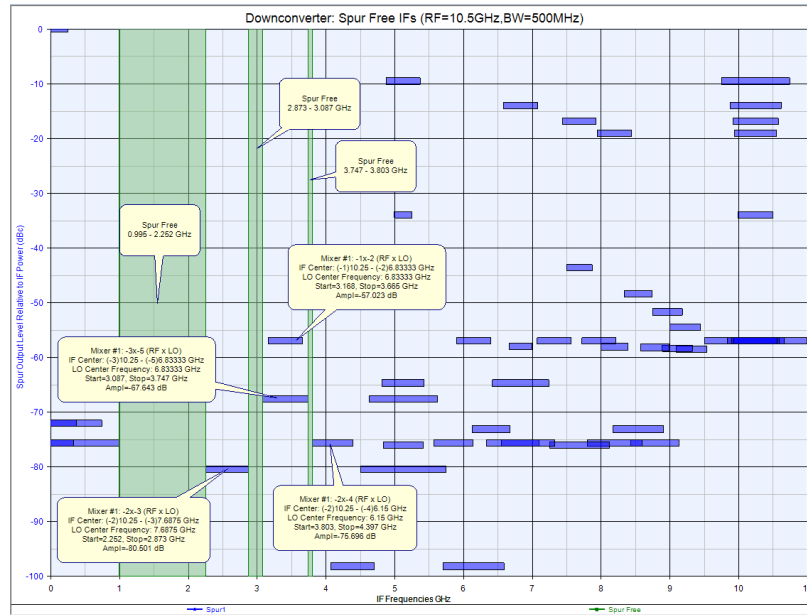


Figure 3.23: X-Band Down-converter Spurious Mixing Signals

conversion block diagram is shown in yellow in Figure 3.24. The appropriate filtering and amplification presents a clean chirped LO split between the two mixers at approximately 7 dBm . The chirped LO output is verified with the Keysight N9040B Spectrum Analyzer. The output power is measured above 7 dB from $7 - 7.5\text{ GHz}$. The 2^{nd} and 3^{rd} harmonics are above 42 dBc with total harmonic distortion of 0.71% at 7.245 GHz .

After mixing with the IF at $f_{IF} = 3.025\text{ GHz}$, the unfiltered transmit 500 MHz bandwidth signal is shown in Figure 3.25. The single-tone IF on the left side of the spectrum mixes with the chirped LO using 500 MHz of the available bandwidth between Markers 3 and 4. The upper and lower mixing products are clearly seen at $f_{LO} \pm f_{IF}$. The LO is isolated through the mixer down to -30 dBm . The desired upper mixing product is seen between Marker 5 (10.058 GHz) and Marker 6 (10.489 GHz). The strongest mixing spur is seen directly to the right of the desired

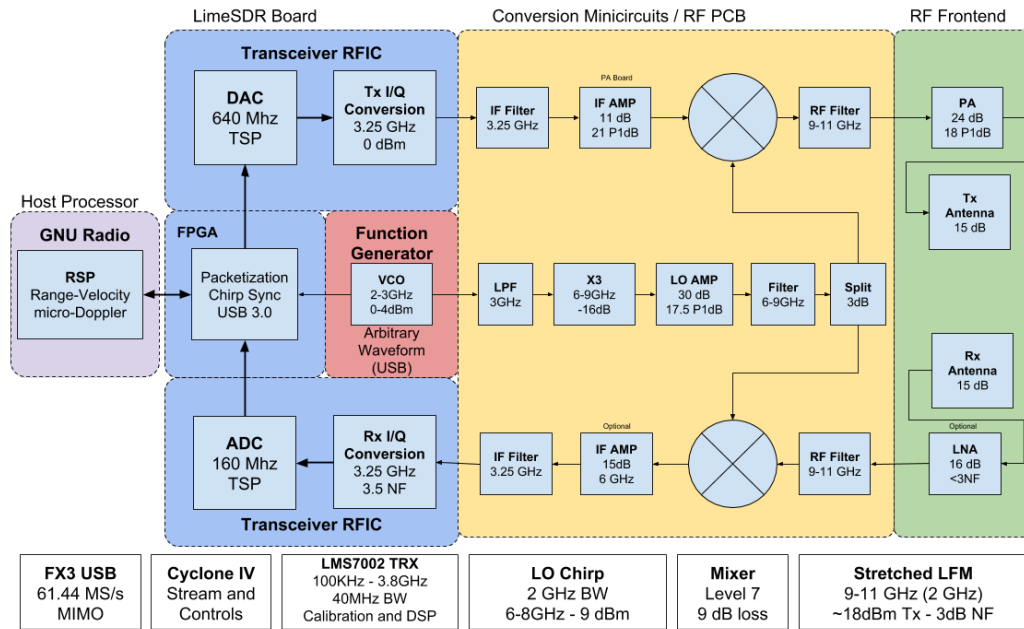


Figure 3.24: X-Band Radar Testbed Block Diagram

signal with ≈ 100 MHz bandwidth. The spur is the 2^{nd} LO harmonic minus the IF. Smaller mixing spurs are seen scattered along the noise floor.

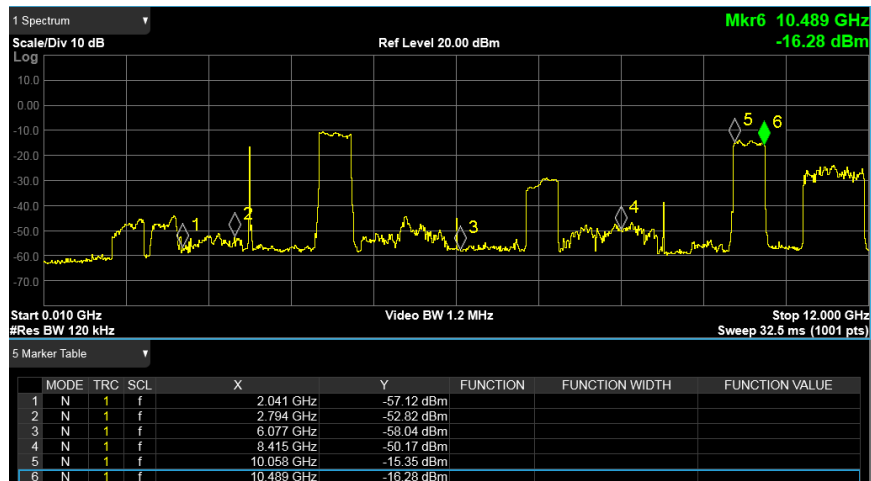


Figure 3.25: N9040B Measurement of Unfiltered Frequency Conversion Spectrum

Microwave Frontend

After the frequency conversion, the transmit and receive signal are properly filtered and amplified before radiating through horn antennas. A high-Q cavity band-pass filter isolates only the desired bandwidth prior to driving the final PA to maximum output power. The maximum P_t is 20 *dBm* which can be controlled via the SDR transmit gain control. The system NF is dominated by the final LNA (3.5 *dB*). Two identical horn antennas operating in the WR-90 standard waveguide frequencies (8.2 – 12.4 *GHz*) provide high directivity required for tracking radars. The antennas have 15 *dB* gain, 29 degrees main beam width, and are linearly polarized.

Waveform Generation

The radar waveform is generated by a headless USB arbitrary waveform generator from SciCore Instruments. The generator can be programmed to create any waveform and is limited with 50 *MHz* bandwidth. It drives the VCO in the chirped LO. The instrument runs off of USB power and provides a “sync” channel which sends a square wave with the same frequency and phase as the output channel. The host processor will make radar measurements and the appropriate API can dynamically send control to SciCore in order to complete the control loop and provide potential for CR research.

Power Distribution

The DC power provided to the frequency conversion and microwave frontend need to be stable and quiet in order to not introduce noise and non-linearities into the signal. To achieve this, special Low Drop Output (LDO) regulators generate

the desired voltages. Texas Instruments TPS7A4701 provides an evaluation board (TPS7A4701EVM-094) with input/output pins and voltage control. Two boards are purchased to drive the 5 and 12 volt power supply lines. The x-band system pulls nominally 3.5 *Watts*.

3.2.5 RF Link Budgets

To simulate overall SNR, RF link budgets are calculated for each band using Keysight's Genesys Software [136]. Simple models use datasheet or measured data of each component. The models are plugged into dynamic simulations for iterative design, budgeting, and validation. The channel model uses simple gain blocks and freespace loss plus atmospheric attenuation for the target's RCS and freespace loss, respectively. The target is nominally $\sigma = 0.1 \text{ m}^2$ large at 100 *m*. Using these link budgets, each component is meticulously selected for optimal system performance and component performance while minimizing the monetary budget of the project. For a select few components and antennas, internal design and implementation was required for customization and cost reduction.

Figures 3.26 and 3.27 are plots of the cascade power (CP), cascade noise power (CNP), desired signals cascade power (DCP), and cascade signal to noise ratio (CNR) across each component for each operation band. The models predict 1 *dB* and 25 *dB* SNR for S-Band and X-Band, respectively. The S-Band differs drastically from theory in Figure 3.10 due to a decreased antenna gain, increased PRF, and smaller target RCS. X-Band SNR is higher due to using a smaller PRF from theory.

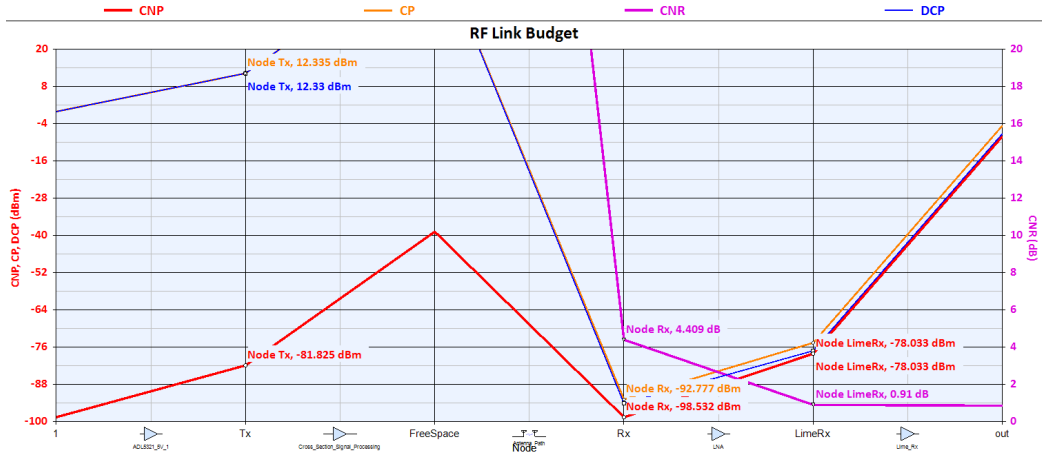


Figure 3.26: S-Band Radar Testbed RF Link Budget



Figure 3.27: X-Band Radar Testbed RF Link Budget

3.3 Prototypes

During the prototyping phase, many problems needed to be addressed in order to successfully make radar measurements. The following section will describe first-run prototypes, the RSP, and any major problems that need to be debugged or redesigned.

3.3.1 S-Band

Figure 3.28 is the prototype S-Band single-channel detection and identification radar testbed. The PA, LNA, and patch antennas are clearly seen connected to the SDR via coaxial SMA connectors. The SDR is connected to the host processor laptop via a short USB cable. DC power wires are removed from the picture to avoid clutter. The output power was measured with the S-Band PA to be 3.12 dBm .

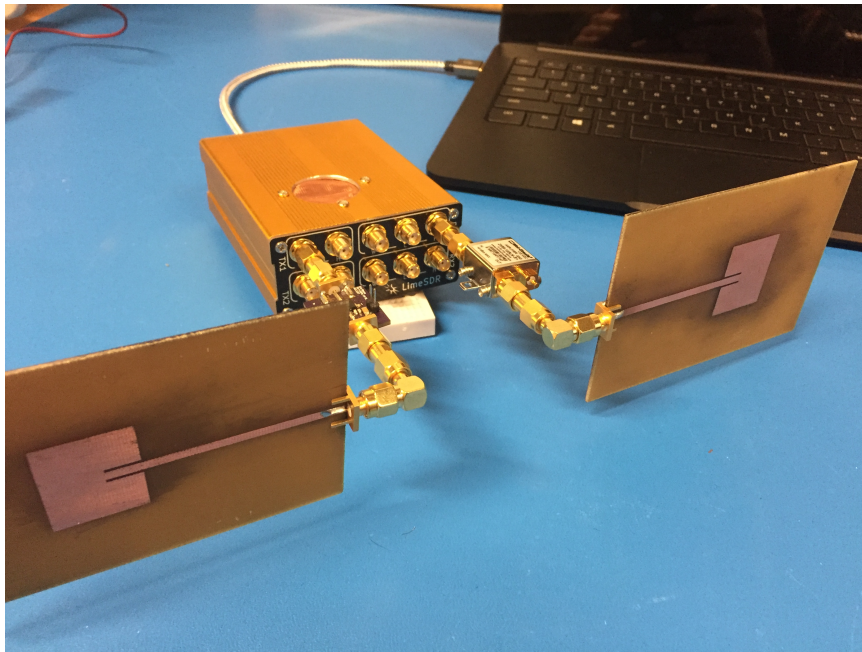


Figure 3.28: S-Band Radar Testbed Prototype

S-Band Radar Signal Processing

The S-Band detection radar only uses the internal 30 MHz instantaneous or digital bandwidth as the effective RSP bandwidth ($\beta_{dig} = \beta_{rsp} = 30 \text{ MHz}$). The signal is generated in GNU Radio, transmitted out of LimeSDR, reflects off of the target, is received by LimeSDR, and processed in GNU Radio. The signal is an LFM

chirp followed by some deadtime CW DC signal. The bandwidth of the chirp extends from $-f_s/2$ to $f_s/2$. A software de-chirping RSP is performed by mixing the beating transmit and receive chirps. The RSP signal path is shown in Figure 3.29. The chirp source is split between the echotimer and delay block. The echotimer block handles synchronizing transmit and receive packets. Both the echotimer and delay block handle HW/SW latency occurring along the data streaming path. A beat frequency is created after the Multiply Conjugate block directly related the range of a target. The signal is filtered, decimated, and peak searched using a simple FFT.

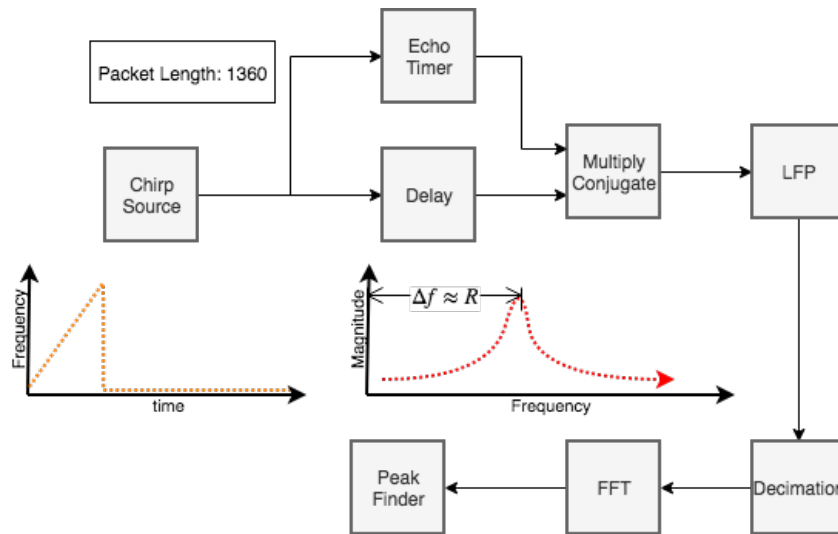


Figure 3.29: S-Band RSP

Latency

The hardware latency/jitter from FPGA packetization and software latency/jitter from GNU Radio scheduler inhibit clean synchronization and clean radar measurements. To solve this problem, a single “Echotimer” block is created to handle LimeSDR specific source/sink synchronization. The block is found within an updated

version of gr-radar and interacts with GNU Radio, SoapySDR, and LimeSuite. The echotimer block successfully synchronizes channels and eliminates most of the jitter. Due to overhead and databus limitations, some “deadtime” between chirps is required to reduce packet loss to a tolerable level.

Figure 3.30 shows the display GUI for GNU Radio Companion. The transmit and receive chirp packets in the time domain are seen on the top plot. The smaller green and black signals are the real and imaginary return signals from placing the patch antennas directly facing each other. However, the leakage from the transmit to the receive channel is strong enough to be observed regardless of position of antennas. This self-interference restricts observable range however, provides a signal to calibrate internal latency. The bottom plots are the frequency domain beat signal arising from the self-interference testing. The internal latency is seen as a shift in frequency from DC. Dynamic control parameters in the GUI allow for real-time tuning by centering the self-interference peak. Packets can be synchronized with sample rate precision.



Figure 3.30: S-Band Self-Interference Tune Testing

3.3.2 X-Band

Figure 3.31 shows the prototyped X-band single channel tracking and identification radar testbed. The LimeSDR, SciCore FuncGen, power regulators, and microwave frontend are all mounted on aluminum sheet metal. The entire system is placed on a cart to bring to field locations. The system can be powered by wall outlet if one can be reached with an extension cord. Otherwise, the system can be run off of any standard lithium battery that provides above 12 Volts. The maximum output power is measured to be is 12 *dB* and the spurious free bandwidth around 10.5 *GHz* is 260 *MHz*.

X-Band Stretch Processing

Figure 3.32 displays the X-Band system from a signal processing perspective. The chirp signal in orange is a 50% duty cycle voltage signal generated by the function

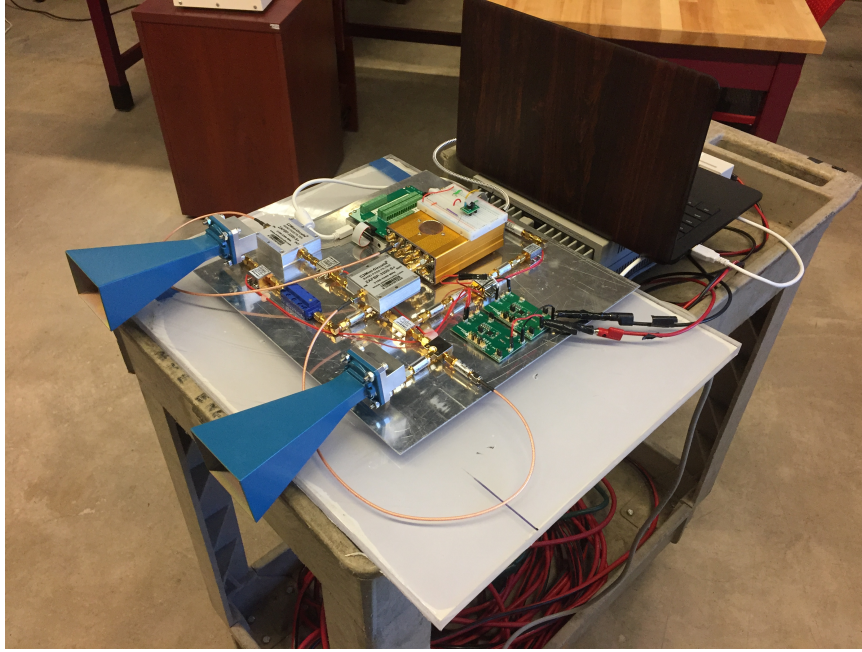


Figure 3.31: X-Band Radar Testbed Prototype

generator to drive the VCO. The purple LO signal is a 50% duty cycle LFM chirp which drives the mixers. The receive signal in green is time $\Delta\tau$ and frequency f_{Dr} shifted from the transmit red signal due to range and velocity of the target. The chirp is decoupled out of the receive signal leaving the IF offset by both Δf and Δf_{σ} . The SDR samples and estimates the peak frequency. The range is calculated from the linear slope $m = \frac{\Delta f}{\Delta\tau}$ and estimated peak $\Delta\hat{f}$ factoring out c shown in equation 3.9.

$$\hat{R} = \Delta\hat{f} \frac{c}{2m} \quad (3.9)$$

The Doppler frequency shift f_{Dr} for X-Band will be less than $\approx 6 \text{ kHz}$ from Figure A.5. During the chirp portion of the waveform, the Doppler shift is much smaller than the range frequency shift. During the non-chirp portion of the waveform, the peak finder will estimate the velocity shown in equation 3.10. Additionally, a

down-sloped chirp will experience a Doppler shift affecting the absolute frequency shift in the opposite direction. The difference in the magnitude of each direction of the chirp is twice the Doppler shift.

$$\hat{V} = \Delta \hat{f} \frac{\lambda}{2} \quad (3.10)$$

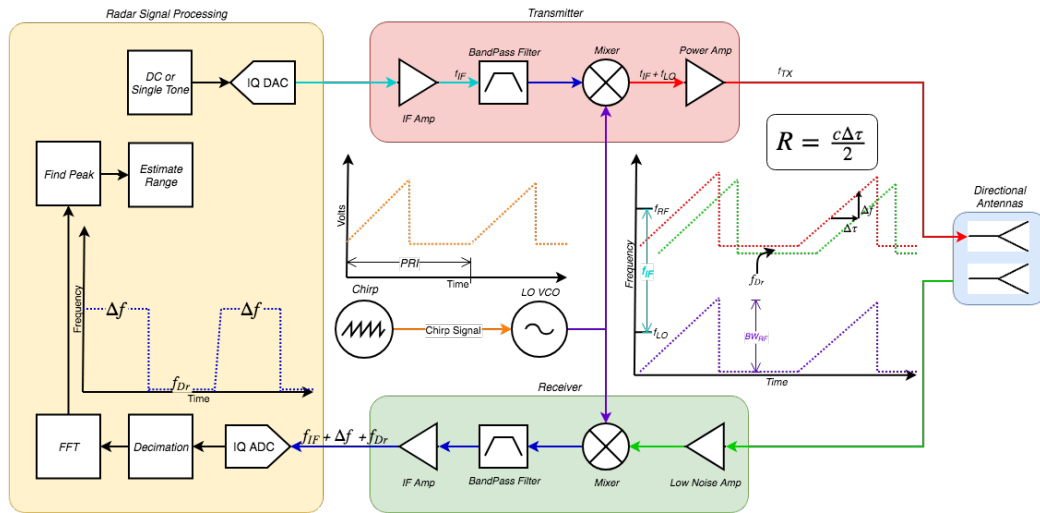


Figure 3.32: X-Band Stretch Processing Frequency Conversion

Chirp Packet Synchronization

Having an external function generator driving the radar waveform requires the time to be synchronized between said function generator and the samples gathered by LimeSDR. To accomplish this, the SciCore Function Generator provides a “sync” output which is a square wave with the same phase as the waveform. The sync output is connected to a GPIO pin of the FPGA. The FPGA now sends a chirp timestamp and the period of the chirp as information in the footer of each packet as seen in Figure 3.33. The new data packet structure is implemented by modifying

the provided open-source Altera Quartus 15 HDL project. A counter and finite state machine is used to calculate the period to the nearest clock tick. The start of each chirp period is recorded using the same timestamp clock as the receive channel. Both chirp period and the last chirp timestamp are sent as two 32b footer integers with units of sample clock ticks. A modified version of the LimeSuite drivers are also required to extract the chirp information and feed into GNU Radio.

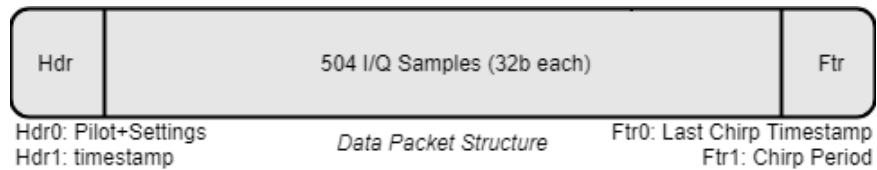


Figure 3.33: Chirp Sync New Data Packet Structure

Chapter 4

Experiments and Results

A set of experiments were performed to prove radar functionality and to ultimately implement or evaluate novel μ D and CR ideas. The experiments test the range and Doppler capabilities. Due to measurement limitations within the DU²SRI, strategic measurements were performed and performance was extrapolated.

4.1 Range

The range experiment involves setting up known or similar RCS objects to that of a Part 107 UAV in areas without sufficient clutter and measuring range with the intent of estimating the system's resolution ΔR and swath. The range performance will directly affect detection and tracking errors.

4.1.1 S-Band

The range test of the S-Band detection radar involves using a 25 inch diameter dish in the **DU²SRI** laboratory. The dish is placed far enough away from radar such that the frequency peak is clearly observable next to the leakage peak. The transmit frequency is set to 3.25 GHz. The chirp period is 38.85 μs and sample rate is 35 MHz, resulting in 1360 samples per chirp. The de-chirped signal is decimated by a factor of 12 prior to FFT peak finding. The transmit and receive gain is set to nominal values needed for close-range testing. After tuning out the self-leakage, Figure 4.1 shows the spectrum of the de-chirped signal. The FFT is zero-padded to show the underlining analog range bandwidth.

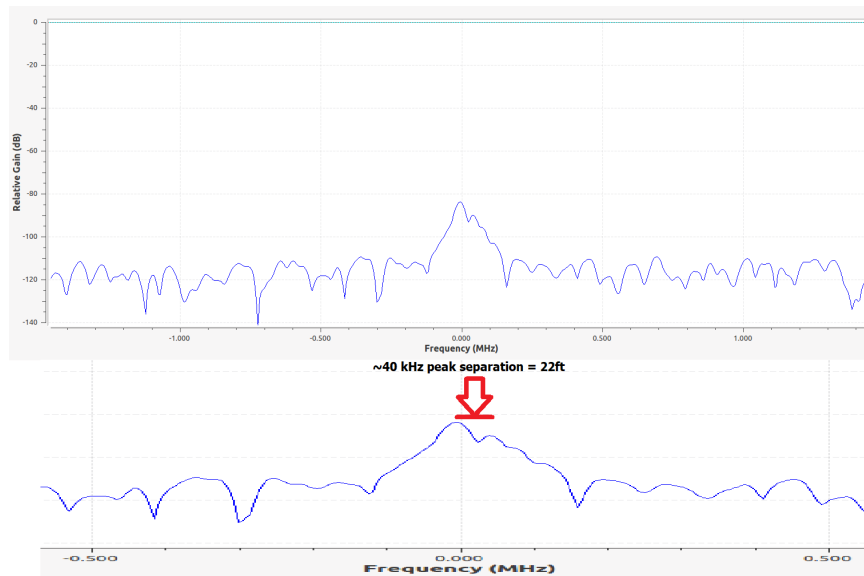


Figure 4.1: S-Band Range Test: Dish target at 22 feet

The target peak is correlated in real-time with target movement and measured to be 22 ft from the radar. Compensating for c , the LFM chirp has an effective slope of 545 ft/MHz. The target peak is found to be 40 kHz from the self isolation.

Multiplying by the LFM slope results in a range estimation of 21.8 *feet*. Since the dish is placed at a minimum observable distance next to another range peak, 22 *ft* is an empirically measured maximum range resolution. In FMCW radar, the range resolution is also the minimum measurable range. According to equation 3.7, 35 *MHz* has a theoretical Rayleigh Resolution of 14 *ft*. As expected, the theoretical is less than the empirical measured maximum.

4.1.2 X-Band

A range test involving the same 25 *inch* (0.635 *m*) dish is performed to verify range capabilities for the X-Band testbed. X-Band is expected to have higher range resolution than S-Band at the cost of the maximum detectable range. The dish is placed 20 *m* away in an open field with mild clutter from trees, cars, and buildings in the distance. A golf laser rangefinder is used to measure the distance and establish the ground truth. The X-Band testbed is set up facing the dish target. The entire radar scene is shown in Figure 4.2.

The function generator sets the stretched effective bandwidth $\beta_{rsp} = 267.05 \text{ MHz}$, $PRF = 1 \text{ kHz}$, and duty cycle of 50%. The waveform and microwave outputs are verified using an oscilloscope and spectrum analyzer. The SDR samples the IF at 5 *MHz*, low-pass filters, and decimates the signal by a factor of eight. The final sample rate is 312.5 *kHz*. Within GNU Radio, a simple FFT and peak finder locates the maximum frequency peak within $\pm 312.5 \text{ kHz}$. The speed of light is factored out and a final estimation of range is made. Figure 4.3 and 4.4 are the sampled chirp data in the time and frequency domain, respectively. The time plot shows the in-phase signal ($I(t)$) in red and quadrature signal ($Q(t)$) in blue. The



Figure 4.2: X-Band Range Test: Dish target at 20 meters

total chirp time is 0.5 ms or $1/2$ the PRI. The CW half of the PRI reduces the overlap between sequential chirps and allows efficient RSP given data processing rate limitations.

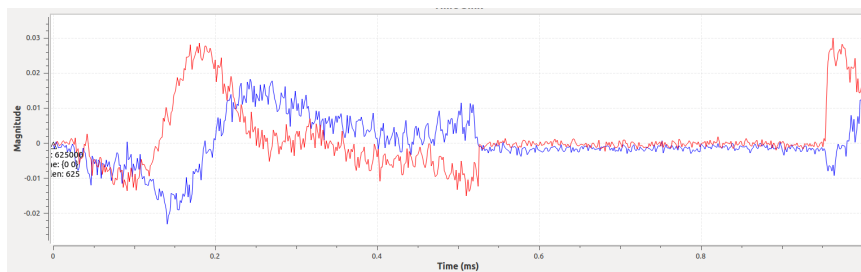


Figure 4.3: X-Band Range Test: Radar Chirp Samples vs. time

The spectrum of the chirp portion of the signal has distinct peaks along the positive direction at 73.34 kHz , 160 kHz , and 250 kHz . The slope of the chirp m is calculated in equation 4.1. From equation 3.9, each kHz represents about 28 cm . Using this calculation, the first peak corresponds to the dish at 20 m . The clutters of peaks at 160 kHz and 250 kHz correspond to clutter at 45 m and 70 m , respectively. Using the rangefinder, the first group is primarily from tree scattering. The second group is primarily from the cars and building across the road.

$$m = \frac{\Delta f}{\Delta \tau} = \frac{\beta_{rsp}}{PRI \cdot DC} = 534.1 \frac{Hz}{ns} \quad (4.1)$$

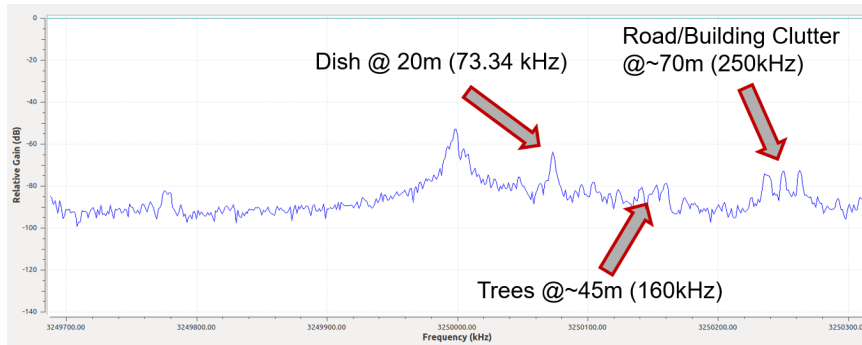


Figure 4.4: X-Band Range Test: Radar Chirp FFT

The dish's peak sits about 20 dB above the noise floor. According to the radar range equation, the power level is related to the inverse of R^4 . The dish's distance can increase by a factor of 3.16 before the peak falls into the noise floor. Any target with the same RCS as the dish will fall below the noise floor, $\chi \approx 0 \text{ dB}$, at approximately 63 m . According to Allen E. Fuhs in his RCS lectures, the RCS of a flat disk from the broad side is equal to πa^2 where a is the radius of the disk [146]. Thus, the RCS of a 0.3175 m radius dish can be approximated as 0.316 m^2 or $\approx -5 \text{ dBsm}$. From

the above approximations, a target with an RCS of 0 dBsm can be observed above $\chi = 0$ less than 85 m away.

Figure 4.5 is a snapshot of the real-time range measurements \hat{R} . The system starts with the transmit and receive gain practically off. Prior to five seconds, the transmit gain is turned to 50 dB and the receive gain is increased to a nominal value avoiding quantization noise from the ADC and amplifier saturation. At 15 seconds , the radar operator walks out from behind the radar, up to the target, and circles back to the radar. The operator's body shadows the target for this period of time.

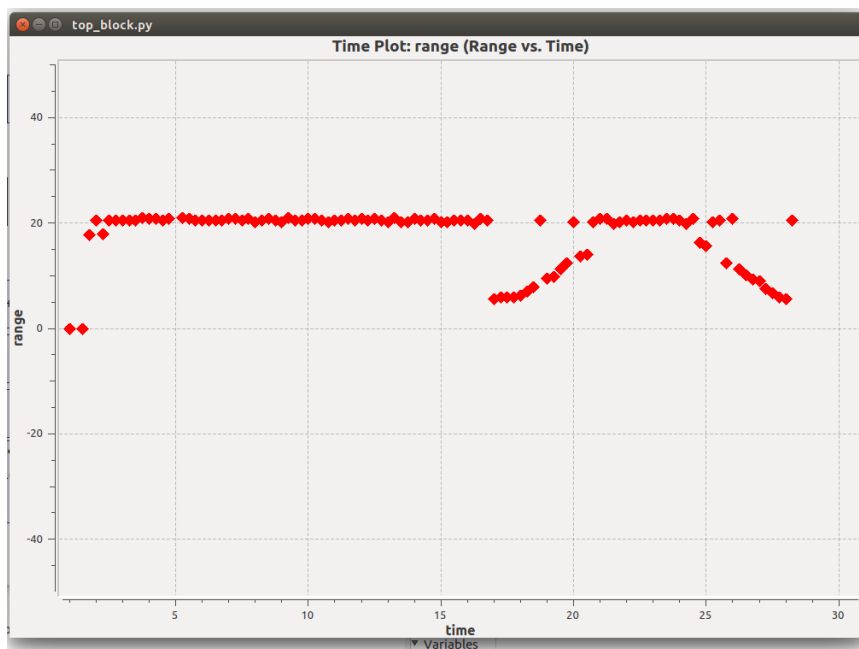


Figure 4.5: X-Band Range Test: Range Measurements

4.2 Doppler

Experiments are performed to prove Doppler capabilities for tracking and μ D functions. The velocity behavior for Part 107 UAVs limits the bulky Doppler shifts from frontal full speed (45 m/s) collision to 2.17 kHz and 7.00 kHz for S-Band and X-Band, respectively. A nominal speed of 10 m/s results in only a 216 Hz Doppler shift at S-Band. The low absolute Doppler shift of Part 107 UAVs leads to the requirement of higher frequency bands to accomplish tracking. Fundamentally, the effects of the Doppler shift can clearly be seen within the gathered samples at S-Band; however, in order to compute meaningful FFTs with discrete resolution in the Hz region, sufficiently long sample data packets must be stored and processed. One limitation of using SDRs is their inherent design for high-speed, making particularly slow measurements difficult to accomplish. This problem arises not only in the implementation but limits radar solutions which require quick electrical or mechanical scanning [42]. Thus, only X-Band was built and evaluated for Doppler performance.

4.2.1 X-Band

Two X-Band Doppler experiments are performed and analyzed. The first is an extension of the X-Band range experiment. The second is a real-time μ D analysis using a house fan.

Walking Person

Using the data collected from range experiment only when the radar operator walks into the radar scene, MATLAB is used to post-process the data to show more detail and analyze Doppler effects. First, Figure 4.6 plots the imaginary (red) and real (blue) signals between 20 – 38 seconds. At 22 seconds the operator moves in front of the radar antennas, and the high-energy return signal is observed above the noise. At 36 seconds, the operator returns to the radar and an increase in amplitude is again seen.

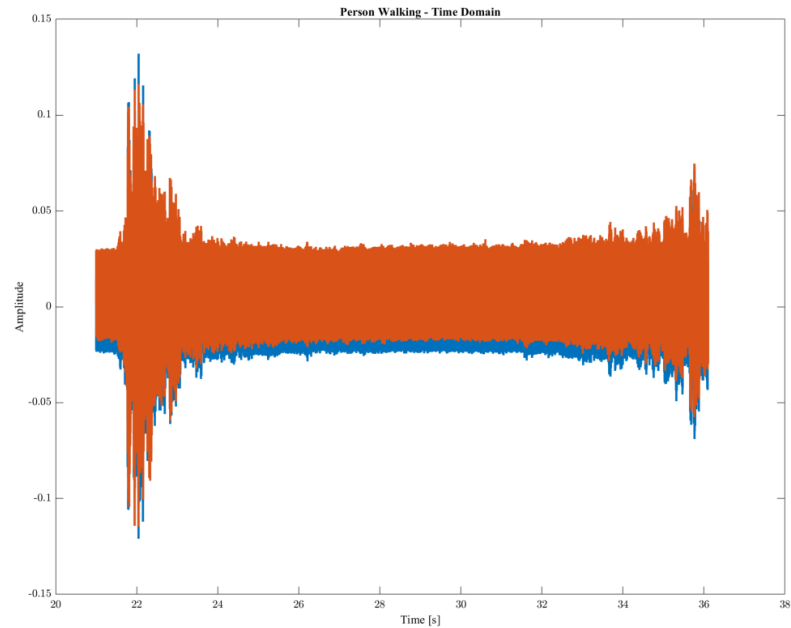


Figure 4.6: X-Band - Real (blue) and Imaginary (red) Radar Echo of Person Walking

The information about the range and velocity are not easily observable within the time-domain. Another signal processing tool called a spectrogram generates a TFR of the signal. The color-scale indicates the power of signal in frequency normalized

units. The top plot of Figure 4.7 is the “fast-time” spectrogram of the radar operator. The “fast-time” indicates the spectrum reveals high-frequency range information as generated by stretch-processing. Across the entire time frame, a peak is observed at 73 kHz or 20 m , correlating with the stationary dish target. At 1 second (referenced from start of Figure 4.6), the operator emerges in the scene. He first shadows the dish target and at sufficient distances, reflections from both operator and dish are observed. After circling around the target, the operator returns back to the radar. In the bottom plot, a decimation factor of 100 reduces the frequency range from 100 kHz to 1 kHz . This plot is referred to as the “slow-time” as longer wavelength features are explored. The Doppler shift from the operator’s movement is observed first as a negative shift as the operator moves away from the radar. At the end of the time-frame, a positive shift is observed. The shifts reach an absolute maximum of $\approx 200\text{ Hz}$ indicating a bulk velocity of $\approx 2.8\text{ m/s}$ (6 mph) or $7.0\frac{\text{s}}{20\text{m}}$. The speed is consistent with the range plots.

Micro-Doppler

To analyze Doppler effects, a 20 inch diameter box fan is used as a simulated rotor target. The fan has 5 curved blades which are covered with copper tape to improve reflection. The fan’s μD signature can be mathematically approximated using the rotor blade derivation applied to a single rotor hub with 5 blades found in [86] and described in Section 2.4.1. The SDR is programmed to CW mode and received samples are decimated to 40 kHz . The fan is placed 3 meters away from the radar testbed on a 20° angle and images are captured showing the μD of the fan off and on each of its three power settings. Figure 4.8 is an overlay of all four captured

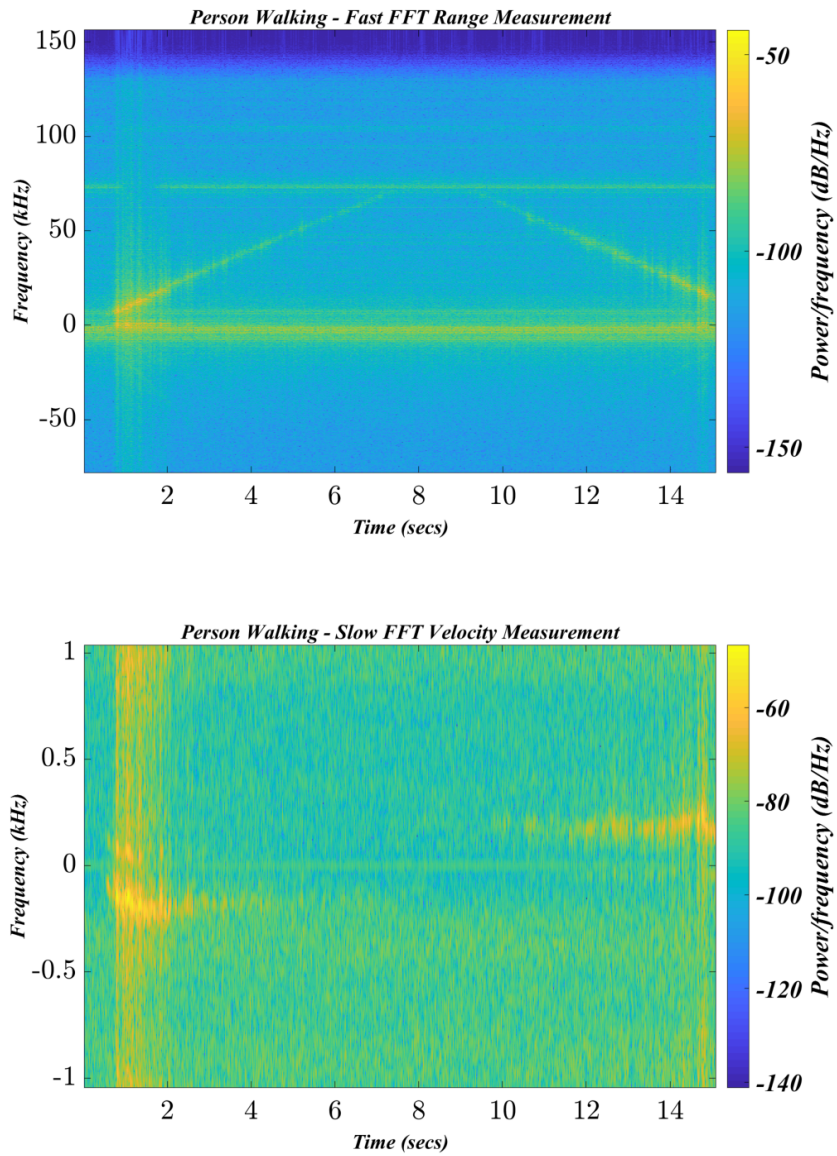


Figure 4.7: X-Band - Operator Walking - Fast/Slow Time Spectrograms

modes. The red trace shows fan in the off state. The resting target, noise floor, and SDR imperfection can be seen in this state. It provides context for the blue, yellow,

and green traces that show the μ D of the fan in all three power levels from least to greatest.

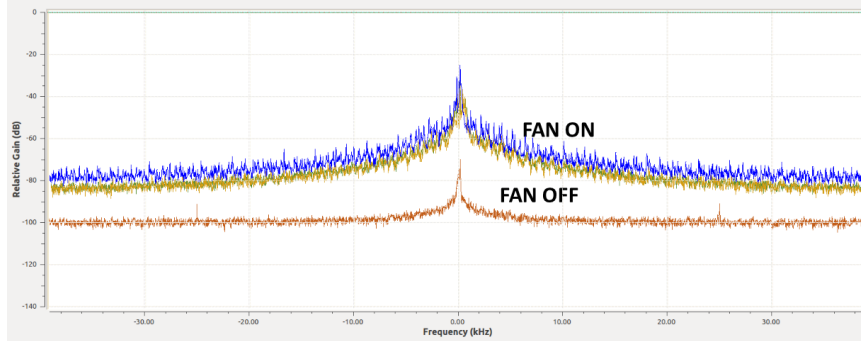


Figure 4.8: X-Band Micro-Doppler Contributions from a Metallic Fan

The entire band of the signal experiences a dramatic increase in power; however, a Doppler shift of 30 kHz would result from above mach one speeds, which is highly doubtful from a box fan. The general noise increase is assumed to be a byproduct of the testbed itself. The μ D from the fan is found in a much narrower bandwidth shown in Figure 4.9. Across $\pm 5 \text{ kHz}$, a μ D signature containing regular resonances similar to the measured DJI spectrum in Figure 2.23. The most narrow bandwidth ($\approx 2 - 3 \text{ kHz}$) is shown to increase as fan speed increases.

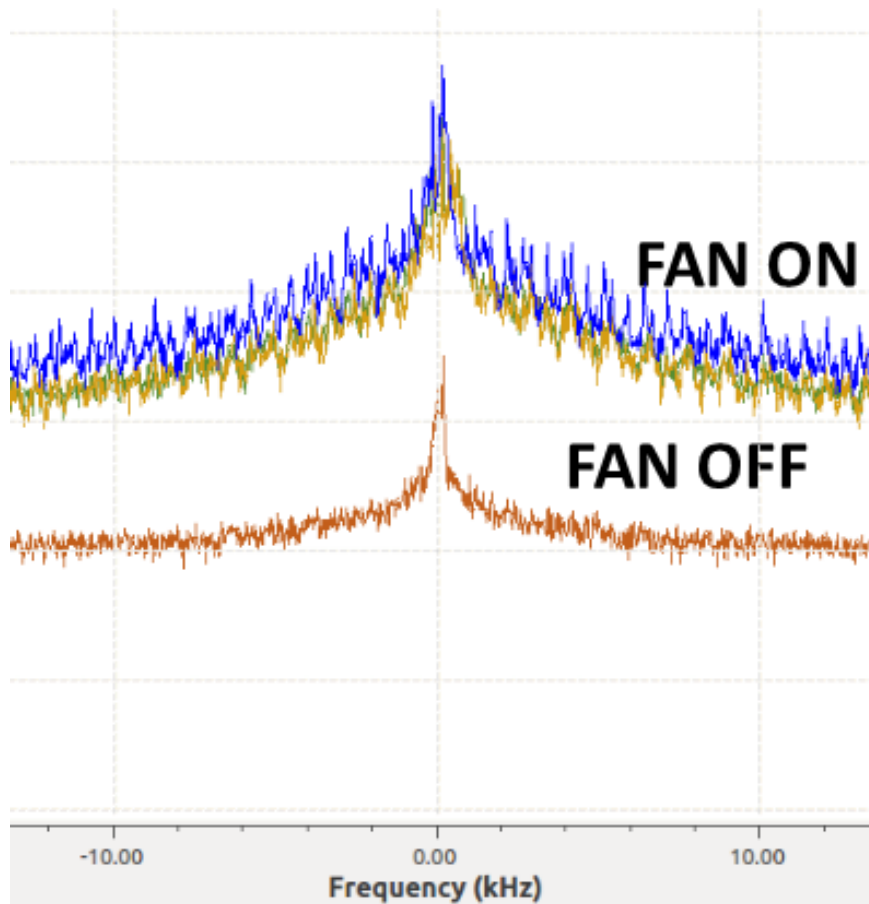


Figure 4.9: X-Band Micro-Doppler Contributions from a metallic fan - ZOOM

4.3 Testbed Results

Throughout the design process, observations were discovered about the performance and limitations of the specific design and components used, as well as larger benefits and issues with software-defined radars as a whole. Table 4.1 consolidates the radar performance results as a function of parameter. The desired performance will be met if the supported target parameter value is met or exceeded.

Performance	Parameter	Target Value	Units	Results
S-Band Detection				
	f_{tx}	S-Band	GHz	3.25 GHz
SNR	P_t	10	dBm	3.12 dBm
$\Delta R < 10m$	Bandwidth	> 15	MHz	35 MHz (4.28 m)
$\Delta V < 10 m/s$	T_D	4.62	ms	1.17 ms (39.6 m/s)
$R_{max} > 600m$	PRF	< 8	kHz	25.74 kHz (860 Hz min)
X-Band Tracking				
	f_{tx}	X-Band	GHz	10.5
SNR	P_t	10	dBm	12
$\Delta R < 1m$	Bandwidth	> 150	MHz	Stretched: 500 (< 60cm)
$\Delta V < 1m/s$	T_D	14.3	ms	8.16 ms (1.75 m/s)
$L_{fmcw} < 1$	PRF	< 50	kHz	1 kHz
Identification				
	f_{tx}	S-Band,X-Band		
$\Delta V < 1m/s$	Bandwidth	< 50	MHz	Packet length Restriction
$\Delta V < 1m/s$	T_D	> 14.3	ms	

Table 4.1: Radar Testbed Design Results

4.3.1 S-Band

For S-Band, the prototype operated at 3.25 GHz with a measured maximum output power of 3.12 dBm. The limited power output is a result of operating the LimeSDR at the upper limit of the device. A higher gain frontend amplifier can solve this problem. The LimeSDR's instantaneous β_{dig} is ultimately limited by USB 3.0 data rates or 61.44 MSps for a single SISO 1x1 channel. In practice however, to synchronize transmit and receive packets and maintain low packet loss, the sample-rate should be set to 35 MHz, which achieves the range accuracy performance target. Keeping the PRF less than 8 kHz while meeting all other power and sensitivity parameters will result in adequate SNR. A minimum PRF of 860 Hz is possible given a maximum radar waveform length of 1.17 ms.

One challenge with S-Band Doppler analysis is the required look-time or Doppler window T_D the target velocity swath. For S-Band 10 m velocity resolution, $T_D > 4.62 ms$. At 35 MHz sample rate, the signal processing chain must buffer 323,400 I/Q samples. To minimize latency, LimeSDR packetizes the data into 4096 *Byte* packets to be sent across USB 3.0. Each packet contains 1360, 12 *bit* I/Q samples. It was found, the GNU Radio software-implemented stretched process can process approximately 30 packets prior to running into packet loss and/or buffer overloading. While maintaining a 35 MHz sample rate, a maximum $T_D = 1.17 ms$ can achieve a velocity resolution of $\approx 40 m/s$. If the sample rate is reduced to the LimeSDR minimum 5 MHz , the Doppler processing window has maximum of 8.15 ms . While meeting S-Band velocity resolution requirements, the system can not simultaneously measure range and velocity. This problem is an extension of the range-velocity dilemma as mentioned in Section A.1.3 applied to the range and velocity resolutions. For software-implemented FMCW systems, the maximum processing window or maximum T_D is limited by the number of maximum buffer length in samples N_{max} scaled by sample rate or β_{rsp} . The range and velocity resolution, ΔR and ΔV , is related to T_D from equations 3.7 and 3.8. Combining the resolution equations and solving N_{max} results in equation 4.2 or the *Range-Velocity Uncertainty*.

$$\Delta R \cdot \Delta V = \lambda \frac{c}{4N_{max}} \quad (4.2)$$

From a radar parameters perspective, equation 4.3 factors out the speed of light and the transmit frequency of the radar system. This bandwidth-Doppler tradeoff will occur in any software-implemented FMCW (or stretched) RSP, and is limited by the total processing window length. The minimum separable Doppler frequency or

Rayleigh resolution of the radar Doppler shift Δf_{Dr} is directly related to the velocity resolution ΔV as seen in equation 3.8. Some strategies to overcome processing buffer limitations are sequential decimation, adding more memory, or implementing RSP within the FPGA itself. This limitation can easily be overlooked when designing SDRads.

$$\frac{\beta_{rsp}}{\Delta f_{Dr}} = N_{max} \quad (4.3)$$

In addition to extending the processing window, implementing the RSP in a secondary, chirped-LO heterodyne conversion stage will eliminate the direct relationship between RSP bandwidth β_{rsp} and minimum-detectable Doppler frequency shift Δf_{Dr} . Thus, long Doppler processing windows and high velocity resolution can be achieved while maintaining high range resolution. The Doppler frequency shift resolution is shown in equation 4.4.

$$\Delta f_{Dr} = \frac{\beta_s}{N} \quad (4.4)$$

4.3.2 X-Band

For X-Band, the prototype operated at 10.5 *GHz* with a measured maximum output power of 12 *dBm*. Implementing a stretch-bandwidth process in hardware via a chirped LO increases potential β_{rsp} up to 500 *MHz* resulting in $\Delta R < 60$ *cm*. The hardware implemented stretch process decouples the range-velocity resolution dilemma described above. However, the LimeSDR minimum sample rate of 5 *MHz* limits the velocity resolution independent to β_{rsp} . The maximum Doppler processing

window is 8.16 *ms* and the minimum velocity resolution is 1.75 *m/s*. The velocity limitation is an important design consideration when selecting SDR technology, and it is an important example of how the entire signal processing chain must be considered when designing SDRads or radar systems as a whole.

Chapter 5

Results and Discussion

5.1 Conclusion

This research focuses on a small sub-set of the solution required for safe UAV flight integration into the NAS; radar SAA sensor performance. The final contribution is a dual band software-defined radar testbed for rapid prototyping novel radar techniques: Micro-Doppler and Cognitive Radar. The thesis resulted in first generation prototypes for S-Band detection and X-Band tracking and identification radar prototyping. The main goal of enabling rapid prototyping of CR is accomplished by implementing flexible, software-defined hardware to allow implementation of “pulse-to-pulse” control or optimization. The testbed also offers the ability to generate a comprehensive database of UAV μ D echoes to train machine learning identification. Further, the testbed is repeatable and cost-efficient compared to similar laboratory SDRads, thus allowing the collaboration of a wide variety of university or industrial laboratories into the wider UAS or radar research community.

Wide-scale, comprehensive μ D RTI database creation is integral for successfully solving the identification problem.

The design of the testbed prototypes are portable, repeatable, and scalable. The final parts cost of both prototypes is \$5,000. The S-Band testbed operates off of less than one Watt. The X-Band operates off of less than four Watts, and both testbeds can fit on a $< 1/3$ square meter portable cart. The low SWaP allows for portability of the entire system to move to various environments to collect data or evaluate high-clutter performance. The system can be powered by an extension cord or standard lithium batteries. Prior to extensive field work, an operator or researcher is required to obtain an FCC experimentation license in order to avoid potential legal issues. However, a few options exist without currently holding an explicit FCC license. A few Industrial, Scientific, and Medical (ISM) radio bands exist at the UHF, S-Band, C-Band, K-Band, V-Band, and W-Band. For low-power use, the FCC allows for “Intentional Radiators” at radiation power depending on frequency and application [147].

The prototypes are comprised of low-cost, commercially available parts, systems, or manufacturing techniques, and the SDR uses entirely open-source software and hardware design. The result is a low-cost, repeatable testbed design which can accelerate UAV radar SAA sensor development and integration into CASs, not only in **DU²SRI** but in the wider UAS research community. The X-Band frequency converter architecture is also designed to be scalable to higher-frequency bands while still integrating into the same data-acquisition and software environment. The design and software source-code is published on Github [148].

The testbeds are evaluated for functionality and performance with emphasis on its overall CAS function. The evaluations use FMCW waveforms however, alternate or novel waveform design can be considered. One major limitation when implementing FMCW or other LFM plus CW radars within a software-defined architecture is the total available processing window of the entire signal processing chain. This limitation is explored and defined in terms of fundamental radar parameters. The processing window ultimately limits the combined range-velocity resolution in a software-implemented stretched RSP. This can be thought of as the *Range-Velocity Uncertainty*. Potential solutions are provided including implementing the stretched RSP in hardware.

Overall, it is hoped that future engineers, scientists, and hobbyists find the work presented in this thesis useful as they pursue research and development of the next generation of radar SAA sensors. As the development of algorithms grows to meet the complexity of natural phenomena, so too must its evaluation.

5.2 Future Work

This thesis concludes the development, implementation, and basic evaluation of testbed performance which now enables rapid prototyping of novel radar techniques for UAV detection, tracking and identification. Basic evaluation of the testbed resulted in limitations and potential improvements to be considered when developing sequential versions. Data synchronicity, packet-loss, self-interference, and calibration can all be improved to make more robust or accurate measurements. The synchronicity and packet-loss can be improved by modifying HDL or driver software. Reducing

the self-interference will require either improved microwave frontend design to reduce coupling from transmitter to receiver or by leakage cancellation techniques [149, 150]. In addition to LimeSDR on-chip filter, DC, and I/Q corrections, conversion board and frontend non-linearities can be corrected within the radar waveform, on-chip DSP, or backend software.

In addition, development of more sophisticated testbeds with larger processing windows, larger bandwidths, and higher transmit frequencies will increase performance to any level researchers might require. Additional functionality can also be implemented such as making the SDRad potentially deployable or a MIMO expansion. The future research to be enabled includes UAV μ D RTI machine learning evaluation, adaptive stimulus implementation, waveform design prototyping, or any novel radar technique which uses LFM or more complex.

Deployment

Eventual deployment of future SDRads based on SDR technology requires additional engineering hours in order to minimize SWaP and reliability. The first step is to mount all MMIC which are inside the SMA Mini-Circuits parts onto one monolithic frequency conversion microwave PCB. The estimated size of the PCB will be similar to that of the LimeSDR board or roughly 100 cm^2 . Additional mountable small scale patch antennas can enable full 360 degree coverage via electronic beam-steering. Beam-steering requires either analogue or digital beam-forming or phased arrays. Analogue beam-forming channels are phased and combined either prior to the first frequency conversion stage or prior to the LimeSDR conversion stage. The latter requires duplicate microwave components for improved performance and

is typically referred to as a more “Active” phased array. A single chirped LO and/or a single baseband processor on the LimeSDR will multiplex all steering angles. For faster control and multiple simultaneous beams, additional LimeSDRs synchronized in parallel can process all channels distributively using digital beam-forming. This essentially uses beam angle multiplexing instead of time domain multiplexing by placing an additional processing load on the host processor. To implement, synchronization between multiple parallel SDRs will be the most challenging task.

MIMO

Along with testing various radar waveforms and higher-level adaptive control, the additional synchronized channels can be implemented in parallel to enable MIMO radar for potential added performance over standard beam-forming techniques [151, 152]. For full MIMO functionality, each transmit and receive channel is required to be digitally separate similar to digital beam-forming. The channels must also be uncorrelated via time-multiplexing or orthogonal signals. The radiating elements can now be placed in a strategic pattern to create a virtual array with more effective elements than the physical array itself. The virtual elements are created from each combination of transmit and receive elements.

UAV Database

As the primary motivation for the development of this testbed, a μ D UAV database is recommended for not only SAA application but also anti-UAV and airspace management as a whole. A comprehensive database should include a wide range of UAV types and control clutter recorded in many different environments

with various amounts of noise present. The UAVs should record at various angles and transmit frequencies. The clutter should include target-less scenes as well as non-UAV targets such as birds, larger aircraft, and other vehicles. The creation of such a database is a requirement of successfully implementing a real-world, statistically-based μ D RTI system.

Bibliography

- [1] *Pilot's Handbook of Aeronautical Knowledge*, Federal Aviation Administration, Aug 2016.
- [2] L. Dorr, "Fact Sheet - Small Unmanned Aircraft Regulations (Part 107)," Federal Aviation Administration, Tech. Rep., July 2018. [Online]. Available: https://www.faa.gov/news/fact_sheets/news_story.cfm?newsId=22615
- [3] "Right-of-way rules: Except water operations." Title 14 CFR 91.113, Federal Aviation Administration, 2004.
- [4] "Integration of Civil Unmanned Aircraft Systems (UAS) in the National Airspace System (NAS) Roadmap," Federal Aviation Administration, July 2018.
- [5] *Introduction to TCAS II Version 7.1*, Federal Aviation Administration, Feb 2011.
- [6] *Owner's Manual*, ZAON Flight systems, 2008.
- [7] (2008) Flarm Technologies. [Online]. Available: <http://www.flarm.com/>
- [8] (2011) ADS-B Technologies. [Online]. Available: <http://www.ads-b.com/>
- [9] G. Fasano, D. Accado, A. Moccia, and D. Moroney, "Sense and avoid for unmanned aircraft systems," *IEEE Aerospace and Electronic Systems Magazine*, vol. 31, no. 11, pp. 82–110, November 2016.
- [10] V. C. Chen, *The Micro-Doppler Effect in Radar*. Artech House, 2011.

- [11] S. Haykin, "Cognitive Radar: a way of the future," *IEEE Signal Processing Magazine*, vol. 23, no. 1, pp. 30–40, Jan 2006.
- [12] *FCC Online Table of Frequency Allocation*, 47 C.F.R. Â§ 2.106, Federal Communications Commission Std., 2018. [Online]. Available: <https://transition.fcc.gov/oet/spectrum/table/fcctable.pdf>
- [13] F. C. White, "Is an airborne system for collision avoidance operationally and technically feasible?" *IRE Transactions on Aeronautical and Navigational Electronics*, vol. ANE-4, no. 2, pp. 72–74, June 1957.
- [14] E. O. Frye and D. E. Killham, "Aircraft collision avoidance systems," *IEEE Spectrum*, vol. 3, no. 1, pp. 72–80, Jan 1966.
- [15] R. E. Perkinson and F. D. Watson, "Airborne collision avoidance and other applications of time/frequency," *Proceedings of the IEEE*, vol. 60, no. 5, pp. 572–579, May 1972.
- [16] K. M. Fahey and M. J. Miller, "Unmanned systems integrated roadmap FY2017-2042," Department of Defense. [Online]. Available: http://cdn.defensedaily.com/wp-content/uploads/post_attachment/206477.pdf
- [17] R. T. Ogan, "Integration of manned and unmanned aircraft systems into u.s. airspace," in *IEEE Southeast Con 2014*, March 2014, pp. 1–4.
- [18] A. Canolla, M. B. Jamoom, and B. Pervan, "Interactive multiple model sensor analysis for Unmanned Aircraft Systems (UAS) Detect and Avoid (DAA)," in *2018 IEEE/ION Position, Location and Navigation Symposium (PLANS)*, April 2018, pp. 757–766.
- [19] J. A. Douthwaite, A. D. Freitas, and L. S. Mihaylova, "An interval approach to multiple unmanned aerial vehicle collision avoidance," in *2017 Sensor Data Fusion: Trends, Solutions, Applications (SDF)*, Oct 2017, pp. 1–8.
- [20] A. D. Zeitlin, "Sense & avoid capability development challenges," *IEEE Aerospace and Electronic Systems Magazine*, vol. 25, no. 10, pp. 27–32, Oct 2010.

- [21] G. Fasano, D. Accardo, A. E. Tirri, and A. Moccia, “Experimental analysis of onboard non-cooperative sense and avoid solutions based on radar, optical sensors, and data fusion,” *IEEE Aerospace and Electronic Systems Magazine*, vol. 31, no. 7, pp. 6–14, July 2016.
- [22] S. Ramasamy, R. Sabatini, and A. Gardi, “Cooperative and non-cooperative sense-and-avoid in the CNS+A context: A unified methodology,” in *2016 International Conference on Unmanned Aircraft Systems (ICUAS)*, June 2016, pp. 531–539.
- [23] J. A. Jackson, J. D. Bošković, and D. Diel, “Sensor fusion for sense and avoid for small uas without ADS-B,” in *2015 International Conference on Unmanned Aircraft Systems (ICUAS)*, June 2015, pp. 784–793.
- [24] K. P. Valavanis, “Unmanned aircraft systems challenges in design for autonomy,” in *2017 11th International Workshop on Robot Motion and Control (RoMoCo)*, July 2017, pp. 73–86.
- [25] S. Ramasamy, R. Sabatini, and A. Gardi, “Avionics sensor fusion for small size unmanned aircraft sense-and-avoid,” in *2014 IEEE Metrology for Aerospace (MetroAeroSpace)*, May 2014, pp. 271–276.
- [26] A. Finn and S. Franklin, “Acoustic sense & avoid for UAV’s,” in *2011 Seventh International Conference on Intelligent Sensors, Sensor Networks and Information Processing*, Dec 2011, pp. 586–589.
- [27] X. Yang, K. Huo, W. Jiang, J. Zhao, and Z. Qiu, “A passive radar system for detecting UAV based on the OFDM communication signal,” in *2016 Progress in Electromagnetic Research Symposium (PIERS)*, Aug 2016, pp. 2757–2762.
- [28] C. Schüpbach, C. Patry, F. Maasdorp, U. Böniger, and P. Wellig, “Micro-UAV detection using DAB-based passive radar,” in *2017 IEEE Radar Conference (RadarConf)*, May 2017, pp. 1037–1040.

- [29] A. Aldowesh, M. Shoaib, K. Jamil, S. Alhumaidi, and M. Alam, “A passive bistatic radar experiment for very low radar cross-section target detection,” in *2015 IEEE Radar Conference*, Oct 2015, pp. 406–410.
- [30] M. A. Richards, *Fundamentals of Radar Signal Processing*. United States: McGraw-Hill Education, 2014.
- [31] D. S. Hicok and D. Lee, “Application of ADS-B for airport surface surveillance,” in *17th DASC. AIAA/IEEE/SAE. Digital Avionics Systems Conference. Proceedings (Cat. No.98CH36267)*, vol. 2, Oct 1998, pp. F34/1–F34/8 vol.2.
- [32] E. Frew and R. Sengupta, “Obstacle avoidance with sensor uncertainty for small unmanned aircraft,” in *2004 43rd IEEE Conference on Decision and Control (CDC) (IEEE Cat. No.04CH37601)*, vol. 1, Dec 2004, pp. 614–619 Vol.1.
- [33] E. J. Rodríguez-Seda, D. M. Stipanović, and M. W. Spong, “Collision avoidance control with sensing uncertainties,” in *Proceedings of the 2011 American Control Conference*, June 2011, pp. 3363–3368.
- [34] E. J. Rodríguez-Seda, D. M. Stipanović, and M. W. Spong, “Lyapunov-based cooperative avoidance control for multiple lagrangian systems with bounded sensing uncertainties,” in *2011 50th IEEE Conference on Decision and Control and European Control Conference*, Dec 2011, pp. 4207–4213.
- [35] S. Ramasamy, R. Sabatini, and A. Gardi, “A unified approach to separation assurance and collision avoidance for flight management systems,” in *2016 IEEE/AIAA 35th Digital Avionics Systems Conference (DASC)*, Sept 2016, pp. 1–8.
- [36] J. A. Douthwaite, A. D. Freitas, and L. S. Mihaylova, “An interval approach to multiple unmanned aerial vehicle collision avoidance,” in *2017 Sensor Data Fusion: Trends, Solutions, Applications (SDF)*, Oct 2017, pp. 1–8.

- [37] H. Hertz, *Electric Waves: Being Researches on The Propagation of Electric Action with Finite Velocity Through Space*. Dover Publications, 1893. [Online]. Available: <https://archive.org/details/b2172457x/page/n7>
- [38] A. Bauer. (2005) Christian hulsmeyer and about the early days of radar inventions. [Online]. Available: <https://aobauer.home.xs4all.nl/Koeln%202006%20ppt.pdf>
- [39] G. Goebel. Microwave Radar at War. [Online]. Available: http://vc.airvectors.net/ttwiz_04.html
- [40] M. Skolnik, *Radar Handbook*. McGraw-Hill Education, 2008.
- [41] D. M. Pozar, *Microwave Engineering*. John Wiley & Sons, 1990.
- [42] S. Kemkemian, M. Nouvel-Fiani, P. Cornic, P. L. Bihan, and P. Garrec, "Radar systems for "Sense and Avoid" on UAV," in *2009 International Radar Conference "Surveillance for a Safer World" (RADAR 2009)*, Oct 2009, pp. 1–6.
- [43] Y. K. Kwag and C. H. Chung, "UAV based collision avoidance radar sensor," in *2007 IEEE International Geoscience and Remote Sensing Symposium*, July 2007, pp. 639–642.
- [44] A. Moses, M. J. Rutherford, and K. P. Valavanis, "Radar-based detection and identification for miniature air vehicles," in *2011 IEEE International Conference on Control Applications (CCA)*, Sept 2011, pp. 933–940.
- [45] A. Moses, "Radar based collision avoidance for unmanned aircraft systems," Ph.D. dissertation, University of Denver, 2013.
- [46] A. F. Scannapieco, A. Renga, G. Fasano, and A. Moccia, "Ultralight radar sensor for autonomous operations by micro-UAS," in *2016 International Conference on Unmanned Aircraft Systems (ICUAS)*, June 2016, pp. 727–735.
- [47] W. Simon, T. Klein, and O. Litschke, "Small and light 24 GHz multi-channel radar," in *2014 IEEE Antennas and Propagation Society International Symposium (APSURSI)*, July 2014, pp. 987–988.

- [48] E. Itcia, J.-P. Wasselin, S. Mazuel, and M. O. and Albert Huizing, “FMCW radar for the sense function of sense and avoid systems onboard UAVs,” pp. 8899 – 8899 – 5, 2013. [Online]. Available: <https://doi.org/10.1117/12.2028518>
- [49] J. Mackie, J. Spencer, and K. F. Warnick, “Compact FMCW radar for a UAS Sense and Avoid system,” in *2014 IEEE Antennas and Propagation Society International Symposium (APSURSI)*, July 2014, pp. 989–990.
- [50] S. Futatsumori, A. Kohmura, and N. Yonemoto, “Compact and high-performance 76 GHz millimeter-wave radar front-end module for autonomous unmanned helicopters,” in *2011 8th European Radar Conference*, Oct 2011, pp. 21–24.
- [51] “AWR1642 data sheet,” Texas Instruments, 2018. [Online]. Available: <http://www.ti.com/product/AWR1642>
- [52] “MR3003 data sheet,” NXP Semiconductors, 2018. [Online]. Available: <https://www.nxp.com/products/rf/radar-transceivers/mr3003-high-performance-77-ghz-radar-transceiver:MR3003>
- [53] (2018) Automotive RADAR. Analog Devices, Inc. [Online]. Available: <http://www.analog.com/en/applications/markets/automotive-pavilion-home/autonomous-transportation-and-adas/automotive-radar.html>
- [54] (2018) Fortem TrueView. Fortem Technologies. [Online]. Available: <https://fortemtech.com/products/trueview-radar/>
- [55] T. Maguire, “Wireless telecommunications bureau seeks comment on echodyne corporation request for waiver to permit licensing and use of ground-based 24.45-24.65 GHz radar,” Public Notice, December 2017. [Online]. Available: <https://www.fcc.gov/document/comment-sought-echodyne-request-ground-based-24-ghz-radar>
- [56] (2018) LimeSDR: Flexible, next-generation, open source software-defined radio. Crowd Supply. [Online]. Available: <https://www.crowdsupply.com/lime-micro/limesdr>

- [57] M. T. Frankford, N. Majurec, and J. T. Johnson, "Software-defined radar for MIMO and adaptive waveform applications," in *2010 IEEE Radar Conference*, May 2010, pp. 724–728.
- [58] S. Baskar and E. Ertin, "A software defined radar platform for waveform adaptive MIMO radar research," in *2015 IEEE Radar Conference (RadarCon)*, May 2015, pp. 1590–1594.
- [59] (2010) Small Form Factor (SFF) Software Defined Radio (SDR) Development Platform. Texas Instruments. [Online]. Available: <http://www.ti.com/tool/TMDSSFFSDR>
- [60] C. W. Rossler, E. Ertin, and R. L. Moses, "A software defined radar system for joint communication and sensing," in *2011 IEEE RadarCon (RADAR)*, May 2011, pp. 1050–1055.
- [61] J. M. Christiansen, G. E. Smith, and K. E. Olsen, "USRP based cognitive radar testbed," in *2017 IEEE Radar Conference (RadarConf)*, May 2017, pp. 1115–1118.
- [62] K. Stasiak and P. Samczynski, "FMCW radar implemented in SDR architecture using a USRP device," in *2017 Signal Processing Symposium (SPSymposium)*, Sept 2017, pp. 1–5.
- [63] S. Costanzo, F. Spadafora, A. Borgia, H. O. Moreno, A. Costanzo, and G. DiMassa, "High resolution software defined radar system for target detection," *JECE*, vol. 2013, Jan. 2013. [Online]. Available: <http://dx.doi.org/10.1155/2013/573217>
- [64] J. Hershberger, T. Pratt, and R. Kossler, "A software-defined, dual-polarized radar system," in *2016 IEEE Conference on Antenna Measurements Applications (CAMA)*, Oct 2016, pp. 1–4.
- [65] S. Prager, T. Thrivikraman, M. Haynes, J. Stang, D. Hawkins, and M. Moghadam, "Ultra-wideband synthesis for high-range resolution software defined

- radar,” in *2018 IEEE Radar Conference (RadarConf18)*, April 2018, pp. 1089–1094.
- [66] S. Sundaresan, C. Anjana, T. Zacharia, and R. Gandhiraj, “Real time implementation of FMCW radar for target detection using GNU Radio and USRP,” in *2015 International Conference on Communications and Signal Processing (ICCSP)*, April 2015, pp. 1530–1534.
- [67] Y. L. Sit, B. Nuss, S. Basak, M. Orzol, W. Wiesbeck, and T. Zwick, “Real-time 2D+velocity localization measurement of a simultaneous-transmit OFDM MIMO radar using software defined radios,” in *2016 European Radar Conference (EuRAD)*, Oct 2016, pp. 21–24.
- [68] Y. Kwag, J. Jung, I. Woo, and M. Park, “Multi-band multi-mode SDR radar platform,” in *2015 IEEE 5th Asia-Pacific Conference on Synthetic Aperture Radar (APSAR)*, Sept 2015, pp. 46–49.
- [69] Y. Kwag, I. Woo, H. Kwak, and Y. Jung, “Multi-mode SDR radar platform for small air-vehicle drone detection,” in *2016 CIE International Conference on Radar (RADAR)*, Oct 2016, pp. 1–4.
- [70] I. Woo, J. Jung, M. Park, and Y. Kwag, “Software defined radar platform testbed for micro-Doppler detection,” in *2015 IEEE 5th Asia-Pacific Conference on Synthetic Aperture Radar (APSAR)*, Sept 2015, pp. 50–53.
- [71] Y. Kwag and I. Woo, “Multi-band multi-mode SDR radar platform for traffic and security applications,” in *2016 URSI Asia-Pacific Radio Science Conference (URSI AP-RASC)*, Aug 2016, pp. 1182–1183.
- [72] E. Kennaugh and R. Cosgriff, “The use of impulse response in electromagnetic scattering problems,” in *1958 IRE International Convention Record*, vol. 6, March 1958, pp. 72–77.
- [73] E. M. Kennaugh and D. L. Moffatt, “Transient and impulse response approximations,” *Proceedings of the IEEE*, vol. 53, no. 8, pp. 893–901, Aug 1965.

- [74] D. Moffatt and R. Mains, "Detection and discrimination of radar targets," *IEEE Transactions on Antennas and Propagation*, vol. 23, no. 3, pp. 358–367, May 1975.
- [75] M. V. Blaricum, L. Pearson, and R. Mittra, "An efficient scheme for radar target recognition based on the complex natural resonances of the target," in *1975 Antennas and Propagation Society International Symposium*, vol. 13, June 1975, pp. 416–419.
- [76] W. Goggins, P. Blacksmith, and C. Sletten, "Phase signature radars," *IEEE Transactions on Antennas and Propagation*, vol. 22, no. 6, pp. 774–780, November 1974.
- [77] Y. Lin and A. Ksienski, "Utilization of phase information in radar target identification," in *1973 Antennas and Propagation Society International Symposium*, vol. 11, April 1973, pp. 29–29.
- [78] R. Strattan, "Target identification from radar signatures," in *ICASSP '78. IEEE International Conference on Acoustics, Speech, and Signal Processing*, vol. 3, April 1978, pp. 223–227.
- [79] E. Kennaugh, "The K-pulse concept," *IEEE Transactions on Antennas and Propagation*, vol. 29, no. 2, pp. 327–331, March 1981.
- [80] F. Fok, D. Moffatt, and N. Wang, "K-pulse estimation from the impulse response of a target," *IEEE Transactions on Antennas and Propagation*, vol. 35, no. 8, pp. 926–933, August 1987.
- [81] E. Rothwell, K. Chen, D. Nyquist, N. Gharsallah, and B. Drachman, "Frequency domain E-pulse synthesis and target discrimination," in *1985 Antennas and Propagation Society International Symposium*, vol. 23, June 1985, pp. 285–288.
- [82] F. Fok and D. Moffatt, "The K-pulse and E-pulse," *IEEE Transactions on Antennas and Propagation*, vol. 35, no. 11, pp. 1325–1326, November 1987.

- [83] K.-M. Chen, D. Nyquist, E. Rothwell, L. Webb, and B. Drachman, "Radar target discrimination by convolution of radar return with extinction-pulses and single-mode extraction signals," *IEEE Transactions on Antennas and Propagation*, vol. 34, no. 7, pp. 896–904, July 1986.
- [84] D. Blanco, M. Morante, J. Rodr guez, J. A. Garz n-Guerrero, M. C. Carri n, and J. F. G mez-Lopera, "Noncooperative radar target discrimination by extinction pulses using exponential β -splines," *IEEE Transactions on Antennas and Propagation*, vol. 64, no. 11, pp. 4887–4890, Nov 2016.
- [85] M. M. Moreno, D. B. Navarro, and M. C. C. P rez, "Radar target discrimination with extinction pulses using exponential β -splines," in *2015 9th European Conference on Antennas and Propagation (EuCAP)*, April 2015, pp. 1–4.
- [86] V. C. Chen, "Analysis of radar micro-Doppler with time-frequency transform," in *Proceedings of the Tenth IEEE Workshop on Statistical Signal and Array Processing (Cat. No.00TH8496)*, Aug 2000, pp. 463–466.
- [87] B. D. Bullard and P. C. Dowdy, "Pulse Doppler signature of a rotary-wing aircraft," *IEEE Aerospace and Electronic Systems Magazine*, vol. 6, no. 5, pp. 28–30, May 1991.
- [88] M. A. Govoni, "Micro-Doppler signal decomposition of small commercial drones," in *2017 IEEE Radar Conference (RadarConf)*, May 2017, pp. 0425–0429.
- [89] A. Herschfelt, C. R. Birtcher, R. M. Gutierrez, Y. Rong, H. Yu, C. A. Balanis, and D. W. Bliss, "Consumer-grade drone radar cross-section and micro-Doppler phenomenology," in *2017 IEEE Radar Conference (RadarConf)*, May 2017, pp. 0981–0985.
- [90] S. Harman, "Analysis of the radar return of micro-UAVs in flight," in *2017 IEEE Radar Conference (RadarConf)*, May 2017, pp. 1159–1164.

- [91] O. H. Y. Lam, R. Kulke, M. Hagelen, and G. Mellenbeck, "Classification of moving targets using micro-Doppler radar," in *2016 17th International Radar Symposium (IRS)*, May 2016, pp. 1–6.
- [92] J. J. M. de Wit, R. I. A. Harmanny, and G. Prémel-Cabic, "Micro-Doppler analysis of small UAVs," in *2012 9th European Radar Conference*, Oct 2012, pp. 210–213.
- [93] M. Jahangir, C. J. Baker, and G. A. Oswald, "Doppler characteristics of micro-drones with L-band multibeam staring radar," in *2017 IEEE Radar Conference (RadarConf)*, May 2017, pp. 1052–1057.
- [94] L. Fuhrmann, O. Biallawons, J. Klare, R. Panhuber, R. Klenke, and J. Ender, "Micro-Doppler analysis and classification of UAVs at Ka band," in *2017 18th International Radar Symposium (IRS)*, June 2017, pp. 1–9.
- [95] J. A. Nanzer and V. C. Chen, "Microwave interferometric and Doppler radar measurements of a UAV," in *2017 IEEE Radar Conference (RadarConf)*, May 2017, pp. 1628–1633.
- [96] M. Jian, Z. Lu, and V. C. Chen, "Experimental study on radar micro-Doppler signatures of unmanned aerial vehicles," in *2017 IEEE Radar Conference (RadarConf)*, May 2017, pp. 0854–0857.
- [97] X. Qi, T. Wang, and J. Liu, "Comparison of support vector machine and softmax classifiers in computer vision," in *2017 Second International Conference on Mechanical, Control and Computer Engineering (ICMCCE)*, Dec 2017, pp. 151–155.
- [98] M. F. Amasyali and O. K. Ersoy, "Comparison of single and ensemble classifiers in terms of accuracy and execution time," in *2011 International Symposium on Innovations in Intelligent Systems and Applications*, June 2011, pp. 470–474.
- [99] M. S. Andrić, B. P. Bondžulić, and B. M. Zrnić, "The database of radar echoes from various targets with spectral analysis," in *10th Symposium on Neural Network Applications in Electrical Engineering*, Sept 2010, pp. 187–190.

- [100] P. Molchanov, K. Egiazarian, J. Astola, R. I. A. Harmanny, and J. J. M. de Wit, "Classification of small UAVs and birds by micro-Doppler signatures," 10th European Radar Conference. IEEE, October 2013.
- [101] J. Zabalza, C. Clemente, and G. D. Caterina, "Robust PCA micro-Doppler classification using SVM on embedded systems," *IEEE Transactions on Aerospace and Electronic Systems*, vol. 50, no. 3, pp. 2304–2312, July 2014.
- [102] J. J. M. de Wit, R. I. A. Harmanny, and P. Molchanov, "Radar micro-Doppler feature extraction using the singular value decomposition," IEEE Radar Conference. IEEE, 2014.
- [103] B. P. Bogert, M. J. R. Healy, and J. W. Tukey, "The quefrequency analysis of time series for echoes: Cepstrum, pseudo autocovariance, cross-cepstrum and saphe cracking," in *1963 Symposium on Time Series Analysis*, no. 5, 1963, pp. 209–243.
- [104] R. I. A. Harmanny, J. J. M. de Wit, and G. P. Cabic, "Radar micro-Doppler feature extraction using the spectrogram and the cepstrogram," in *2014 11th European Radar Conference*, Oct 2014, pp. 165–168.
- [105] A. Brewster and A. Balleri, "Extraction and analysis of micro-Doppler signatures by the empirical mode decomposition," IEEE Radar Conference. IEEE, 2015.
- [106] B. Oh, X. Guo, F. Wan, K. Toh, and Z. Lin, "Micro-Doppler mini-UAV classification using empirical-mode decomposition features," *IEEE Geoscience and Remote Sensing Letters*, vol. 15, no. 2, pp. 227–231, Feb 2018.
- [107] —, "An EMD-based micro-Doppler signature analysis for mini-UAV blade flash reconstruction," in *2017 22nd International Conference on Digital Signal Processing (DSP)*, Aug 2017, pp. 1–5.
- [108] Y. Zhao and Y. Su, "Cyclostationary phase analysis on micro-Doppler parameters for radar-based small UAVs detection," *IEEE Transactions on Instrumentation and Measurement*, vol. 67, no. 9, pp. 2048–2057, Sept 2018.

- [109] S. H. Darwish, M. A. El-latif, and M. Morsy, “Micro-Doppler detection and target identification using artificial neural network,” in *2012 IEEE Aerospace Conference*, March 2012, pp. 1–5.
- [110] J. Martinez, D. Kopyto, M. Schütz, and M. Vossiek, “Convolutional neural network assisted detection and localization of UAVs with a narrowband multi-site radar,” in *2018 IEEE MTT-S International Conference on Microwaves for Intelligent Mobility (ICMIM)*, April 2018, pp. 1–4.
- [111] G. J. Mendis, T. Randeny, J. Wei, and A. Madanayake, “Deep learning based Doppler radar for micro UAS detection and classification,” in *MILCOM 2016 - 2016 IEEE Military Communications Conference*, Nov 2016, pp. 924–929.
- [112] M. R. Bell, “Information theory and radar waveform design,” *IEEE Transactions on Information Theory*, vol. 39, no. 5, pp. 1578–1597, Sept 1993.
- [113] J. R. Guerci and S. U. Pillai, “Theory and application of optimum transmit-receive radar,” in *Record of the IEEE 2000 International Radar Conference [Cat. No. 00CH37037]*, May 2000, pp. 705–710.
- [114] M. S. Greco, F. Gini, P. Stinco, and K. Bell, “Cognitive radars: On the road to reality: Progress thus far and possibilities for the future,” *IEEE Signal Processing Magazine*, vol. 35, no. 4, pp. 112–125, July 2018.
- [115] K. L. Bell, C. J. Baker, G. E. Smith, J. T. Johnson, and M. Rangaswamy, “Cognitive radar framework for target detection and tracking,” *IEEE Journal of Selected Topics in Signal Processing*, vol. 9, no. 8, pp. 1427–1439, Dec 2015.
- [116] —, “Fully adaptive radar for target tracking part I: Single target tracking,” in *2014 IEEE Radar Conference*, May 2014, pp. 0303–0308.
- [117] —, “Fully adaptive radar for target tracking part II: Target detection and track initiation,” in *2014 IEEE Radar Conference*, May 2014, pp. 0309–0314.
- [118] A. E. Mitchell, G. E. Smith, K. L. Bell, and M. Rangaswamy, “Coordinate descent for cognitive radar adaptation,” in *2016 CIE International Conference on Radar (RADAR)*, Oct 2016, pp. 1–5.

- [119] —, “Single target tracking with distributed cognitive radar,” in *2017 IEEE Radar Conference (RadarConf)*, May 2017, pp. 0285–0288.
- [120] A. S. Butterfield, A. E. Mitchell, G. E. Smith, K. L. Bell, and M. Rangaswamy, “Metrics for quantifying cognitive radar performance,” in *2016 CIE International Conference on Radar (RADAR)*, Oct 2016, pp. 1–4.
- [121] G. E. Smith, Z. Cammenga, A. Mitchell, K. L. Bell, J. Johnson, M. Rangaswamy, and C. Baker, “Experiments with cognitive radar,” *IEEE Aerospace and Electronic Systems Magazine*, vol. 31, no. 12, pp. 34–46, December 2016.
- [122] K. L. Bell, J. T. Johnson, G. E. Smith, C. J. Baker, and M. Rangaswamy, “Cognitive radar for target tracking using a software defined radar system,” in *2015 IEEE Radar Conference (RadarCon)*, May 2015, pp. 1394–1399.
- [123] A. Department, *Electronic Warfare and Radar Systems Engineering Handbook*. Naval Air Warfare Center Weapons Division, Point Mugu, 2013.
- [124] “IEEE standard letter designations for radar-frequency bands,” *IEEE Std 521-2002*, pp. 1–3, 2003.
- [125] E. Koelink, *Scattering Theory*, Radboud Universiteit, Spring 2008.
- [126] C. A. Balanis, *Antenna Theory: Analysis and Design*. New York, NY: Wiley-Interscience, 2005.
- [127] A. Schroder, M. Renker, U. Aulenbacher, A. Murk, U. Boniger, R. Oechslin, and P. Wellig, “Numerical and experimental radar cross section analysis of the quadrocopter DJI Phantom 2,” in *2015 IEEE Radar Conference*, Oct 2015, pp. 463–468.
- [128] S. Kim, S. J. Lee, J. H. Jung, and Y. Kim, “Radar cross section measurements of quadcopters using long term evolution frequency,” in *2017 IEEE Asia Pacific Microwave Conference (APMC)*, Nov 2017, pp. 1294–1297.
- [129] S. Pisa, E. Piuzzi, E. Pittella, P. Lombardo, N. Ustalli, W. Cao, D. Bloisi, D. Nardi, P. D’Atanasio, and A. Zambotti, “Evaluating the radar cross section

of the commercial IRIS drone for anti-drone passive radar source selection,” in *2018 22nd International Microwave and Radar Conference (MIKON)*, May 2018, pp. 699–703.

- [130] S. Rzewuski, K. Kulpa, B. Salski, P. Kopyt, K. Borowiec, M. Malanowski, and P. Samczyński, “Drone RCS estimation using simple experimental measurement in the WIFI bands,” in *2018 22nd International Microwave and Radar Conference (MIKON)*, May 2018, pp. 695–698.
- [131] (2018) About GNU Radio. GNU Radio. [Online]. Available: <https://www.gnuradio.org/about/>
- [132] R. Buder, *The Invention That Changed the World: How a Small Group of Radar Pioneers Won the Second World War and Launched a Technical Revolution*. Touchstone, 1997.
- [133] T. Long, Y. Wang, and T. Zeng, “Signal-to-noise ratio in stretch processing,” *Electronics Letters*, vol. 46, no. 10, pp. 720–722, May 2010.
- [134] (2018) Empro 3d em simulation software. Keysight Technologies. [Online]. Available: <https://www.keysight.com/en/pc-1297143/empro-3d-em-simulation-software?cc=US&lc=eng>
- [135] (2018) Advanced Design System (ADS). Keysight Technologies. [Online]. Available: <https://www.keysight.com/en/pc-1297113/advanced-design-system-ads>
- [136] (2018) Genesys RF/Microwave Synthesis and Simulation Software. Keysight Technologies. [Online]. Available: <https://www.keysight.com/en/pc-1297125/genesys-rf-and-microwave-design-software?cc=US&lc=eng>
- [137] (2018) Mini-Circuits (homepage). Mini-Circuits. [Online]. Available: <https://www.minicircuits.com/>
- [138] (2018) RTL-SDR home page. RTL-SDR. [Online]. Available: <https://www.rtl-sdr.com/about-rtl-sdr/>

- [139] (2018) Wideband Transceivers. Analog Devices, Inc. [Online]. Available: <https://www.analog.com/en/applications/technology/sdr-radioverse-pavilion-home/wideband-transceivers.html>
- [140] (2018) Ettus Research, an NI Brand. Ettus Research. [Online]. Available: <https://www.ettus.com/>
- [141] (2018) LMS7002M. online. Lime Microsystems. [Online]. Available: <https://limemicro.com/technology/lms7002m/>
- [142] (2018) LimeSDR. MyriadRF. [Online]. Available: <https://myriadrf.org/projects/limesdr/>
- [143] (2018) LimeSuite. MyriadRF. [Online]. Available: <https://github.com/myriadrf/LimeSuite>
- [144] (2018) Soapysdr. Pothosware. [Online]. Available: <https://github.com/pothosware/SoapySDR>
- [145] (2018) GNU Radio Radar Toolbox. Kit-Cel. [Online]. Available: <https://github.com/kit-cel/gr-radar>
- [146] A. E. Fuhs, *Radar Cross Section Lectures*, Naval Postgraduate School, March 1983.
- [147] “Radio Frequency Devices,” Title 47 CFR 15, Federal Communications Commission, 2004,
https://www.ecfr.gov/cgi-bin/text-idx?SID=2ddc98dc387c291baaf407452e4d1c72&mc=true&node=pt47.1.15&rgn=div5#_top.
- [148] E. Moore. (2018) Radar UAV SAA LIME. [Online]. Available: https://github.com/Audioholic11/RADAR_UAV_SAA_LIME
- [149] A. Melzer, A. Onic, F. Starzer, and M. Huemer, “Short-range leakage cancellation in FMCW radar transceivers using an artificial on-chip target,” *IEEE Journal of Selected Topics in Signal Processing*, vol. 9, no. 8, pp. 1650–1660, Dec 2015.

- [150] M. Pehlivan and K. Yegin, "Self-jamming and interference cancellation techniques for continuous wave bi-static radar systems," in *2018 22nd International Microwave and Radar Conference (MIKON)*, May 2018, pp. 255–257.
- [151] A. Hassaniien and S. A. Vorobyov, "Phased-MIMO radar: A tradeoff between phased-array and MIMO radars," *IEEE Transactions on Signal Processing*, vol. 58, no. 6, pp. 3137–3151, June 2010.
- [152] Y. Qu, G. S. Liao, S. Q. Zhu, X. Y. Liu, and H. Jiao, "Performance comparisons of MIMO and phased-array radar," in *MIKON 2008 - 17th International Conference on Microwaves, Radar and Wireless Communications*, May 2008, pp. 1–4.
- [153] *Radio Frequency Integrated Circuits and Technologies*. Springer-Verlag Berlin Heidelberg, 2008, ch. 2 Transceiver Architectures.
- [154] M. Chaplin. (2018) Water structure and science. [Online]. Available: http://www1.lsbu.ac.uk/water/microwave_water.html

Appendix A

Radar Basics

A.1 Radar Types

Radars are often distinguished by their inherent measurement capabilities. At a fundamental level, the sensor is capable of estimating range and/or velocity. The capabilities are often referred to by the radar's action rather than measurement. For range measurements, a pulsed radar is required. For velocity measurements, a Doppler radar is required. The following section first isolates each capability and overviews the required systems. Subsequently, methods and limitations of combining both capabilities into one system are introduced.

A.1.1 Pulsed

The first pulsed radar systems used short-time, high-power pulses at one constant wavelength. When and if the pulse returns, a detection and distance estimate can be made by the radar system. The whole system spun on a large mechanical servo to “sweep” a field of view by taking successive azimuthal measurements. A pulse consists of a carrier transmit frequency enveloped or multiplied by a square wave with low duty cycle as shown in Figure A.1.

The pulse width τ repeats every pulse period T_r seconds with a pulse repetition frequency $f_r = 1/T_r Hz$. The detected signal contains transmitter leakage and the superposition of the target return signal and unwanted reflections from all

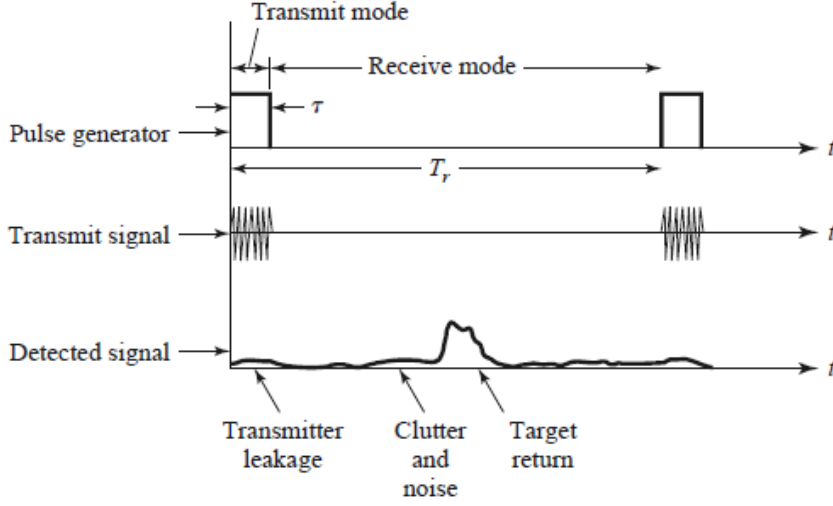


Figure A.1: Radar pulse signal with return signal [41]

objects within the scene. The range of a target can be calculated by the time difference between transmit mode and the return signal via equation 2.1. The range can be calculated by the cross-correlation between send and return signals. The range resolution is limited by $1/\tau$ which determines the main lobe width of a cross correlation between two pulses. The minimum range is determined when a full pulse can be received (equation A.1). The maximum ambiguous range is determined by T_r . If the target return signal occurs after T_r , it is unknown from which transmit pulse the signal originated. In this way, the range is ambiguous above R_{amb} calculated in equation A.2.

$$R_{min} = \frac{c\tau}{2} \quad m \quad (\text{A.1})$$

$$R_{amb} = \frac{cT_r}{2} \quad m \quad (\text{A.2})$$

From the radar range equation 2.13, the received noise power is inversely proportional to R^4 . For a given target RCS, Figure A.2 shows the minimum, maximum and ambiguous range. R_{min} and R_{amb} are determined by the pulse waveform. R_{max} is determined by the radar range equation 2.13. Typically R_{amb} is set to just after R_{max} to hide any ambiguous return signal in the noise of the

system, thus limiting the acquisition time of the system. The range between R_{min} and R_{max} is called the *Range Swath* and can be increased by increasing transmit power, antenna gain or target RCS.

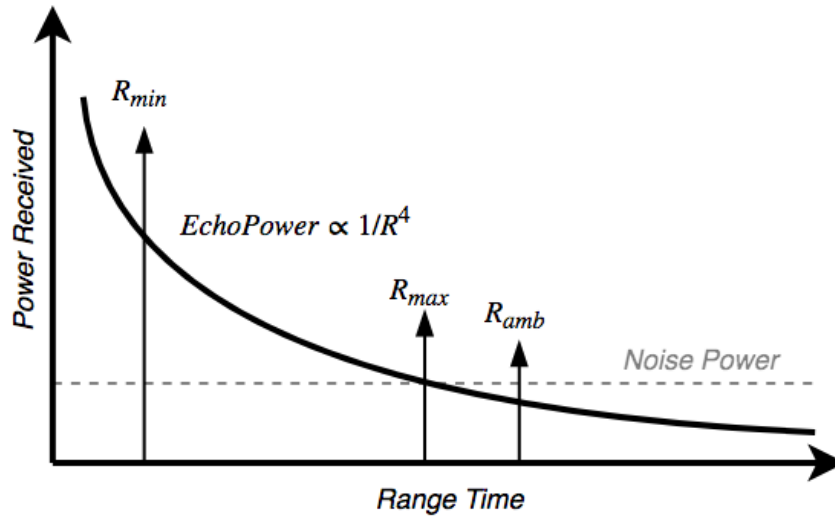


Figure A.2: Radar range swath

Figure A.3 gives an example of a range-only pulse radar block diagram. The radar waveform is modulated onto the transmit signal by *duplexing* a single antenna with a microwave switch, effectively transitioning the radar between transmit and receive mode. The transmit frequency f_0 is modulated out of the return signal leaving the radar return signal only. The resulting signal is amplified, peak detected, and displayed.

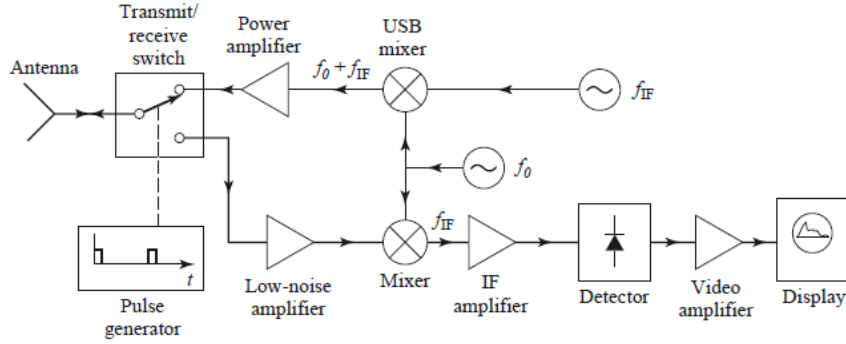


Figure A.3: Pulse radar block diagram [41]

A.1.2 Doppler

From a radar operator's standpoint, having a direct velocity measurement is desired for more accurate tracking. A pulsed radar can also be capable of calculating the target velocity with additional circuits and components via the Doppler Effect. The Doppler Effect was first described in 1842 by physicist Christian Doppler. The effect changes the observed frequency of a wave originating at a source by the receiver's relative velocity and is a property of all propagating waves including sound, water and EM. The relationship between the observed frequency f and the emitted frequency f_0 is given in equation A.3 [10].

$$f = f_0 \left(\frac{c \pm v_r}{c \mp v_s} \right) \quad (\text{A.3})$$

Setting the source velocity to zero ($v_s = 0$) and assuming the receiver velocity v_r is small compared to c , the relative velocity, $\Delta v = v_r - v_s$, is shown in the Doppler relationship equation A.4. A positive relative velocity results from source and receiver moving away from each other.

$$f = f_0 \left(1 + \frac{\Delta v}{c} \right) \quad (\text{A.4})$$

The change in frequency due to the Doppler Effect, $\Delta f = f - f_0$, is shown in equation A.5. In this way the observed Doppler Effect induced frequency shift or

Doppler Shift is determined by the relative velocity scaled by the wavelength of the transmitted frequency.

$$\Delta f = -f_0 \frac{\Delta v}{c} = -\frac{\Delta v}{\lambda} \quad (\text{A.5})$$

EM waves do not propagate in a medium like sound or water waves. The constant velocity of light c is seen from both the source and observer and thus the relative velocity must account for special relativity effects through Lorentz transformations. More specifically, a time dilation factor (equation A.6) stretches or compresses the time length between crests of an EM wave (equation A.7).

$$\gamma = \frac{1}{\sqrt{1 - \frac{v_s^2}{c^2}}} \quad (\text{A.6})$$

$$\Delta t_s = t_2 - t_1 = \frac{\gamma}{f_0} \quad (\text{A.7})$$

The Doppler shift equation A.3 becomes equation A.8 which can be written in terms of $\beta = \frac{v}{c}$. If $v \ll c$ relativistic effects become negligible as $\gamma \rightarrow 1$, $\Delta t_s \rightarrow \frac{1}{f_0}$ and equation A.8 \rightarrow equation A.3 [10].

$$f = \frac{f_0}{\gamma} \left(\frac{c \pm v_r}{c \mp v_s} \right) = f_0 \sqrt{\frac{1 \pm \beta}{1 \mp \beta}} \quad (\text{A.8})$$

This can also be seen via the MacLaurin series when $\beta \rightarrow 0$ and higher order terms cancel out...

$$\sqrt{\frac{1 - \beta}{1 + \beta}} = 1 - \beta + \frac{\beta^2}{2} - \dots \quad (\text{A.9})$$

The Doppler shift when source and observer are moving away from each other at relatively low speeds is...

$$f \cong f_0 (1 - \beta) = f_0 \left(1 - \frac{v}{c} \right) \quad (\text{A.10})$$

This is approximately equal to equation A.4 or the classical interpretation of the Doppler effect and thus the Doppler shift for all relatively low speed interactions can

be calculated via equation A.5. To keep terms consistent, positive Δv represents the observer traveling away from the source and thus imparting a negative frequency shift or longer wavelength shift onto the signal.

$$f_{Doppler} \cong \Delta f = -\frac{\Delta v}{\lambda} \quad (\text{A.11})$$

For radar applications the relative speed of the aircraft is assumed to be much less than the speed of light. Figure A.4 is a diagram representing the Doppler effect in radars. The transmitter emits a wave with frequency f_{tx} in the general direction of a target with an RCS σ . The target has a velocity and direction represented by vector v . The Doppler circles in the background are the two dimensional frequency shifts from each source direction observed by a target traveling at velocity v . The projected velocity or relative velocity between transmitter and target $\Delta v = v \cos \theta$ imparts a frequency shift Δf_D onto the reflection of the wave. From equation A.11 the Doppler shift is based on the relative velocity Δv and wavelength λ . Thus, the scattered wave has a frequency $f_{tx} + \Delta f_D$. The scattering signal captured by the radar experiences another Doppler shift of $\frac{\Delta v}{\lambda}$ as the source becomes the target and the observers becomes the receiver of the radar system. The total frequency shift in a monostatic Doppler radar is then $f_{Dr} = \frac{2\Delta v}{\lambda}$. Notice that the negative sign from the velocity term cancels the negative sign in equation A.11 and thus increases the frequency or decreases the wavelength.

Figure A.5 contour plots the Doppler shift in a monostatic radar system for microwave frequencies up to 30 GHz and over ± 100 m/s. FCC Part 107 dealing with small commercial UASs gives a velocity limit of 100 mph or 45 m/s. This gives a maximum relative speed of 90 m/s between two Part 107 UAVs going opposite directions. At S-Band, the Doppler shift for UAVs is between ± 2 kHz. At X-band, the Doppler shift is ± 6 kHz. At K-Band, it is ± 15 kHz. In order to measure the full Doppler shift, the PRF f_τ or the sample rate of the Doppler processor must be larger than $2 \times f_{DopplerMax}$ to prevent Doppler ambiguities from sample aliasing. The Doppler resolution is limited by the frequency resolution of the FFT of a coherent acquisition window. From basic signal processing theory, the longer acquisition window yields a more resolved main lobe in the frequency domain. Applying windows can also effect the main lobe width of the FFT.

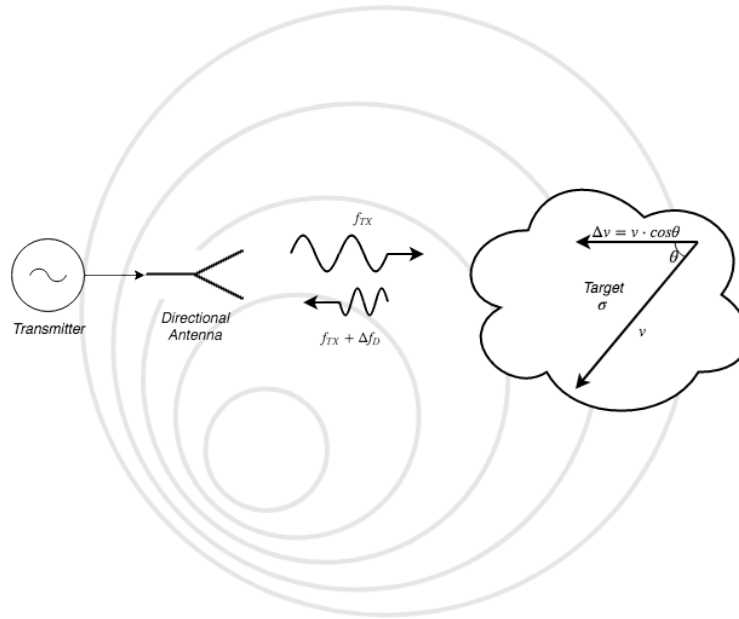


Figure A.4: Radar doppler effect: $f_{Dr} = \frac{2\Delta v}{\lambda}$

A simplified functional block diagram of a Doppler (velocity) only radar system is shown in Figure A.6. The *circulator* only allows microwave energy entering a certain port to travel to the port in the counter-clockwise direction. The Doppler shift f_d is demodulated out of the return signal and pre-processed for the display. The transmitted signal is a continuous frequency and does not have modulation applied to it. This is commonly called a Continuous Wave or “CW” signal and CW radar.

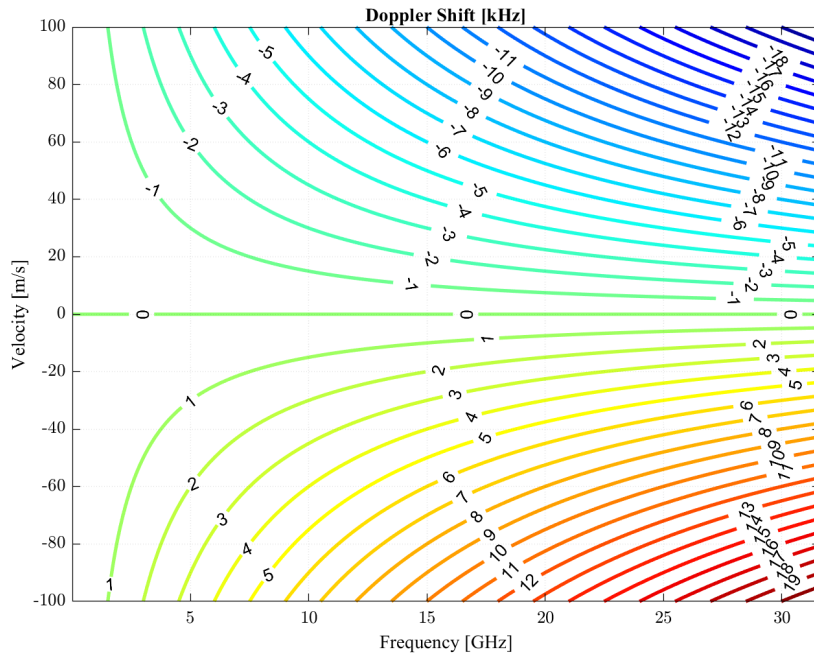


Figure A.5: Doppler shift in radar

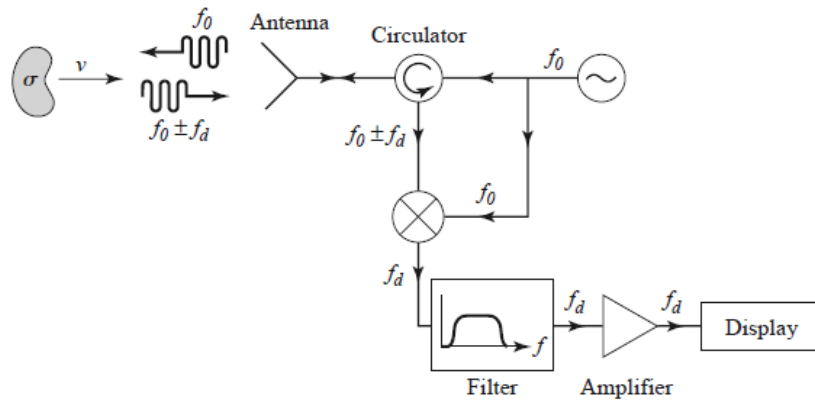


Figure A.6: Doppler radar block diagram [41]

A.1.3 Pulse-Doppler

Combining pulse and Doppler radars to estimate range and velocity within the same system was enabled by high-data sampling and fast computation, using the radar architecture in figure 2.11 with a pulsed radar waveform. A single range

measurement is made every PRI. The measurement contains inherent ambiguities and resolution limitations. The method to estimate the range is explained in the following sections. The range measurement is considered to occur in the “fast time” because the estimate is processed and further limited by the fundamental data sample rate of the system f_{samp} . In a CW system, the velocity or Doppler processing occurs in the “fast time”. If the system is coherent across pulses, CPI can be performed by using information of a single, similar sample from successive pulses. Using one sample from each pulse reduces the effective sample rate and is thus the origin for the nomenclature “slow time.”

The inherent temporal behavior of range and Doppler mechanisms lead to the effectiveness of CPI processing range in the fast time and Doppler in slow time. A range requires differentiating propagating signals traveling at the speed of light. As a baseline, light in a vacuum takes 3.33 ns to travel 1 m . Sampling a passing EM wave at 300 MHz will capture the wave at 1 m increments. From the preceding section, the target Doppler shifts for typical UASs at common radar bands are within the kHz range, thus Doppler processing occurs in the slow time. Figure A.7 shows a two-dimensional data matrix which represents each complex data sample organized along the fast time and slow time dimensions. The vertical fast time dimension represents each data sample within one pulse or the discrete range bins within the range swath. The horizontal slow time dimension represents the same range bin across multiple pulses occurring at the PRI. Digital filters and further processing in each direction can either isolate targets at constant range or constant velocity. For example, if the Doppler shift is required, the spectral analysis of a single range bin across the slow time results in an estimate of the target’s velocity only at a specific range. Applying a high-pass filter across the slow time removes stationary objects which is often desired when removing ground clutter.

The PRI or PRF ($PRF = 1/PRI = 1/T_r$) affects ambiguity of both range and velocity measurements. For a given PRF, the unambiguous range R_{un} and velocity v_{un} are shown in equations A.12 and A.13. The unambiguous range is inversely related to the PRF while the unambiguous velocity is directly related. Therefore,

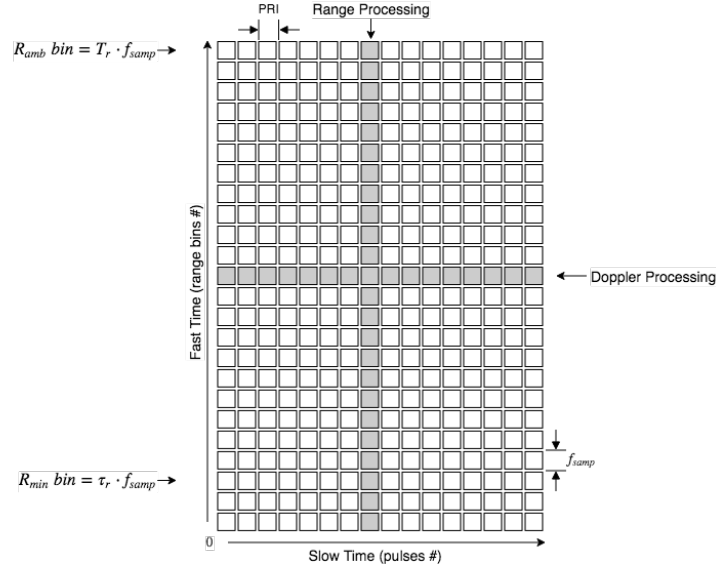


Figure A.7: Fast time, slow time 2D radar processing data matrix

the PRF trades range coverage for velocity coverage. The relationship is known as the *Range-Doppler Dilemma*.

$$R_{un} = \frac{c}{2PRF} \quad (\text{A.12})$$

$$v_{un} = \frac{\lambda PRF}{2} \quad (\text{A.13})$$

The combined unambiguous coverage or total range-Doppler coverage is constant and does not depend on PRF but does depend on the transmit wavelength (equation A.14). As the operating frequency increases, the coverage decreases. Figure A.8 shows the maximum unambiguous range vs. maximum unambiguous velocity as a function of operating frequency in GHz . To move along the operating frequency contours, the operator must only change the PRF. The higher the PRF, the lower the range.

$$R_{um}v_{um} = \frac{\lambda c}{4} \quad (\text{A.14})$$

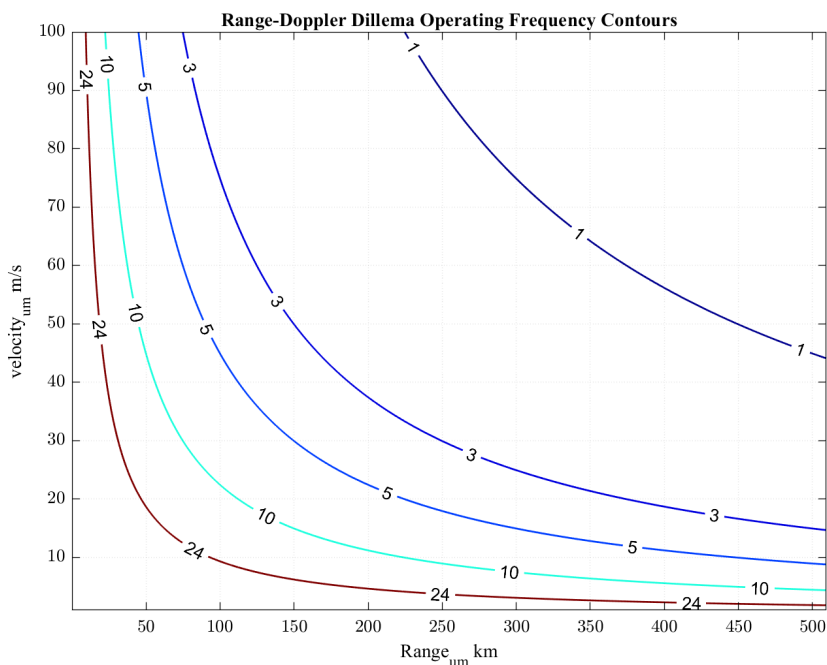


Figure A.8: Maximum unambiguous range vs. velocity at operating frequency in GHz.

A.2 Radar Signal Processing

RSP is the method or algorithms by which the sampled signals are processed to calculate range and/or velocity estimates. RSP algorithms are typically designed from fundamental mathematical models with careful consideration for radar types, desired targets, environmental noise and hardware limitations. The following sections provide an introduction to the common, fundamental topics of RSP. A more expansive overview can be found in [30].

A.2.1 Matched Filter

From a signal processing perspective, the goal is to maximize the SNR and measure the time difference between send and receive signals. Any increase in SNR due to signal processing techniques can be captured in a signal processing gain factor G_s . A common and well-established filter technique call *Matched Filtering* is used to

maximize output SNR [30]. The matched filter (equation A.15) is the time-reversed, scaled, complex conjugate of the input signal $x(t)$. T_M is an arbitrary time shift. α is an arbitrary scale factor which has no effect on output SNR.

$$\begin{aligned} h(t) &= \alpha x^*(T_M - t) \quad \text{or} \\ H(\omega) &= \alpha X^*(\omega) e^{-j\omega T_m} \end{aligned} \tag{A.15}$$

To get a better intuition as to the effect of a matched filter, equation A.16 shows the output $y(t)$ of the matched filter applied or convolved with $x'(t)$. The output is seen to be the cross-correlation between the signal plus noise and the matched filter with a time shift T_m . If $x(t)$ is a pulse, the cross-correlation between input and shifted output results in a triangle function centered around the shift. The peak of the triangle is an SNR-optimized estimate of the time shift T_m . This is ideal for radar range finding.

$$h(t) = \alpha \int_{-\infty}^{\infty} x'(s) h(t - s) ds = \alpha \int_{-\infty}^{\infty} x'(s) x^*(s + T_M - t) ds \tag{A.16}$$

Figure A.9 shows the signal processing chain for a matched filter range detector. The input $x(t)$ is simply a pulse. The Matched filter $H(\omega)$ is calculated and applied to the input signal plus noise, plus an ideal target model. The noise N is a function of radar direction and system NF. The target model includes an attenuation factor σ and the time delay t_0 . Setting $T_m = \tau$ the output is now the same cross-correlated triangle from equation A.16 but now time shifted $t_0 + \tau$. A simple peak detector can now estimate the time shift \hat{t}_0 and calculate the range of the target. The range resolution ΔR or ability for the estimator to distinguish two targets close to each other is determined by the pulse duration in terms of range.

$$\Delta R = \frac{c\tau}{2} \tag{A.17}$$

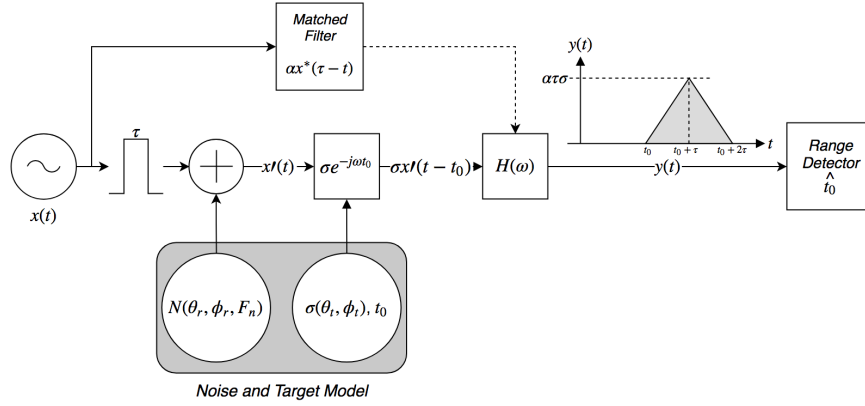


Figure A.9: Matched filter signal processing chain

A.2.2 Ambiguity Function

The ideal target model excludes the effects of Doppler shift which may occur if the target has a relative velocity. Incorporating a Doppler-shifted $e^{j2\pi f_d t}$ applied to the signal $x(t)$ and assuming $\alpha = 1$ and $T_m = 0$ leads to an important radar waveform design tool called Ambiguity Function (AF) $A(t, f_d)$. The function, as defined in equation A.18, is often depicted as a 2-dimensional plane with a maximum at $(0, 0)$. It represents the cross-correlation response of an input function in both time and Doppler shift. Figure A.9 is a contour plot of a pulse AF with $\tau = 1\mu s$ and $T_m = 10\mu s$.

$$A(t, f_d) = \left\| \hat{A}(t, f_d) \right\| = \left\| \int_{-\infty}^{\infty} x(s) e^{j2\pi f_d s} x^*(s - t) ds \right\| \quad (\text{A.18})$$

Figures A.11 and A.12 show $\tau = 0$ and $0Hz$ Doppler and Delay cut, respectively. The resolution of a Doppler shift or range estimate can be seen as the ability to differentiate the main lobe from a shifted main lobe.

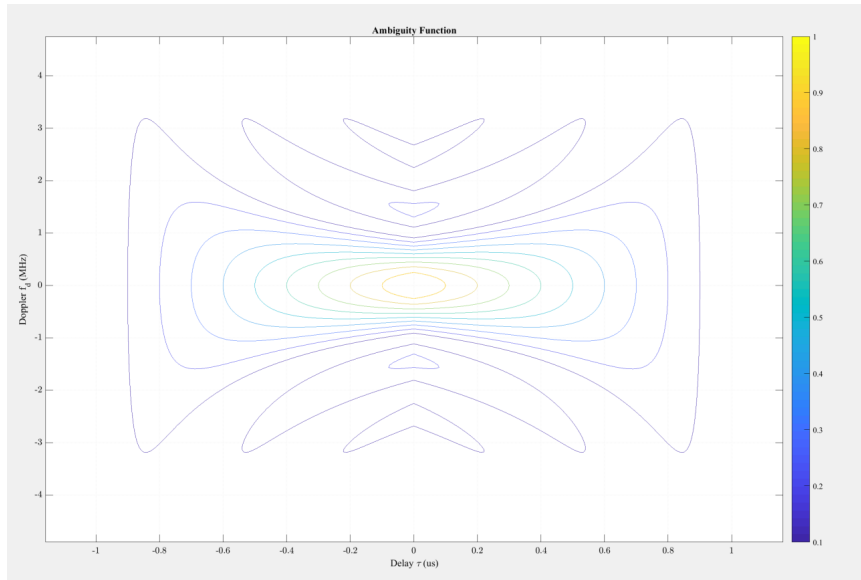


Figure A.10: Pulse ambiguity function

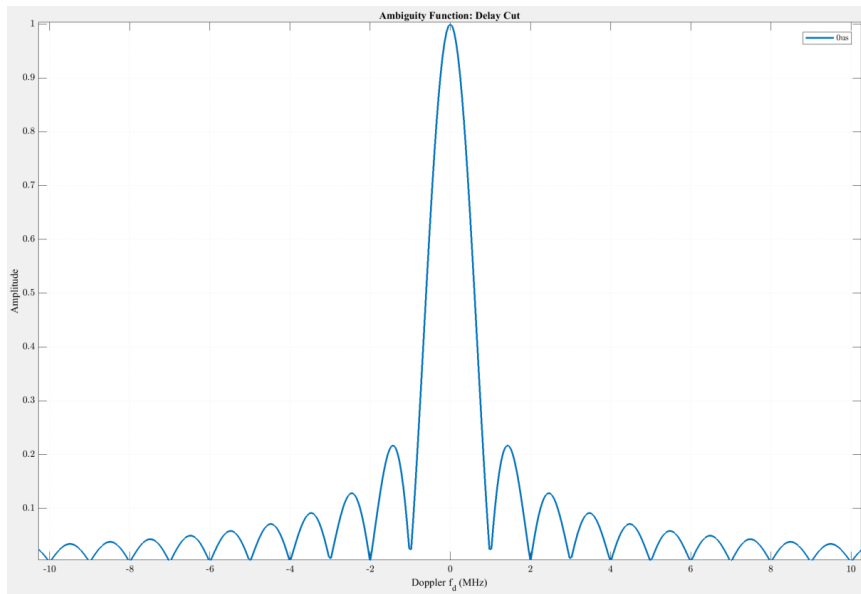


Figure A.11: Pulse ambiguity function delay cut

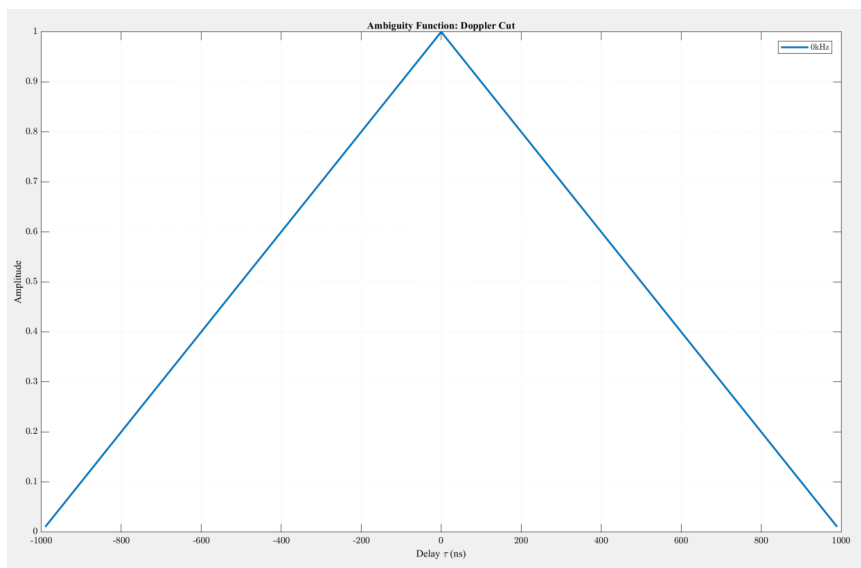


Figure A.12: Pulse ambiguity function doppler cut

A.2.3 Pulse Compression

Both Pulse and Doppler radar's performance is limited by hardware speed and power handling. Peak and average power limit the maximum range which can be seen in the radar range equation 2.6. Typically, a high power handling amplifier is placed before the transmit antenna. If the amplifier is driven to high peak powers, the output becomes saturated and power is lost to the harmonics of the transmit frequency. The duty cycle $\frac{\tau}{T_m}$ relates the peak to average transmit power. High average powers can lead to power loss to heat and thus reduce power efficiency.

The range resolution and signal detection are effected by hardware power limitations. For pulse radar, the range resolution ΔR is directly related to the pulse width τ through equation A.17 and thus a smaller pulse width is required for better range resolution. For signal detection, the SNR χ of the return signal can be written in the energy form equation A.19 where the noise is modeled as a zero-mean white Gaussian noise with variance σ_n .

$$\chi = \frac{E_s}{\sigma_n} \quad (\text{A.19})$$

The total signal energy E_s of a data acquisition time T_m is the received instantaneous power $P_s(t)$ integrated over the entire time period. For a reflected pulse waveform $x(t)$ with a peak voltage level A from propagation attenuation, RCS and system losses K , the power is related to $x^2(t)$. Therefore, $P_s(t) = x^2(t) = K^2 A^2(t)$ for $t = 0$ to $t = \tau$.

$$E_s = \int_0^{T_m} P_s(t) dt = \int_0^{\tau} K^2 A^2 dt = K^2 A^2 \tau \quad (\text{A.20})$$

The SNR is also directly related to τ . This presents an inverse relationship between smaller range resolution and larger SNR. To maintain a required SNR, decreasing τ requires increased peak power. Therefore the hardware power limitations require a minimum τ in order to detect a signal at a given SNR. Since the signal's SNR decreases as range increases via the inverse square law, the radar engineer must choose τ to increase range resolution or maximum range of detection.

The idea of pulse compression was theorized in order to decouple SNR or energy from resolution for a given range of targets. In order to decouple, the range resolution must be further investigated. The range resolution is fundamentally determined by an internal time resolution which can be interpreted as the ability for a system to sense changes in time or time derivatives. One measure of a system's ability to transfer higher time derivatives in steady state is commonly called bandwidth. Intuitively, a zero-mean, sinusoidal signal with higher frequency ultimately requires larger slopes at the zero crossings or a system with a larger bandwidth allows higher time derivatives to pass through. The FFT of a pulse width τ is known to be a sinc function with main lobe peak-to-null bandwidth $\beta_p = \frac{1}{\tau}$. β_p can be thought of as the minimum bandwidth or minimum resolution of any signal of length τ . To increase the time resolution, the pulse is modulated by a known signal with higher bandwidth β_m thus decoupling bandwidth and time-width by a known factor. The TBP is a measure of bandwidth increase or time-resolution increase from the simple pulse minimum. For a simple pulse, the TBP is equal to 1. As $\beta_m \gg \beta_p$, the pulse energy is compressed across more bandwidth by a factor of TBP thus maintaining detection performance while improving range resolution.

Common modulation waveforms include linear or non-linear frequency, stepped frequency and binary phase. LFM is one of the most commonly used, simple, and understood functions. It is defined as a linear sweep of some bandwidth β_{LFM} over the pulse width τ .

$$x(t) = \cos\left(\pi \frac{\beta_{LFM}}{\tau} t^2\right) \quad (\text{A.21})$$

Ideally, the waveform contains equal energy at all frequencies across the bandwidth and is commonly called an up-chirp or down-chirp signal depending on the ramp direction due to the sound it makes when played back within the audio range. Figure A.13 shows the real and imaginary parts of a chirp waveform with a length of $1\mu s$ with a TBP of 50.

Processing the LFM waveform with $TBP = 10$ through a matched filter, Figure A.14 is the AF and Figure A.15 is the zero Doppler cut or auto-correlation. The LFM waveform appears to rotate the AF from the simple pulse so constant

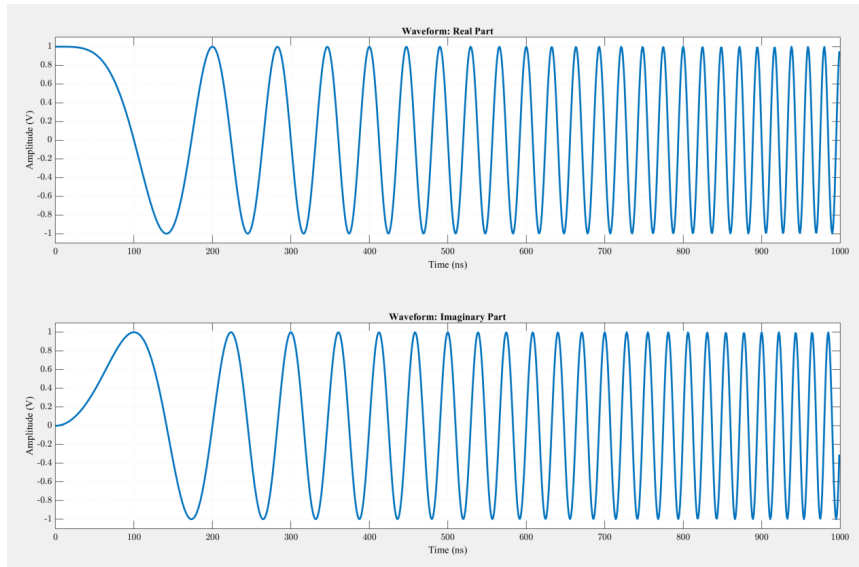


Figure A.13: Linear Frequency Modulated Waveform of length $1\mu s$ and $TBP = 50$

Doppler cuts will cross the main lobe at a diagonal and therefore decrease the main lobe of the constant Doppler cut. The zero-delay cut will remain similar to a simple pulse; however, the range and velocity are now coupled when the Doppler frequency shift is similar to $\frac{2R}{c} \frac{\beta}{\tau} Hz$ or the target reflection occurs along the AF diagonal.

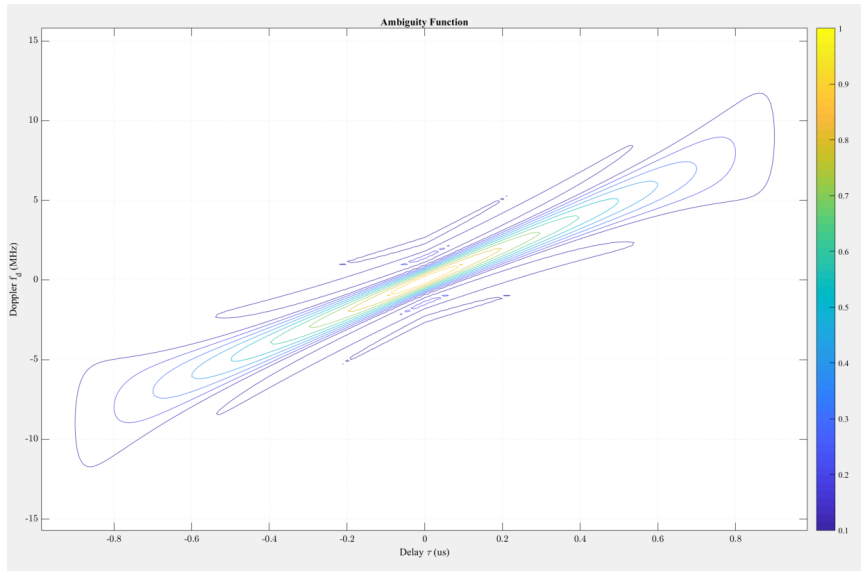


Figure A.14: Ambiguity Function of LFM Waveform of length $1\mu s$ and $TBP = 10$

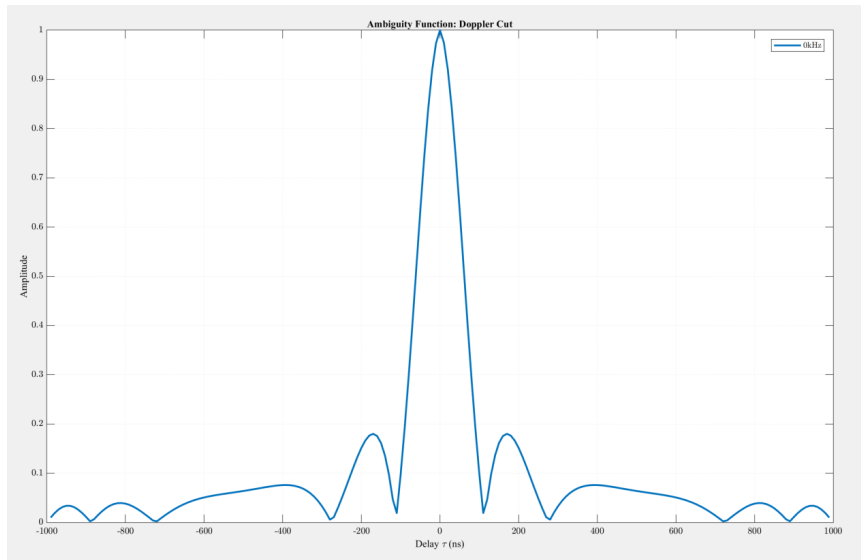


Figure A.15: Doppler cut of the Ambiguity Function of LFM Waveform of length $1\mu s$ and $TBP = 10$

A.2.4 Frequency Modulated Continuous Wave

FMCW radar is arguably the most common radar technique at the time of this thesis. It involves a repeated LFM transmit signal with a duty cycle near 100%. The chirp signal can be linearly increasing, decreasing, or both in frequency for some bandwidth (usually about $500MHz$). FMCW is ideal for accurate, close-range tracking. The bandwidth in a radar system ultimately determines the range resolution and nominal ranges. FMCW provides higher average power from near 100% duty cycle. This yields higher SNR at greater distances or smaller RCS. Thus making FMCW a good candidate for accurate range detection of small targets within the close range.

Appendix B

Software Defined Radios

B.1 Mixed Signal Limitations

Current ADCs and Digital-to-Analog Converters (DACs) have limited upper sample frequency ranges determined by the physical speed of electronics. The Nyquist frequency is defined as half the sample rate or the maximum frequency a sampling process can recreate without aliasing. As a rule of thumb, a usable sampling process must be at least 5-10 times higher than operating bandwidth. Typical high-end ADCs/DACs have sampling frequencies less than $500MHz$ thus limiting potential operating bandwidths.

The use of a single data converter per transmit or receive channel further limits temporal or phase measurements to be made across channels. For MIMO, fully coherent information across all channels is required for physical layer time synchronicity. “Fully Coherent” implies both in-phase and quadrature (90° out of phase) signals are sampled or created. Thus, both amplitude and phase of the signal is monitored.

B.2 Frequency Conversion

Due to EM propagation behavior, common communication frequency bands range from a few MHz to a few GHz . Short-range communications are also being devel-

oped up to 100 GHz at the time of this thesis. Given the limitation of ADCs/DACs, RF frontends have been conceived and developed to convert limited frequency bands from the propagation frequency to near 0 Hz or “DC” while maintaining the integrity of the information signal. To achieve this, components are developed to “mix” or multiply two signals together. The result is a signal whose frequency is a combination of the sum and difference of the original signal’s frequencies. This behavior is easily seen in the “Product-to-Sum” and “Sum-to-Product” trigonometric identities in equations B.1 and B.2.

$$\cos \theta \cdot \cos \phi = \frac{\cos(\theta + \phi)}{2} + \frac{\cos(\theta - \phi)}{2} \quad (\text{B.1})$$

$$\cos \theta + \cos \phi = 2 \cdot \cos\left(\frac{\theta \pm \phi}{2}\right) \cdot \cos\left(\frac{\theta \mp \phi}{2}\right) \quad (\text{B.2})$$

B.3 Frontend Architecture

The sampled or constructed signal is centered around the IF. The IF is converted to or from the propagation frequency, called RF, by a single tone generated by some local generator and is therefore commonly called the LO. The choice of IF, whether at DC or near to, is an architectural design choice between a homodyne (direct or DC conversion) or heterodyne transceiver, respectively.

Figures B.1 and B.2 show typical homodyne and heterodyne receiver architecture. The main difference is ω_{if} and the channel select filters. The additional filters are required due to non-ideal behavior of the components such as amplifier non-linearity caused by saturation. The saturation induces harmonic components to propagate through mixers generating *spurious* signals at unwanted frequencies. Sufficient care must be taken to eliminate unwanted spurious noise by strategic filtering. For SDRs the transceiver architecture is chosen to be flexible and UWB to allow for multiple applications to be implemented from the same system. Typically homodyne, fully coherent receivers and transmitters are used.

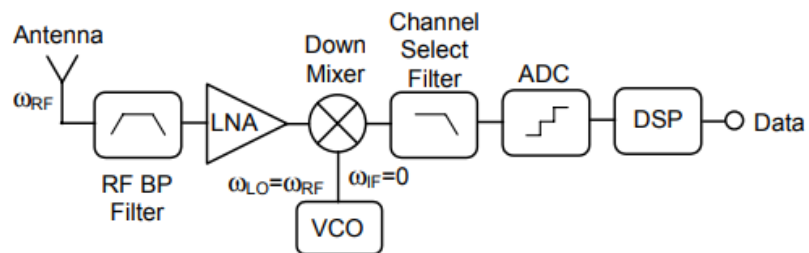


Figure B.1: Homodyne or Direct Down Conversion Receiver Architecture [153]

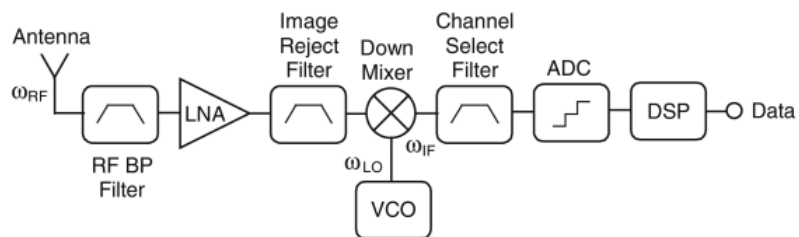


Figure B.2: Heterodyne Conversion Receiver Architecture [153]

Appendix C

Electromagnetic Theory

C.1 Electromagnetic Material Properties

The movement of electrons or any charge carrier in a conductor will, by Maxwell's equations, displace an electric field \vec{E} which induces a magnetic field \vec{H} which can, by Lorentz Forces, displace free electrons in another conductor. However, the fields cannot change instantaneously within a medium and thus changes must propagate at a finite speed. The velocity of propagation in a vacuum is the speed of light c^1 .

If the material has a large density of molecular electric dipoles, the applied field can create electric dipole moments and effect the total electric flux density or displacement field \vec{D} by inducing an electric polarization density \vec{P}_E . If \vec{P}_E is linearly related to \vec{E} by equation C.1, the relationship between the displacement field and the electric field can be written as the constitutive equation C.2. Where ϵ_0 is the permittivity of free space² and χ_E is the electric susceptibility.

$$\vec{P}_E = \epsilon_0 \chi_E \vec{E} \tag{C.1}$$

$$\vec{D} = \epsilon_0 \epsilon_r \vec{E} \tag{C.2}$$

¹ $c = 299,792,458$ meters per second

² $\epsilon_0 = 8.854187817 \times 10^{-12}$ Farads per meter

The relative permittivity ϵ_r is the free space normalized permittivity and is a complex frequency and position dependent number or tensor. In a non-dispersive, homogeneous and isotropic medium, the frequency dependence, position dependence and tensor matrix properties are dropped, respectively, and a single complex number is left as shown in equation C.3. The complex part represents the dielectric damping of the medium and the real part is called the *dielectric constant*; $D_k = \frac{\epsilon'}{\epsilon_0}$. From Maxwell's curl equation, the ratio between dielectric damping plus conductivity σ and dielectric constant determines if a material can propagate fields without loss based on the loss tangent as defined by equation C.4. In a conductor, the loss tangent is overwhelmed by conductivity and the material becomes an inefficient propagator of fields through displacement currents because currents are "shorted" through conductive currents. In a insulator or "dielectric", the propagation loss is dominated by dielectric damping.

$$\epsilon = \epsilon_0 \epsilon_r = \epsilon' - j\epsilon'' \quad (\text{C.3})$$

$$\tan \delta = \frac{\omega\epsilon'' + \sigma}{\omega\epsilon'} \quad (\text{C.4})$$

$$\tan \delta_{\text{conductor}} \cong \frac{\sigma}{\omega\epsilon'} \quad (\text{C.5})$$

$$\tan \delta_{\text{dielectric}} \cong \frac{\epsilon''}{\epsilon'} \quad (\text{C.6})$$

An analog of the medium's electrical properties are found in its magnetic properties. The magnetization density \vec{M} is the measure of magnetic moments caused by a magnetic field \vec{H} by a linear factor χ_M in equation C.7. The medium's combined magnetic effects can be written as a constitutive equation C.8, where μ_0 is the permeability of free space³ and μ_r is the relative permeability. For most

³ $\mu_0 = 4\pi \times 10^{-7}$ Henrys per meter

dielectrics and conductors used in microwave design, $\mu_r = 1$ and permeability is ignored by calculations.

$$\vec{M} = \mu_0 \chi_M \vec{H} \quad (\text{C.7})$$

$$\vec{B} = \mu_0 \mu_r \vec{H} \quad (\text{C.8})$$

The permittivity ϵ , permeability μ , and conductivity σ of a medium play a fundamental role in its scattering characteristics. For a given interface between two mediums with different electromagnetic characteristics, the reflection coefficient is defined as the complex ratio between the electric field of a reflected wave \vec{E}_r and the original incident wave \vec{E}_i and can be expressed in terms of intrinsic impedance of each medium as expressed in equation C.9.

$$\Gamma = \frac{\vec{E}_r}{\vec{E}_i} = \frac{\eta_2 - \eta_1}{\eta_2 + \eta_1} \quad (\text{C.9})$$

Impedance can be thought of as the intrinsic force needed per unit velocity. For electromagnetism in mediums, the force is provided by electric and magnetic fields, and the velocity is either the conductive or displacement currents. The impedance of medium can be defined from the electromagnetic characteristics in equation C.10 where γ is the propagation constant defined as equation C.11.

$$\eta = \sqrt{\frac{j\omega\mu}{\sigma + j\omega\epsilon}} = \frac{j\omega\mu}{\gamma} \quad (\text{C.10})$$

$$\gamma = \alpha + j\beta = j\omega\sqrt{\mu\epsilon}\sqrt{1 - j\sigma/\omega\epsilon} \quad (\text{C.11})$$

As the medium approaches a loss-less dielectric, $\sigma \rightarrow 0$ and ϵ and μ become strictly real quantities. The propagation constant can be written as equation C.12,

$$\gamma = j\beta = j\omega\sqrt{\mu\epsilon} \quad (\text{C.12})$$

and the intrinsic impedance can be written as equation C.13, where the intrinsic impedance of free space is defined as $\eta_0 = \sqrt{\mu_0/\epsilon_0} \cong 377\Omega$.

$$\eta = \frac{j\omega\mu}{j\omega\sqrt{\mu\epsilon}} = \sqrt{\frac{\mu}{\epsilon}} = \eta_0\sqrt{\frac{\mu_r}{\epsilon_r}} \quad (\text{C.13})$$

For most usable dielectrics found in nature, $\mu_r \cong 1$, resulting in the real part of the complex permittivity or the dielectric constant being responsible for an intrinsic impedance difference between two mediums. Intuitively, this can be thought of as reduction in the propagation velocity by a factor of $\frac{1}{\sqrt{\epsilon_r}}$, resulting in a reflection of a significant portion of the EM wave. A common analogy used to explain this phenomenon is the partial reflection in a window due to the impedance transition from air to glass. In another example, water can have a dielectric constant lower than 10 and is dependent on temperature, state, concentration and many other factors as seen in Figure C.1. By equations C.13 and C.9, $\Gamma \geq 0.52$. Thus, at least more than half the wave's energy is reflected.

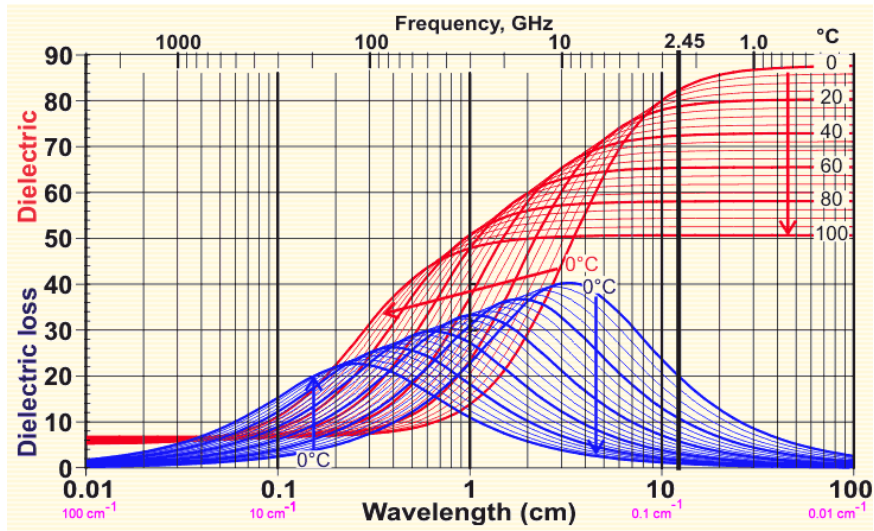


Figure C.1: Dielectric permittivity and dielectric loss of water between 0°C and 100°C [154]

For conductors, as $\sigma \rightarrow \infty$; $\alpha \rightarrow \infty$; $\eta \rightarrow 0$; $\Gamma \rightarrow -1$. Thus, the wave decays infinitely fast and then completely reflects similar to a shorted transmission line. Table C.1 shows rough estimates of conductivity, dielectric constant, and relative

permeability to give the reader an idea of electromagnetic and scattering behavior of common materials in the environment.

Medium	σ [S/m]	D_k	μ_r
Iron	1.00×10^7	-	5000
Copper	5.96×10^7	-	0.999994
Gold	4.10×10^7	-	0.999493
Silver	6.30×10^7	-	0.99998
Aluminium	3.77×10^7	-	1.000022
Sea Water	s4.80	75	0.999992
Drinking Water	$5 \times 10^{-4} \leftrightarrow 5 \times 10^{-2}$	80	0.999992
Silicon	1.56×10^{-3}	11.7	1
Wood	$10^{-4} \leftrightarrow 10^{-3}$	1.22	1.00000043
Glass	$10^{-15} \leftrightarrow 10^{-11}$	6.5	1
Air	$10^{-15} \leftrightarrow 10^{-9}$	1.00058986	1.00000037
Teflon	$10^{-25} \leftrightarrow 10^{-23}$	2.1	1.0000

Table C.1: Electric and Magnetic Characteristics of Common Materials

Appendix D

Bill of Materials

System	Function	Company	Part Number	Price	Spec
Both	SDR	Lime	LimeSDR	\$300	3.8 <i>GHz</i>
S-Band	PA	ADI	ADL5321	\$9	250 <i>mW</i>
Both	LPF	MC	VLP-54	\$25	4 <i>GHz</i>
Both	IF AMP	MC	ZX60-V62+	\$50	15 <i>dB</i>
Both	LNA	MC	ZX60-153LN-S+	\$200	3 <i>dB NF</i>
LO	VCO	MC	ZX95-2500A-S+	\$45	2 – 2.6 <i>GHz</i>
LO	LPF	MC	VLFX-2500+	\$40	2.5 <i>GHz</i>
LO	Tripler	MC	ZX90-3-812-S+	\$52	2 – 3 <i>GHz</i>
LO	LO AMP	MC	ZX60-183A-S+	\$170	30 <i>dB</i>
LO	HPF	MC	VHF-6010+	\$25	6.3 <i>GHz</i>
LO	LPF	MC	VLF-8400+	\$22	8.4 <i>GHz</i>
LO	Splitter	MC	ZX10-2-98-S+	\$40	3.5 <i>dB</i>
X-Band	PA	MC	ZX60-24-S+	\$290	18 <i>OP1dB</i>
X-Band	Mixer	MC	ZX05-153-S+	\$49	4 – 15 <i>GHz</i>
X-Band	Cavity Filter	MC	ZVBP-10R5G-S+	\$300	10 – 11 <i>GHz</i>
X-Band	HPF	MC	VHF-8400+	\$25	8.4 <i>GHz</i>
X-Band	Horn	Pasternack	PE9856/SF-15	\$1100	WR-90
X-Band	FuncGen	SciCore	AWG2300	\$600	50 <i>MHz</i>
X-Band	LDO	TI	TPS7A4701	\$20	1 <i>Amp</i>

Table D.1: Bill of Materials